UNIVERSITY OF CALIFORNIA

Santa Barbara

What do marine particle characteristics and dynamics tell us about the efficiency of the Biological Carbon Pump?

A dissertation submitted in partial satisfaction of the

requirements for the degree Doctor of Philosophy

in Marine Science

by

Elisa Romanelli

Committee in charge:

Professor David A. Siegel, Chair

Professor Uta Passow

Professor Craig Carlson

Professor Alyson Santoro

September 2023

The dissertation of Elisa Romanelli is approved.

Uta Passow

Alyson Santoro

Craig Carlson

David A. Siegel

September 2023

What do marine particle characteristics and dynamics tell us about the efficiency of the Biological Carbon Pump?

ACKNOWLEDGEMENTS

A big thank you goes to Uta, Dave, Alyson, and Craig and all the people that have supported me during these five years.

With much gratitude,

Elisa

VITA OF ELISA ROMANELLI
September 2023

EDUCATION

- Doctor of Philosophy in Marine Science, University of California, Santa Barbara, September 2023 (expected)
- Master of Science, University of Bologna, Ravenna, March 2018
- Bachelor of Science, University of Bologna, Ravenna, March 2015 (summa cum laude)

PUBLICATIONS

- **Romanelli E**, Giering SL, Estapa M, Siegel DA, Passow U. Storms affect sinking fluxes at the end of the North Atlantic spring bloom (In preparation)
- **Romanelli E**, Cisternas-Novoa, C., Stevens-Green, R., LaRoche, J., Siegel, D.A.,
- Carlson, C.A., Passow, U. Microbial activity on suspended and sinking particles during a Phaeocystis bloom in the Labrador Sea. (In preparation)
- Sweet J, **Romanelli E**, D'souza N, Passow U. Light determines cell size and carbon content of the marine diatom Thalassiosira pseudonana at supra-optimal temperatures (In preparation)
- **Romanelli E**, Giering SL, Sweet J, Siegel DA, Passow U. The presence of transparent exopolymer particles rather than ballast determines sinking of small particles in the Northeast Pacific Ocean (Accepted, Elementa: Science of the Anthropocene)
- Graff J, Nelson N, Roca-Martí M, **Romanelli E**, et al. Reconciliation of total particulate organic carbon and nitrogen measurements determined using contrasting methods in the North Pacific Ocean (In review, Elementa: Science of the Anthropocene)
- Ragazzola, F., Nannini, M., Raiteri, G., Peirano, A., Kolzenburg, R., **Romanelli E**., et al. Flexible artificial habitats: in early-stage ecological communities, buffer capability is more important than structural complexity (Submitted for review to Hydrobiologia)
- Ragazzola, F., Marchini, A., Adani, M., Bordone. A., Castelli, A., […], **Romanelli, E**., et al. 2021. An intertidal life: combined effects of acidification and winter heatwaves on a coralline alga (Ellisolandia elongata) and its associated invertebrate community.
- Mar. Environ. Res. 169:105342. doi: 10.1016/j.marenvres.2021.105342
- Wolf KKE, **Romanelli E**, Rost B, et al. Company matters: The presence of other genotypes alters traits and intraspecific selection in an Arctic diatom under climate change. Glob Change Biol. 2019;00:1–16. https ://doi. org/10.1111/gcb.14675

AWARDS

- 2023, Individualized Professional Skills Grant, (1,000$)
- 2023, UCSB Travel Grants, (4,000$)
- 2022, ARP Summer Grant, (7,000$)
- 2022, IGPMS Summer Grants, (5,100$)
- 2020, Nejat Ezal: Memorial Scholarship, (2,000$)

- 2020, ERI's Summer Fellowships, (10,669$)
- 2019, UCSB International Doctoral Recruitment Fellowship, (45,306$)
- 2018, Fulbright Graduate Study, Self-Placed Scholarship, (38,000$)
- 2018, Zegna Founder's Scholarship, (5,000$)
- 2017, Erasmus Placement Scholarship, (3,400$)
- 2015, University of Bologna's Overseas Scholarship, (4,000$)
- 2015, Erasmus Placement Scholarship, (2,500$)

FIELDWORK

- May 2022: RV Celtic Explorer, Cruise CE22009 (34 days)
- May 2021: RRS James Cook, Cruise JC214 (31 days)
- Dec 2019: RV Sally Ride, Cruise SR1919 (7 days)

CONFERENCES

- Romanelli E, Giering S, Estapa M, Siegel DA, and Passow U (2023), Temporal decoupling of two particle export mechanisms at the decline of the North Atlantic spring phytoplankton bloom, presented at ASLO Aquatic Sciences Meeting 2023, Palma de Mallorca, 4-9 June. Talk
- Romanelli E, Giering S, Estapa M, Siegel DA, and Passow U (2023), Marine particle characteristics and dynamics at the decline of the North Atlantic spring phytoplankton bloom, presented at SoCal BOOM meeting, UC Irvine, 29 April. Talk
- Romanelli E, Giering S, Estapa M, Siegel DA, and Passow U (2022), Characteristics and fluxes of sinking particles during the demise of the North Atlantic spring bloom, presented at OCB Summer Workshop 2022, Woods Hole, 20-23 June. Poster
- Romanelli E, Passow U, and Siegel DA (2020), Partitioning of biogeochemical properties between non-sinking and sinking particles collected during EXPORTS, presented at Ocean Sciences Meeting 2020, San Diego, CA, 16-21 December. Poster
- Romanelli E, Growth response of Thalassiosira pseudonana under combined light and temperature changes, S. Teresa Marine Environment Research Centre, Italy, November 2017. Invited talk

TEACHING EXPERIENCE

- Winter 2021, Climatic Change, and Its Consequences (GEOG119)
- Fall 2020, Oceans and Atmosphere (GEOG3)
- Fall 2019, Coastal pollution (GEOG132)

ABSTRACT

What do marine particle characteristics and dynamics tell us about the efficiency of the Biological Carbon Pump?

by

Elisa Romanelli

Gravitational sinking of particles is a key pathway for the transport of particulate organic carbon (POC) into the deep ocean. The sinking of POC and its remineralization directly impact ocean carbon storage on climatologically relevant timescales. Particle size, density and composition influence particle sinking velocity and the remineralization length scale i.e., the depth where POC is converted to suspended organic carbon or inorganic carbon. However, the factors affecting this relationship and their spatiotemporal variability are not well understood. Here, we use data collected from Marine Snow Catchers to characterize profiles of both suspended and sinking particles. Particle size, biogeochemical composition, and microbial activity are used to understand the controls and fate of suspended and sinking POC in the upper ocean. My first chapter shows that during the late summer in the subarctic Pacific POC fluxes were low, marine snow-sized aggregates ($d > 0.5$ mm) were rare and small, suspended particles differed from small sinking particles by their higher TEP (transparent exopolymer particles) content. This work provides the first in situ data to support the hypothesis by Xavier et al. (2017) that the ratio between TEP-C and POC

determines, at least partially, the efficiency of the biological carbon pump (i.e., POC flux 100 m below reference depth/flux at reference depth).

My second chapter focuses on the decline of the spring diatom bloom in the NE Atlantic and shows that turbulent disaggregation and changes in the mixed layer depth due to four strong storms delayed the formation and sinking of POC-rich marine snow-sized aggregates ($d > 0.1$ mm) while small, slow-sinking silica-rich particles sank from the mixed layer, creating an inefficient POC export event. After the last storm passed, we observed the sinking of marine snow aggregates, which resulted in vertical flux of a mixed post-bloom plankton community out of the euphotic zone.

My third chapter focuses on a study conducted in the Labrador Sea, where microbial degradation of total organic carbon (TOC) differed between suspended and sinking particles and across different stages of a spring *Phaeocystis* bloom. Carbon removal rates for fast-sinking and slow-sinking particles were similar but were on average one order of magnitude larger than those found for the suspended fraction. However, at the station characterized by abundant free-floating *Phaeocystis* colonies, the suspended fraction sustained a TOC removal rate similar to the ones for sinking particles. This observation suggests that the presence of *Phaeocystis* colonies may have enhanced the rate of microbial degradation of TOC.

Overall, this work highlights the importance of investigating characteristics and dynamics of suspended and sinking particles to understand which factors affect the efficiency of the biological carbon pump in different open ocean systems.

TABLE OF CONTENTS

Motivation

The ocean plays a pivotal role in controlling the earth's climate by storing a large amount of carbon dioxide (CO_2) at depth and thus acting as a carbon sink. The biological carbon pump (BCP), which includes the processes associated with production, sinking and remineralization of particulate organic carbon (POC), regulates the interaction between the atmosphere and the deep ocean to the extent that without the BCP the concentrations of atmospheric CO_2 would be ~ 200 ppm higher than present (Volk and Hoffert, 1985; Parekh et al. 2006). The strength (magnitude of POC flux out of the euphotic zone, i.e., carbon export flux) and transfer efficiency (fraction of POC flux transported to a target depth) of the BCP (Buesseler et al., 2020) mainly depends on the gravitational settling of particles, physical advection and mixing of particles, and the active vertical transport of particles due to migrating zooplankton and fishes (Boyd et al., 2019). By shaping the carbon export flux and other elements to the mesopelagic these processes influence the delivery of biochemical elements and nutrients to the local food-web (McKinley et al., 2017) and have the potential to impact atmospheric carbon dioxide concentrations over climatologically relevant timescales (Kwon et al., 2009). Current estimates of the carbon export flux obtained from global ocean models are not well constrained and show an elevated uncertainty (5–12 Pg C yr^{-1}) (e.g., Boyd and Trull, 2007; Henson et al., 2011; Siegel et al., 2014; Nowicki et al., 2021) that is comparable to the yearly global fossil fuel emission rate of the last decade (2010–2019) (Friedlingstein et al., 2020). This comparison highlighting the pressing need to elucidate the mechanisms driving the BCP to be able to better estimate the ocean carbon storage and predict the response of the ocean and of its carbon sequestration potential under current and future climate. Gravitational settling particles are the major carbon export flux

pathway of the BCP (Boyd et al, 2019; Nowicki et al., 2022). Marine particles mainly sink as single phytoplankton cells, aggregates, and fecal pellets. During their descent, particles can disaggregate, be consumed, repackaged and remineralized. The depth to which a particle sinks is controlled by its sinking velocity and the rate at which the particle is remineralized by bacteria (Omand et al., 2020; Alcolombri., 2021). The sinking velocity of particles plays a key role in controlling the distribution of particulate carbon within the water column (Khatiwala et al., 2013; Marsay et al., 2015; McDonnell et al., 2015). It is often assumed that particle sinking velocities increase mainly as a function of size following Stokes' law and that small sinking particles either do not sink or sink so slowly that they are remineralized within the upper mesopelagic (Riley et al., 2012). However, recent work has shown that small sinking particles can be an important contributor of POC to the mesopelagic environment in different open ocean ecosystems, hence they require careful consideration (e.g., Riley et al., 2012; Giering et al., 2016). Size classification must be considered in relation with particle composition (e.g., presence of dense mineral and buoyant gel-like particles), which influences particle density thus regulating their sinking velocity (Passow and De La Rocha, 2006; Iversen and Lampitt, 2020). The relationship between particle sinking velocity, particle composition and microbial degradation is complex and changes across different ecosystem types.

In the present thesis, we studied this relationship on suspended, slow- and fast-sinking particles collected using Marine Snow Catchers and we investigated how particles characteristics and dynamics contributed to the biological carbon pump of contrasting ecosystems.

Introduction

Gravitational settling particles

Gravitational settling particles are the largest component of the BCP (Boyd et al. 2019; Nowicki et al. 2022). Marine particles are mainly produced in the surface ocean as living phytoplankton cells (primary production) and they passively sink as single phytoplankton cells, aggregates, fecal material, detritus, carcasses, and minerals. Their fate and distribution within the water column is influenced by biological, physical, and chemical processes that change their size, density, and consequently sinking velocity.

The size range of marine particles spans from being colloidal (submicron diameter) to being marine snow (equivalent spherical diameter, ESD > 0.5 mm). Aggregation and disaggregation processes move particles up and down the size range affecting the transfer of POC into the deep ocean. Aggregation can increase the removal rate of material in the form of small, suspended particles by transforming them into large and possibly rapidly sinking particles (Burd and Jackson, 2008). When particles aggregate, their size increases forming marine snow-sized particles, which have the potential to sink more rapidly and more easily escape consumption, bringing organic matter to the deep ocean (Alldredge and Silver, 1988). During their descent, particles can disaggregate or be removed via the activity of heterotrophic prokaryotic bacteria, and interaction with zooplankton. In addition, zooplankton may inject new particles throughout the water column as byproducts of their feeding on organic matter in the form of fecal pellets, carcasses, or release via sloppy feeding. Zooplankton fecal material has been found to dominate the carbon export flux to the mesopelagic in different marine ecosystems (e.g., Ebersbach and Trull, 2008; Steinberg

et al., 2021). Due to their size, marine snow aggregates and large fecal pellets are considered the main vector of carbon exports to the deep ocean (Turner et al., 2015).

Stokes' Law, which describes the sinking of spherical solid particles in a laminar flow, assumes that particle sinking velocities increase mainly as a function of particle size and to a lesser extent by particle excess density over seawater. The implication is that large particles sink fast (50 – over 2000 m d^{-1}, range for marine snow and fecal pellets) and therefore can escape consumption and reach great depths. Smaller particles either remain suspended or sink so slowly that they are remineralized within the upper mesopelagic (Riley et al., 2012). However, the presence of small particles (0.2 – 20 μm) has been observed at great depths (> 1000 m) (e.g., dall'Olmo and Mork, 2014) challenging this view. Furthermore, recent studies have shown that the downward flux of POC via small particles (< 100 μm) can be significant in specific ecosystems and seasons often constituting the bulk of the total POC flux to the mesopelagic (e.g., Alonso-González et al., 2010; Durkin et al., 2015; Giering et al., 2016). Recently, it has been shown that the sinking velocity of marine particles is controlled by particle size but to a lesser extent than suggested by Stokes' Law (Cael et al., 2021). Therefore, particle size must be considered in relation with particle composition (presence of ballast minerals and gel-like particles) which influence particle density and thus helps regulate particle's sinking velocity (Passow and De La Rocha, 2006; Iversen and Lampitt, 2020; Cael et al., 2021). Ballast minerals such as biogenic silica from silicifying microorganisms, calcium carbonate from calcifying microorganisms and lithogenic silica from terrestrial sources (i.e., dust) may increase particle excess density over seawater and therefore particle sinking velocity (Klaas and Archer, 2002; Armstrong et al., 2009; McDonnell and Buesseler, 2010). The presence of transparent exopolymer particles (TEP)

has also the potential to influence the passive sinking of particles. Transparent Exopolymer Particles are gel-like particles mainly composed by acidic polysaccharides stainable using the cationic dye Alcian blue (Passow and Alldredge, 1995b). They form from extracellular surface-active exopolymers mostly released by phytoplankton and bacteria (Passow, 2002). An important characteristic of TEP is that these particles are very sticky. Stickiness increases the probability of successful attachment of colliding particles (Passow et al., 1994; Jackson, 1995, Engel et al., 2004), and thus enhance the formation of marine snow-sized aggregates. It has been suggested that the ratio between TEP and "solid" particles in an aggregate, may control the aggregate sinking velocity and therefore the export of POC (Mari et al., 2017). In fact, TEP are positively buoyant, and therefore their presence may reduce aggregate sinking velocity when the contribution of TEP in respect to "solid" particles is high (Engel and Schartau, 1999; Azetsu-Scott and Passow 2004) (Figure 1).

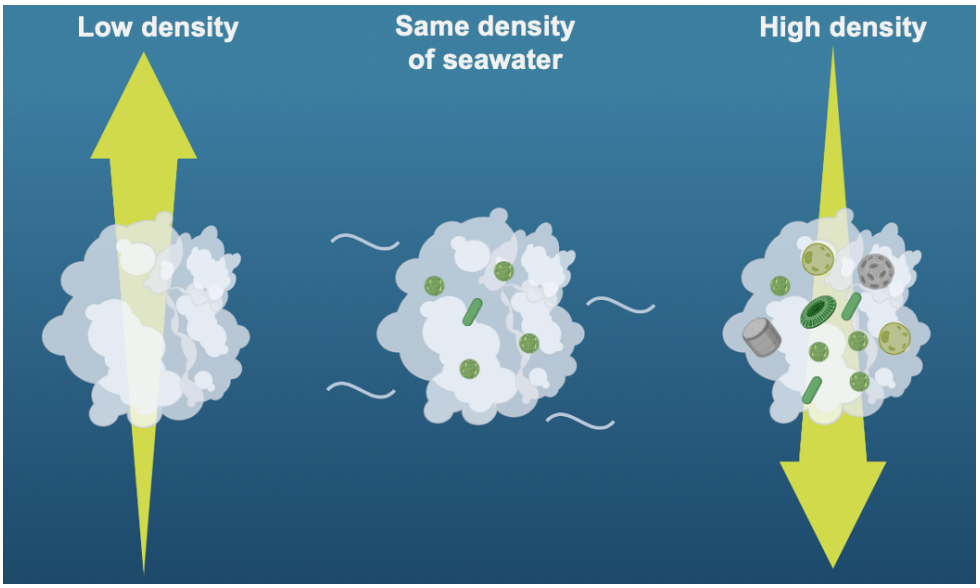

Figure 1. Conceptual schematic summarizing how transparent exopolymer particles (TEP) may affect the density of aggregates and therefore the sinking of POC in the water column. Aggregates rich in TEP may move upward (TEP have a density much lower than seawater,

Azetsu-Scott and Passow, 2004), may remain suspended or sink depending on the contribution of particles with high density to the aggregate.

We currently have a relatively limited mechanistic understanding of all the processes and factors that affect the sinking of particles in the water column. Hence, we lack accurate and universal predictions of particle sinking velocity and how particle sinking velocity changes across different oceanic ecosystem. This knowledge gap limits our understanding of the efficiency of the BCP and our ability to precisely estimate POC flux in the mesopelagic.

Particle flux attenuation and the ocean carbon storage

Depending on the oceanic ecosystem, only about 5 to 25 % of the ocean primary production is exported out of the euphotic zone (EZ) and into the upper mesopelagic (Buesseler et al., 2007b; Henson et al., 2012), and even less reaches the deep ocean. Below the EZ, zooplankton and heterotrophic prokaryotic bacteria rely on sinking POC as their main food source (Buesseler et al., 2007b; Steinberg et al., 2008), with heterotrophic bacteria being largely responsible for POC remineralisation into dissolved inorganic carbon (DIC) (e.g., Ploug et al., 1999; Giering et al., 2014; McDonnell et al., 2015). The depth at which the carbon export flux is attenuated, and organic carbon is converted back to CO_2 (remineralization depth) substantially impact atmospheric CO_2 concentrations on relevant timescales (Kwon et al., 2009; DeVries et al., 2012). This depth is the result of two opposing processes: particle sinking velocity, and the rate at which this particle is remineralized. The remineralization of POC is dominated by diverse interacting pathways (Collins et al., 2015). Particle-attached heterotrophic bacteria can direct respire POC or perform enzymatic solubilization or mechanical disaggregation of POC. Both solubilization and disaggregation transform POC into a dissolved or suspended organic carbon, which is

then accessible to the free-living bacterial communities. Zooplankton may also directly respire POC into CO_2. In addition, zooplankton may mechanical disaggregate POC via sloppy feeding and egest and excrete POC and DOC (Collins et al., 2015). With the exception for direct respiration, all the other processes change the size of POC, impacting its sinking velocity.

If we assume a steady state ocean, the attenuation of POC flux in the mesopelagic (carbon supply) should balance the present community respiration (carbon demand). However, with few exceptions (e.g., Giering et al., 2014), published estimates of POC flux attenuation are lower than corresponding estimates of heterotrophic metabolic rates (Steinberg et al., 2008). This discrepancy means that either organic carbon supply or its demand is not correctly constrained. One hypothesis is that there could be unaccounted sources of organic carbon to the mesopelagic (Burd et al., 2010). As aforementioned the traditional view suggests that carbon supply to the mesopelagic is dominated by large, fast-sinking particles. However, recent technological developments have allowed to document the presence of small particles in the deep ocean (Dall'Olmo and Mork, 2014). These particles are usually under-sampled by the canonical approaches used to measure POC export fluxes (sediment traps, Buesseler et al., 2007), and for this reason their importance has been long ignored and their source is still under debate. In certain ecosystems, zooplankton may mechanically degrade large, fast-sinking particles into small, suspended, and slow-sinking particles. The latter are subsequently consumed by heterotrophic bacteria supporting to some extent remineralization in the mesopelagic and thus helping to close the ocean carbon budget (Giering et al., 2014). Recently, particles fragmentation from large to

small was quantified for the first time and found to account for roughly half of the observed particle flux loss at high latitudes (Briggs et al., 2020) supporting this hypothesis.

Additionally, the contribution of particle degradation processes to the observed particle flux attenuation remains uncertain and challenging to measure. Current methods may potentially lead to an overestimation of the bacterial carbon demand (BCD) (Burd et al., 2010). Bacterial carbon demand includes all the organic carbon assimilated by heterotrophic bacteria, which can be divided into anabolic (bacterial production, BP) and catabolic (bacterial respiration, BR) processes. Heterotrophic bacteria do not perform anabolic and catabolic processes at the same rates making methods and measurements hard to reconciliate. Bacterial carbon demand is calculated based on estimates of bacterial growth efficiency (BGE) (BGE = bacterial production/bacterial carbon demand) (Carlson and Hansell, 2015), which is generally low and show large variability caused, among others, by the quantity and quality of organic matter, heterotrophic community composition, and environmental conditions (e.g., del Giorgio and Cole, 1998; González-Benítez et al., 2019). Bacterial production and respiration are assessed with diverse approaches that integrate over different time scales and show specific caveats. For examples, BP is commonly measured from the uptake rates of amino acid leucine over a few hours and serves as a proxy of labile carbon uptake by bacteria (Simon and Azam 1989). However, amino acids are only one component of the DOC pool; in addition, recent work has shown that the standard conversion factor (Simon and Azam 1989) used to convert leucine incorporation rates into carbon units may overestimate BP depending on the oceanic ecosystem under study (Giering and Evans, 2022).

Respiration is one of the least constrained metabolic processes of the ocean. Rates of microbial respiration in the mesopelagic zone are slow and many direct methods cannot make reliable measurements leaving the scientific community with large mismatches between predictions and observations (Robinson et al., 2020, SCOR-WG). Respiration rates can be estimated from the consumption of oxygen or production of carbon dioxide in incubated water samples. Some of the methods include the Winkler oxygen titration method (Winkler 1888) and the use of oxygen sensors based on electrochemical or optical signaling (e.g., Wikner et al., 2013; Lehner et al., 2015). Microbial respiration can also be estimated from BP, which however requires assuming a BGE. Carbon uptake and remineralization can be estimated by measuring TOC and DOC drawdown in incubation experiments (Baetge et al., 2021). However, this method has not been applied to sinking particles yet. Finally, RESPIRE particle interceptor have been successfully used to measure the respiration of sinking POC by particle-attached bacteria in situ (Boyd et al., 2015).

Ultimately, it is fundamental to constrain estimates of mesopelagic microbial respiration to be able to estimate the how much of the POC flux attenuation is mediated by bacteria. For this reason, there is a clear need to develop new techniques and reconcile current methodologies.

I. The importance of transparent exopolymer particles over ballast in determining both sinking and suspension of small particles during late summer in the Northeast Pacific Ocean

Elisa Romanelli, Julia Sweet, Sarah Lou Carolin Giering, David A. Siegel, Uta Passow

Accepted by Elementa: Science of the Anthropocene

Abstract

Gravitational sinking of particles is a key pathway for the transport of particulate organic carbon (POC) to the deep ocean. Particle size and composition influence particle sinking velocity and thus play a critical role in controlling particle flux. Canonically, sinking particles that reach the mesopelagic are expected to be either large or ballasted by minerals. However, the presence of transparent exopolymer particles (TEP), which are positively buoyant, may also influence particle sinking velocity. We investigated the relationship between particle composition and sinking velocity during the Export Processes in the Ocean from RemoTe Sensing (EXPORTS) campaign in the Northeast Pacific Ocean using Marine Snow Catchers. Suspended and sinking particles were sized using FlowCam for particle imaging, and their biogeochemical composition was assessed by measuring the concentration of particulate organic carbon (POC) and nitrogen, particulate inorganic carbon, biogenic and lithogenic silica, and TEP. Sinking fluxes were also calculated. Overall, both suspended and sinking particles were small (<51 μm, diameter) in this late summer, oligotrophic system. Contrary to expectation, the ratio of ballast minerals to POC was higher for suspended particles than sinking particles. Further, suspended particles showed TEP-to-POC ratios three times higher than sinking particles. These ratios suggest

that TEP content and not ballast dictated whether particles in this system would sink (low TEP) or remain suspended (high TEP). Fluxes of POC averaged 4.3 ± 2.5 mmol C m^{-2} d^{-1} at 50 m (n = 9) and decreased to 3.1 ± 1.1 mmol C m^{-2} d^{-1} at 300–500 m (n = 6). These flux estimates were slightly higher than fluxes measured during EXPORTS with drifting sediment traps and Thorium-234. A comparison between these approaches illustrates that small sinking particles were an important component of the POC flux in the mesopelagic of this late summer oligotrophic system.

Introduction

The biological carbon pump (BCP) comprises the processes that mediate the transfer of organic carbon from the euphotic zone, where it is produced, to the deep ocean (Volk and Hoffert, 1985). Without the BCP the concentrations of atmospheric CO_2 would be approximately 200 ppm higher than present (Parekh et al., 2006). The efficiency of the BCP depends primarily on the gravitational settling of particles, the physical advection and mixing of particles, and the active vertical transport of particles due to migrating zooplankton and fish (Boyd et al., 2019). These processes shape the flux of carbon and other elements through the mesopelagic and abyssopelagic zones, where carbon can be locked away from the atmosphere, impacting atmospheric CO_2 concentrations over climatologically relevant timescales (Kwon et al., 2009; DeVries et al., 2012). Accurately predicting the response of the ocean carbon storage to already underway and future climate changes requires a mechanistic knowledge of the processes making up the BCP (e.g., Siegel et al., 2023).

The largest component of the BCP is settling particles (Boyd et al., 2019; Nowicki et al., 2022). Particles in the open ocean are mainly produced in the surface layer and consist of

living and dead phytoplankton cells, detritus, carcasses, fecal material, and minerals. Their size range spans between less than a micrometer (typical threshold defined as 0.7 μm in diameter) to many millimeters, with those of a diameter >0.5 mm being referred to as "marine snow" (Alldredge and Silver, 1988). The fate and distribution of particles are influenced by the transformation processes that change particle size, composition and, consequently, sinking velocity. Particles can aggregate, disaggregate, solubilize or be remineralized back to inorganic forms via mechanical forcing, bacterioplankton activity, and interaction with zooplankton (Stemmann et al., 2004; Burd et al., 2010; Giering et al., 2014; Collins et al., 2015). When particles aggregate or are repackaged into fecal matter, they have the potential to sink rapidly (approximately 50 to ≥2,000 m d^{-1}) and hence more easily escape consumption, fragmentation, and dissolution at shallow depths, thus bringing organic matter to the deep ocean more efficiently than smaller particles (Alldredge and Silver, 1988; Ebersbach and Trull, 2008).

Particle sinking velocities are typically thought to be determined largely by size. Stokes' Law, which quantifies the sinking velocity of spherical solid particles under laminar flow conditions, assumes that particle sinking velocity increases as the product of the spherical particle diameter squared and the excess density with respect to seawater. The implication for sinking particles in the ocean is that large particles should sink rapidly and are hence effective vectors for carbon transport to depth, whereas small particles should sink slowly and be remineralized within the upper mesopelagic, contributing little to BCP-mediated ocean carbon storage (Kriest, 2002; Marsay et al., 2015; Cavan et al., 2017). Nevertheless, the presence of small particles (0.2–20 μm) has been observed at great depths (>1000 m; e.g., Dall'Olmo and Mork, 2014; Briggs et al., 2020). Furthermore, recent studies have

shown that the downward flux of particulate organic carbon (POC) via small particles (<100 μm) can be significant in specific ecosystems and seasons, at times constituting the bulk of the total POC flux through the mesopelagic (e.g., Durkin et al., 2015; Giering et al., 2016; Bisson et al., 2020; Dever et al., 2021).

The presence of ballast minerals (biogenic silica from diatoms, particulate inorganic carbon from coccolithophores and foraminifera, and lithogenic material from aeolian and riverine inputs) is also thought to increase particle sinking velocity by increasing particle excess density in respect to seawater (Armstrong et al., 2002; Passow and De La Rocha, 2006; Laurenceau-Cornec et al., 2019; Iversen and Lampitt, 2020; Iversen, 2023). However, cause and effect in the relationship between organic matter and minerals is not clear, and sinking aggregates originating from biological activity in the mixed layer could scavenge and subsequently transport small, suspended mineral particles to depth (Passow, 2004).

The presence of transparent exopolymer particles (TEP; Alldredge et al.,1993) also has the potential to influence the sinking of particles. TEP are composed largely of polysaccharides released by phytoplankton and bacteria as extracellular surface-active exopolymers (Passow, 2002), especially under nutrient-limited conditions (Obernosterer and Herndl, 1995). TEP may act as biological glue and thus enhance particle coagulation rate by increasing particle "stickiness" (Passow et al., 1994; Jackson, 1995). However, by being positively buoyant, TEP may also reduce aggregate sinking velocities, especially when aggregates are characterized by a high ratio of TEP to solid particles (Engel and Schartau, 1999; Azetsu-Scott and Passow, 2004). Although TEP has the potential to play an important role in controlling the downward transport of particles, we lack a robust mechanistic understanding of this process (e.g., Mari et al., 2017; Nagata et al., 2021).

Our hypothesis is that TEP play a critical role in determining the sinking velocity of particles, potentially outcompeting the role of ballast minerals. We assessed how particle size and composition regulate the partitioning between sinking and suspended particles within the upper mesopelagic in an iron-limited region of the Northeast Pacific Ocean. Particles were collected using Marine Snow Catchers (MSC) during the Export Processes in the Ocean from RemoTe Sensing field (EXPORTS) campaign. In addition, we considered the possible mechanisms driving the formation of small sinking particles in the mesopelagic and highlighted the importance of studying small particle characteristics and particle patchiness to enhance our understanding of the functioning of the biological carbon pump.

Materials and methods

Ocean Station Papa

This study is part of the first EXPORTS field campaign, which took place in late summer 2018 (August 14 to September 9) at Ocean Station Papa ('Station P'). Station P is a time-series site located in the Northeast Pacific Ocean (nominally 50°N 145°W) that has been monitored regularly since 1949 (e.g., Tabata 1965). It is a high-nutrient low-chlorophyll system with a 'muted' spring bloom owing to persistently low concentrations of iron (Martin and Fitzwater, 1988; Boyd et al., 1996). During our study, Station P was characterized by a shallow mixed layer (average: 29 ± 4 m, n = 226) and strong vertical and weak horizontal gradients in hydrographic properties (Siegel et al., 2021). Mixed layer macronutrient concentrations were elevated and chlorophyll *a* concentrations were low (0.10–0.35 μg L^{-1}) and lower than typical August values (2000–2017) for Station P (Siegel et al., 2021). This condition resulted in an isolume depth of the 1% photosynthetically available radiation (PAR) between 70 m and 90 m (Siegel et al., 2021), which was slightly

deeper than climatological conditions (Siegel et al., 2021). The site was characterized by a highly recycled food web in the mixed layer (Meyer et al., 2020; McNair et al., 2023), with low POC fluxes (Buesseler et al., 2020; Estapa et al., 2021), which were in line with previous observations performed at Station P (Charette et al., 1999; Wong et al., 2002; Kawakami et al., 2010; Timothy et al., 2013; Mackinson et al., 2015). An in-depth discussion of how POC fluxes measured during EXPORTS compare to previous POC flux measurements is provided by Buesseler et al. (2020).

The observations presented here were conducted from the R/V *Roger Revelle*, which sampled ecological and biogeochemical properties following an instrumented Lagrangian float at a depth of approximately 100 m. Detailed operations of the EXPORTS North Pacific field campaign have been described by Siegel et al. (2021).

Sample collection with the Marine Snow Catchers

Profiles of suspended and sinking particles were collected using three Marine Snow Catchers (MSC, OSIL, UK; Lampitt et al., 1993). The MSC is a large volume (volume: $V_{MSC} = 89.8$ L, height: $h_{MSC} = 1.5$ m) water sampler with a removable base section (approximately 8 L) that enables the partitioning of particles according to a predefined settling time (Riley et al., 2012; Giering et al., 2016). The MSCs were deployed at two to three depths ranging between 20 m and 500 m at 13 stations (Table S1). Deployment depths were chosen to include 1) just below the mixed layer depth (20–65 m), 2) at approximately 100 m (Lagrangian float depth), and 3) between 100 m and 500 m. Depths were adjusted to match where particle maxima were detected immediately before the MSC deployments, either via chlorophyll fluorescence profile, or particle counts from the Underwater Vision Profiler-5 (UVP, Hydroptic, France; Picheral et al., 2010). MSC casts were conducted in the

afternoons on days 1, 3, and 6 of each of the three 8-day sampling epochs, with additional two-depth casts on day 5 of epochs 2 and 3 (Table S1).

A full description of the MSC and its sampling methodology has been published by Riley at al. (2012) and Giering et al. (2016). We modified the protocol slightly as follows. During deployment, the terminal apertures of the top and base sections of the MSC were kept open and then were closed at the target depth through a wire-guided messenger trigger mechanism. A tray (height: $h_{tray} = 4.4$ cm, area: $A_{tray} = 0.028$ m^2, approximate volume: 1 L) was placed at the bottom of the MSC base section prior to each deployment. Immediately following deployment and retrieval, the MSC was secured in an upright position, the initial bulk population of particles was sampled from the MSC central tap (time zero, T_0), and particles were allowed to settle for 2 hours. We operationally defined three particle fractions, *top*, *base* and *tray*, according to their sampling locations within the MSC after the 2-hour settling period. The *top* fraction was collected from the central tap in the top section of the MSC and represents the suspended particle pool, i.e., particles that did not sink during the 2-hour settling period. Subsequently, the water contained in the upper part of the MSC was gently drained, and the upper part of the MSC removed. The water in the base section overlying the tray was siphoned off, constituting the *base* fraction (volume: $V_{base;}$ 4.5–5.5 L). Water in the tray was considered as the *tray* fraction (volume: V_{tray} 0.33–0.98 L). The *base*- and *tray*-sampled volumes varied across deployments depending on sampling efficiency (i.e., how much volume was lost during sampling). In the laboratory, the tray was visually investigated for the presence of marine-snow-sized particles. In two instances (settling time experiments; Section 2.6) the *tray* and *base* fractions were combined before sampling (referred to as *bottom* fraction).

All three fractions (*top*, *base*, *tray*) were subsampled for various parameters (Table S1). Subsamples for POC and particulate organic nitrogen (PON) analysis and for counts and identification (particle imaging via the FlowCam) were collected at all stations, except on August 17 when no samples were fixed for particle imaging. Subsamples for the analysis of total particulate carbon (TC), from which we obtained particulate inorganic carbon estimates (PIC) by difference (PIC = TC – POC), biogenic and lithogenic silica (bSi and lSi, respectively), were taken on days 3 and 5 of each epoch. Subsamples for the determination of TEP were collected on days 1 and 5 of each epoch, and the abiotic aggregation potential was determined on seawater collected on day 1 of each epoch.

Particle imaging and sizing with the FlowCam

Particle size distribution of suspended and sinking particles was assessed using particle imaging. Subsamples (50 mL) were fixed with 37% formalin (hexamethylenetetramine buffered) to a final concentration of 1–2% and stored in dark at 4°C until analysis. Subsamples were analyzed using a FlowCam 8000 Series (Yokogawa Fluid Imaging Technologies, US; Sieracki et al., 1998) in auto-image mode (particles imaged at a pre-defined flow rate; Table S2). To assess relevant particle sizes, we first analyzed subsamples using a 40x objective combined to a 300- x 1500-µm flow cell and then a 200x objective with a 50- x 300-µm flow cell. Of 30 suspended particle samples, 13 were not analyzed with the 40x objective due to time constraints. The minimum sizes reliably resolved by the objectives were 30 µm (40x) and 3 µm (200x). The maximum size, dictated by the flow cell size, was 300 µm for the 40x objective and 50 µm for the 200x objective. *Base* and *tray* fractions were pre-filtered using a 44-µm mesh filter to avoid clogging the 50- x 300-µm flow cell when using the 200x objective.

Based on the size of the particles and the FlowCam resolution, we chose to restrict our analysis to particles with an equivalent spherical diameter (ESD) between 4 μm and 128 μm. We calculated the minimum number of particles required to estimate a robust particle size spectrum using the empirical relationship given by Blanco et al. (1994) and assuming that a size bin is well represented if there are at least 10 particles in it (Álvarez et al., 2011). Thus, we imaged around 1,300 particles (i.e., minimum desired count and lowest number of counted particles) to cover a size range of 4 μm to <32 μm at 200x and a size range of ≥32 μm to 128 μm at 40x.

Imaged particles were sized using FlowCam VisualSpreadsheet© software version 4.15.1. and grouped in the 5 size bins based on their ESD. The complete method settings and example images are presented in Table S2. Particle concentrations of *top*, *base* and *tray* were calculated by dividing the counted number of particles in each size bin by the sample volume imaged. Suspended and sinking particle abundances were calculated as explained in Section 2.7. Particle size distributions (PSDs) were estimated as differential number size distributions N(D) (# particle mL^{-1} μm^{-1}) for *top* and *tray* fractions. The slope of the PSDs was calculated as the slope of a one-degree polynomial fit to the $\log_{10}$-transformed PSD and $\log_{10}$-transformed arithmetic mean of each size bin (μm) over the entire measured size range (polyfit function, Matlab R2021b).

Biogeochemical analyses

Typically, 1 L of each of the T_0, *top* and *base* fractions and approximately 0.1 L of the *tray* fraction were filtered for analysis of POC and PON, TC, bSi and lSi, and TEP. For the occasions when we carried out the settling time methodological test, 0.5–1.5 L of the *top* and *bottom* subsamples were filtered instead.

Concentrations of POC and PON were determined by filtering subsamples onto two replicate pre-combusted (450 °C, 30 minutes) GF/F filters (25 mm, Whatmann, UK). The filters were dried at 60°C and stored at room temperature until analysis. Filters were analyzed using a CEC 44OHA elemental analyzer (Control Equipment, US) after treatment with 10% HCl. Replicates were averaged (see average of the relative standard deviations of the filter replicates in Table S3). The range for the detection limit of POC and PON was 0.8–16 μg and 0.2–3.9 μg, respectively. All POC values were above the detection limit of the instrument. However, for PON, 24 of 237 values were below detection, seven of which were negative and therefore substituted with zero (μg L^{-1}). Values were corrected to account for non-target carbon on the filter using the average POC and PON mass (12.6 μg for POC; 2.1 μg for PON) of 28 blanks obtained using a multiple volume (0.5 L, 1 L and approximately 2 L) regression approach (Moran et al., 1999) for water collected with Niskin Bottles from the CTD-rosette system within the mixed layer (campaign-wide correction). A detailed explanation of the blank correction method and a reconciliation of all the POC and PON measurements obtained using different methodologies during the EXPORTS field campaign is presented by Graff et al. (n.d.).

TC was measured following procedures similar to POC but without prior acidification. Only one filter per fraction was generated due to volume constraints. No measured values fell below the instrument detection limit (1.2–4.5 μg). PIC was calculated by subtracting the uncorrected POC from TC.

Biogenic and lithogenic silica concentrations were determined by filtering samples onto 0.6 μm pore size polycarbonate membrane filters (47 mm diameter, Isopore, Millipore), which were dried at 60°C and stored at room temperature until analysis. Filters were

digested in Teflon tubes by adding 4 mL of 0.2 N NaOH (95°C, 40 minutes) and cooled immediately afterwards. The resulting solutions were neutralized by adding 1 mL of 1 M HCl and centrifuged (10 minutes, 2500 rpm) to separate lSi from bSi. Four mL of the solution was diluted with 6 mL of Milli-Q water and assessed via the molybdosilicic acid spectrophotographic method to measure bSi (Strickland and Parsons, 1968). The remaining 1 mL of solution, which was left at the bottom of the Teflon tube together with the filter, was rinsed using Milli-Q water, left to dry, and cooled. To extract lSi, 0.25 mL of 2.5 M hydrofluoric acid was added. After 48 hours 9.75 mL of 1 M saturated boric acid solution were added, and filters were centrifuged. Eight mL of the resulting solution was added to 2 mL of 1 M saturated boric acid solution and assessed spectrophotometrically as aforementioned.

Concentrations of TEP were determined colorimetrically on triplicate samples. Subsamples were filtered onto 0.4 μm pore size polycarbonate filters (25 mm, Whatmann, UK), stained with Alcian blue, and stored frozen until analysis. Filter blanks, prepared by staining and rinsing wet filters, were processed like the samples. Stained filters were soaked for at least 2 hours in 80% sulfuric acid (95% w/w; Fisher Scientific), and the absorption at 787 nm was measured spectrophotometrically (Thermo Scientific GENESYS 10S UV- VIS; Passow and Alldredge, 1995). The stained filters were compared to a standard curve developed using xanthan gum (Sigma-Aldrich), and hence TEP determinations were expressed as standardized xanthan gum equivalents (XGeq; Bittar et al., 2018). TEP determinations were considered above detection if the absorbance value of a sample at 787 nm was at least twice the absorbance value of the blank at 787 nm (Passow and Alldredge, 1995). A total of 28 of 112 TEP determinations measured from the MSC were below this

detection limit. TEP values associated with sinking particles between 300 m and 500 m were always at or below detection limit. In addition to the MSC samples, we also determined water column TEP on water collected using Niskin bottles fitted to a CTD rosette (depth range: 5–500 m; n = 153). A total of 22 of 153 TEP measurements on the water column sampled with the Niskin bottles were at or below the detection limit. We did not remove TEP values at or below the limit of detection but instead considered these observations an upper bound estimate of the true in situ concentrations. We expressed TEP in carbon units (TEP-C) using a conversion factor of 0.75 μg C μg L^{-1} / XGeq L^{-1} (Engel and Passow, 2001).

Several values of the biogeochemical measurements were considerably higher than the average concentrations at their collection depth. If at least twice the average concentration for that depth layer, a value was defined as an outlier; approximately 5% of the total number of observations were *outliers*. We refer to background concentrations when these outliers were removed to assess the baseline biogeochemical composition of suspended and sinking particles. The nature of the outliers and the implication of their presence is discussed in Section 4.5.

Abiotic aggregation potential experiments

The potential for the abiotic formation of aggregates was evaluated using rolling tanks experiments. Four experiments were conducted using MSC T_0 (August 25 at 95 m), *top* (August 25 at 95 m) or *base* (August 17 at 55 m and August 19 at 55 m and 95 m) sample fractions. Each experiment was conducted for 36 hours in 1.1 L rolling tanks at near in situ temperature (13°C or 4°C) in the dark. Aggregate formation was monitored by visually checking every 6 hours for the appearance of marine snow-sized particles (ESD >0.5 mm).

Settling time experiments for MSC

Methodological experiments to determine the effect of settling time on particle fraction partitioning were conducted twice (on August 20 and September 03; Table S1) on samples from MSC deployments at depths of 60 m and 80 m, respectively. Each time, all three MSCs were deployed at the same depth, but settling times after retrieval varied: particles were allowed to settle for 1, 2 and 4 hours after recovery of the MSCs. Subsamples of *top* and *bottom* fractions were analyzed for POC and PON, bSi, and TEP.

Calculations of particle concentrations and fluxes

Following Riley et al. (2012) and Giering et al. (2016), concentrations of suspended (c_{NS}), slow-sinking (c_{SS}) and fast-sinking (c_{FS}) particles were calculated as follows:

$$c_{NS} = \textit{top} \text{ concentration} \quad (2)$$

$$c_{SS} = (\textit{base} - \textit{top} \text{ concentrations}) \times V_{\textit{base}} / V_{MSC} \quad (3)$$

$$c_{FS} = (\textit{tray} - \textit{base} \text{ concentrations}) \times V_{\textit{tray}} / (A_{\textit{tray}} \times h_{MSC}) \quad (4)$$

Occasionally after applying the corrections, we obtained negative values; i.e., the *top* concentration exceeded the *base* concentration, or the *base* concentration exceeded the *tray* concentration. We assigned a zero concentration to the specific observations. The negative values could reflect a lack of sinking particles, the presence of ascending particles and/or actively moving zooplankton. In the analyses that follow, little differences were found between slow- and fast-sinking particle concentrations (Section 3.2). Hence, these two sinking particle fractions are combined. In four deployments, TEP and TC were measured

only in the *top* and *tray* fractions. In these cases, sinking TEP and TC concentrations were estimated following Equation 4 but subtracting the *top* fraction from the *tray* fraction.

The standard particle sinking velocity for the MSC is assumed to be 18 m d^{-1}, as determined geometrically by dividing the sinking distance (height of the MSC; $h_{MSC} = V_{MSC} / A_{MSC}$ = 1.5 m) by the settling time (t = 2 hours). We assumed that the 18 m d^{-1} sinking velocity estimate for sinking particles represents a lower bound estimate because the sinking particles could have reached the bottom of the MSC much sooner (Giering et al., 2016).

Statistical analyses

The relative uncertainties in the calculated concentrations and fluxes were determined by using a Monte Carlo error propagation, with mean values obtained by averaging the replicate filters and the precision estimated by calculating the average of the relative standard deviations of the filter replicates (Table S3). A 1% uncertainty was assumed for the measured values (V_{MSC}, A_{tray}, h_{MSC}, V_{base}, V_{tray}, h_{MSC} and sinking time). Final estimates of the averages and standard deviations of particle concentrations and fluxes were then calculated from the simulation results. Simple linear regression was used to test (Student's t-test, 95% confidence) for statistically significant temporal and depth trends displayed by the biogeochemical content of suspended and sinking particles, and their partitioning to total. The linear analyses were performed using the function fitlm in Matlab (R2021b). The same approach was used to test for significant temporal trends displayed by the biogeochemical content of suspended and sinking particles during the settling tests. Paired t-test was used to test for differences among particle fractions. The data presented in this study, and all the data generated during the first EXPORTS field campaign, can be found at NASA SeaBASS data repository (https://seabass.gsfc.nasa.gov/cruise/EXPORTSNP).

Results

Marine snow and abiotic aggregation potential

No visible sinking marine snow particles (diameter >0.5 mm) were found in the tray fractions from any of the MSCs deployments. This observation suggests that the concentration of sinking marine-snow-sized particles was less than 0.02 L^{-1}. Furthermore, during the four aggregation potential experiments, no visible marine snow-sized aggregates formed in the rolling tanks regardless of depth (55 m and 95 m) or sample fraction (T_0, *top* or *base*).

Particle concentrations and size

Most of the imaged particles (approximately 95%) were smaller than 16 µm in diameter (ESD), whether suspended or sinking (Figure 1). Furthermore, particle concentrations measured in the tray were equal to or lower than the ones measured in the base for 20 of 30 MSC deployments. These observations suggest that the concentration differences between *base* and *tray* particle fractions were too small to be detected with this method. We hence summed the concentrations of slow- and fast-sinking particles into a single sinking particle fraction. This decision is also supported by the lack of marine snow, which would have contributed appreciably to the fast-sinking particle fraction.

Our results, based on the analysis of particles with diameters (ESD) between 4 µm and 128 µm, suggest that >70% of suspended and sinking particles had a diameter of 4–8 µm and that particles larger than 32 µm were at the detection limit of our method (i.e., too rare to be quantified). The partitioning of particles across the size bins was consistent among particle fractions (paired t-test, p = 0.33–0.63, n = 17), indicating that suspended and sinking particles were of a similar size (Figure 1 and Table S4).

Additionally, we calculated the particle size distribution (PSD, 4–128 μm) of suspended particles and of sinking (*tray*) particles (uncorrected fraction) to assess differences in slopes among fractions with depth. Overall, throughout the entire water column, PSD slopes of suspended particles were similar (–3.3 ± 0.3, n = 17) to those of sinking particles (–3.5 ± 0.2, n = 17; Figure S1). Yet below 100 m, PSDs of sinking particles were significantly steeper than those of suspended particles (paired t-test, $p = 0.03$, n = 5*;* Figure S1). Furthermore, the slope of suspended PSD became significantly shallower with depth between 20 m and 500 m ($R^2 = 0.33$, $p < 0.02$, n = 17), while the slopes of sinking PSDs remained constant ($R^2 = 0.01$ $p = 0.75$, n = 17; Figure S1).

The determination of particle size using this approach is associated with uncertainties due to sample handling. We cannot exclude the possibility that fragile and larger aggregates (ESD > 0.5 mm) may have broken up due to physical disturbance developed during the sampling and partitioning of the three particle fractions and during injection of subsamples into the FlowCam flowcell used in combination with the 40x objective (minimum size of 300 μm). Therefore, the size characterization performed with the FlowCam must be taken with caution. Particle type and shape could not be resolved reliably with the FlowCam due to the small size of the particles.

Biogeochemical partitioning by particle sinking fraction

The background suspended POC concentrations decreased significantly with depth in the euphotic zone between 20 m and 65 m ($R^2 = 0.43$, $p = 0.03$, n = 11) and in the upper mesopelagic between 95 m and 500 m ($R^2 = 0.59$, $p = 0.001$, n = 14; Figure 2A), whereas background sinking POC concentrations did not attenuate significantly with depth ($R^2 = 0.01$, $p = 0.62$, n = 24). The relative contribution of background suspended POC to total

background POC decreased significantly in the upper mesopelagic ($R^2 = 0.70$, $p < 0.001$, n = 13), resulting in a concomitant increase in the contribution of the background sinking POC ($R^2 = 0.70$, $p < 0.001$, n = 13) (Figure 2A). Nearly all the background POC was found in suspended particles, which contributed to the total POC on average 89 ± 9% (n = 23). In respect to outliers, in 5 of 29 MSC deployments, the measured POC of either suspended or sinking particle fractions was at least twice as high as POC concentrations measured at other stations in the same depth layer (Table S5).

Patterns of PON (Figure S2) were similar to those of POC, with molar POC-to-PON ratios of the suspended fraction on average slightly higher than the Redfield ratio of 6.6 (average: 7.9 ± 3.9, n = 24). The molar POC-to-PON ratios did not show any trend with depth ($R^2 = 0.06$, $p = 0.25$) and were in general agreement with molar POC-to-PON ratios measured during the EXPORTS field campaign (Graff et al., n.d.). Molar POC-to-PON for sinking particles varied between 3 and 16 (average: 7.2 ± 3.8, n = 26) and did not show any significant trend with depth ($R^2 = 0.11$, $p = 0.10$).

PIC was below detection in 20% of the suspended particle fractions, and in 60% of sinking particle fractions. Suspended PIC concentrations increased significantly with depth ($R^2 = 0.40$, $p = 0.05$, $n = 10$; Figure 2B). Background sinking PIC was on average 0.4 ± 0.3 (n = 8) μg C L^{-1} and remained constant with depth ($R^2 = 0.05$, $p = 0.59$, n = 8). Background molar PIC-to-POC ratios calculated for suspended particles increased significantly with depth ($R^2 = 0.80$, $p < 0.001$, n = 10) and were significantly higher than PIC-to-POC ratios of sinking particles in the mesopelagic (paired t-test, $p = 0.01$, n = 5; Figure 3A).

Background suspended and sinking bSi concentrations and their contribution to total bSi concentrations did not change significantly with depth between 50 m and 500 m ($R^2 = 0.06$–

0.18, p = 0.17–0.49, n = 11; Figure 2C). Suspended particles stored on average 83 ± 9% (n = 10) of the total background bSi pool. Molar bSi-to-POC ratios associated with background suspended particles increased significantly with depth between 50 m and 500 m (R^2 = 0.84, p < 0.001, n = 8), whereas ratios of sinking particles remained constant (R^2 = 0.16, p = 0.32, n = 8). Furthermore, molar bSi-to-POC ratios of sinking particles were on average higher than the ratios associated with suspended particles above 95 m (n = 3), and lower between 350 and 500 m (n = 4). Ratios above and below 95 m were statistically different (paired t-test, p = 0.01 and p = 0.008, respectively; Figure 3B).

Suspended and sinking lSi concentrations and relative contribution to the total lSi pool showed high variability and did not display a significant trend with depth (R^2 = 0.004–0.19 p = 0.18–0.85, n = 11; Figure 2D). Suspended lSi accounted on average for 82 ± 19% (n = 10) of the total lSi pool. Molar lSi-to-POC ratios associated with suspended particles increased significantly with depth between 20 and 500 m depth (R^2 = 0.76, p < 0.005, n = 8). For sinking particles, molar lSi-to-POC ratios displayed the tendency of decreasing with depth between 20 m and 500 m, although the trend was not statistically significant (R^2 = 0.25, p = 0.21, n = 8; Figure 3C). Ratios between suspended and sinking particles differed statistically below the euphotic zone (paired t-test, p < 0.01), with suspended particles characterized by consistently higher ratios than sinking particles.

Suspended TEP decreased significantly with depth (R^2 = 0.53, p =0.001, n = 16) and, like POC, displayed the sharpest decrease between 50 m and 95 m. On average, 95 ± 4% of TEP was suspended, and sinking TEP was often at or near detection (average = 0.3 ± 0.2 µg XGeq L^{-1}, n = 15; Figure 2E). TEP concentrations measured in the MSCs were in line with the concentrations measured in the water collected with the CTD rosette (Figure S3). After

converting TEP to TEP-C, we estimated, in 11 of 15 deployments, that 15 ± 5% of suspended POC was TEP and only 3 ± 1% of sinking POC was TEP. In 4 observations collected above 100 m, TEP-C accounted for 13% of the sinking POC (Figure 3D). Ratios of TEP-C to POC associated with suspended and sinking particles were statistically different (paired t-test, $p < 0.001$, $n = 15$).

Background POC, TEP, bSi and lSi concentrations in the suspended and sinking particle pools did not display a significant variability over time at 50–65 m, 95 m or 300–500 m (t-test, 95% confidence). Temporal trend for PIC could not be tested owing to the limited number of observations available.

To provide an overall assessment of the relative changes in the measured biogeochemical composition of suspended and sinking particles with depth, we summed the background cruise-wide averaged concentrations of organic TEP-C, POC and PON, and ballast minerals and evaluated the differences in their relative contributions (Figure 4). We found that the composition of suspended particles was dominated by POC (62 ± 1%, $n = 2$) in the euphotic zone and on average ($n = 3$) by POC (30 ± 12%), lSi (36 ± 8%) and PIC (17 ± 9%) in the upper mesopelagic, whereas sinking particles were on average ($n = 5$) composed mainly of POC (50 ± 10%), followed by lSi (20 ± 7%), bSi (14 ± 7%) and PON (9 ± 3%) throughout the water column. The relative contribution of TEP-C in suspended particles was on average twice that in sinking particles (Figure 4B).

Constraining the particle sinking velocity

The settling time experiments showed no consistent differences in the fraction of sinking particles to the whole particle population (suspended plus sinking) as a function of settling time (t-test, 95% confidence). After 1, 2 and 4 hours of settling, sinking POC made up 10,

11 and 10%, and sinking PON 6, 7 and 8%, of the whole particle population (Table S6). Sinking bSi made up 23, 25 and 25%, whereas sinking TEP made up 6, 3 and 5%; Table S6). Thus, the concentrations of POC, PON, bSi and TEP in sinking particles were effectively the same regardless of the settling time. However, our experiment was limited to only two casts within the euphotic zone; hence, we cannot assume that all sinking particles collected had the potential to sink within one hour at 36 m d^{-1}. We therefore present fluxes calculated assuming the standard sinking velocity of 18 m d^{-1}, and we reinforce that these fluxes represent a lower bound as suggested by our settling time experiments (Figure 5). Background POC fluxes averaged 4.3 ± 2.5 (n = 9), 3.1 ± 1.5 (n = 7) and 3.1 ± 1.1 (n = 6) mmol C m^{-2} d^{-1} at 50–65 m, 95 m, and 300–500 m, respectively. When including the outliers, the estimates increased to 7 ± 10 (n = 10), 9 ± 18 (n = 8) and 4 ± 2 (n = 7) mmol C m^{-2} d^{-1}, respectively, at these same depth intervals. Fluxes of bSi averaged 0.2 (n = 3), 0.2 (n = 3) and 0.1 (n = 4) mmol Si m^{-2} d^{-1} and lSi fluxes 0.3 (n = 4), 0.4 (n = 3) and 0.2 (n = 4) mmol Si m^{-2} d^{-1}, at 50–65 m, 95 m and 300–500 m, respectively.

Discussion

In this discussion, we first put our results into the overall cruise context and then focus on the causes that drive the differences between the suspended and sinking particles as measured with the MSC. Specifically, we discuss why – despite all particles being small – some particles sank while others remained suspended. Furthermore, we discuss the potential mechanisms that can explain the presence of small, slowly sinking particles in the mesopelagic. We finally address several aspects of the methodology by comparing sinking particle fluxes derived from different methods and interpreting the observed outliers in our

data set and their implications, including the potential role of 'patchiness' in ocean particle distributions.

Comparison with other particulate biochemical measurements made during EXPORTS: consistency in responses by size

A variety of methods and sampling equipment were used to measure the biogeochemical composition of particulate matter during the first EXPORTS field campaign (Siegel et al., 2021). Values of POC and PON measured in the MSC T_0 fraction were slightly higher than those obtained from the 12 L Niskin bottles sampled from the CTD/rosette system from the same ship (Graff et al., n.d.). The differences between the two measurements may be explained by a combination of the following: 1) under-sampling of sinking particles by Niskin bottles compared to the MSC, 2) slight overestimation of MSC POC values due to a possibly higher POC blank than the one used to correct the measured POC masses (Section 2.4), and 3) spatiotemporal differences in sampling (Graff et al., n.d.).

Our PIC concentrations were low but consistent with low productivity regimes in the global ocean (Mitchell et al., 2017) and complementary measurements made at Station P during EXPORTS (Roca-Martí et al., 2021), suggesting a limited presence of calcifying microorganisms. In situ pump observations showed low PIC concentrations and small contributions to particle stocks during EXPORTS (Roca-Martí et al., 2021). Our PIC estimates were higher than the in situ pump observations, which may be attributed to the use of a larger filter pore size with in situ pumps (QMA; 1.0 μm nominal pore size) compared to the smaller pore size of glass fiber filters used with Niskin bottles and MSC analyses (GF/F; 0.3 μm nominal pore size after combustion; Nayar and Chou, 2003; Graff et al., n.d.). Indeed, during EXPORTS, most of the PIC was associated with the smallest size particle

fraction measured by in situ pumps (i.e., in the 1–5 μm fraction rather than the 5–51 μm or >51 μm fraction; Roca-Martí et al., 2021).

Our measurements of bSi standing stocks were in good agreement with measurements performed on seawater collected with Niskin bottles (Brzezinski et al., 2022) and measurements obtained with in situ pumps (Roca-Martí et al., 2021), which used similar pore sizes (0.6, 0.6 and 0.8 μm, respectively). Our molar bSi-to-POC ratios associated with suspended and sinking particles were in the same range as the 1–51 μm particle size fractions (bSi:POC = 0.03–0.16; Roca-Martí et al., 2021), except for one outlier (0.35 at 500 m; Section 4.5). Molar bSi-to-POC ratios measured from larger sized particles with in situ pumps and drifting sediment traps were higher (Roca-Martí et al., 2021; Estapa et al., 2021). This comparison suggests that the MSC sampled on average small particles (<51 μm) and under-sampled large particles, and that using GF/F filters allowed a better representation of particles <1 μm in diameter than in situ pumps. Overall, the concentrations and flux values (see also Section 4.4) obtained by the MSCs agreed with other measurements obtained during the cruise; we are therefore confident that the MSC observations are representative of the conditions present in situ during our visit.

Partitioning of TEP and ballast minerals in suspended and sinking particles

When comparing sinking to suspended particles, we expected to find either larger particles or a higher ratio of ballast materials to POC (or both) in the sinking fraction. However, neither expectation was met (Figures 1, 3 and 4). Both fractions were characterized by small particles which, from a simplistic view, would suggest that sinking particles contained a higher fraction of ballast material than suspended particles. Contrary to this idea, however, suspended particles were characterized by the higher ratio of ballast

material in the mesopelagic. This finding begs the question of why the small non-ballasted particles sank (and, why the ballasted particles did not sink).

The partitioning of particles into suspended and sinking pools must have been controlled by another factor. So far, we looked at the composition in context of the traditional constituents: POC, PIC and silicate. However, the molecular makeup of POC can have a large effect on particle density. For example, diatoms have been shown to be positively buoyant (i.e., float; Villareal, 1988; Moore et al., 1996; Woods et al., 2008); however, the phytoplankton community consisted predominantly of very small non-diatom cells (McNair et al., 2021). Alternatively, TEP are positively buoyant and thus could reduce the sinking velocity of aggregates (Engel and Schartau, 1999; Azetsu-Scott and Passow, 2004). Overall, we observed low concentrations of water column TEP between 5 m and 500 m (17.3–1.2 µg XGeq L^{-1}). This result is in line with low productivity systems such as the Southern Ocean (from undetectable values to 48 µg XGeq L^{-1}; Ortega-Retuerta et al., 2009), the tropical western Pacific Ocean (5.3–40 µg XGeq L^{-1}; Yamada et al., 2017), the Eastern Mediterranean Sea (5.7–25.1 µg XGeq L^{-1}; Ortega-Retuerta et al., 2019) and the Indian and subtropical South West Pacific oceans (<20 µg XGeq L^{-1}; Engel et al., 2020). Despite the observed low TEP concentrations, TEP-C accounted for approximately 15% of the suspended POC pool. According to theoretical calculations, a 1 mm aggregate composed solely of TEP, and diatoms can sink only if less than 5% of its carbon content consists of TEP (Mari et al., 2017). Here we show that the relative contribution of TEP-C was on average three times that threshold (15%) in suspended particles, while in sinking particles on average only 3% of the POC was TEP. While the model used diatoms as the primary particle pool, in our case most of the suspended particle pool consisted of very small cells

(*Synechococcus* spp, picoeukaryotes and nanoeukaryotes; McNair et al., 2021), and possibly fragments of old cells, minerals, and detritus. Nonetheless, our data support the model implication (Mari et al., 2017) and provide evidence that the chemical composition of POC, and especially the contribution of organic exudates, is critical to understanding particle sinking velocity.

Hence, the higher TEP-to-POC ratio in suspended particles compared to sinking particles may have led to the difference in the partitioning of the two particle fractions as collected by the MSC by reducing the sinking velocity of small, ballasted particles that in the absence of TEP would have been part of the collected sinking fraction. Whereas the suspended POC was associated with ballasting material and consisted of a large fraction of TEP, the sinking POC consisted of relatively small fractions of ballasting material and TEP. This result suggests that the ratio of ballasting material to POC cannot be used as a sole predictor for sinking velocity, but that organic carbon composition needs to be considered.

The importance of TEP for potentially reducing sinking velocity and thus flux was first suggested by Mari et al. (2017), and here we present the first in situ measurements suggesting that high TEP concentrations reduce particle sinking velocities. Yet, our observations are limited to one field campaign only, and hence we cannot generalize. We observed this phenomenon in a low productivity system where particle concentrations were low and TEP concentrations were high. Our dataset was collected during late summer, when the system was characterized by low concentrations of chlorophyll *a*, nutrients, particles, and ballast minerals (Siegel et al., 2021; Roca-Martí et al., 2021; Brzezinski et al., 2022). The TEP-to-POC ratio may have been higher compared to other seasons, due to stressful conditions for phytoplankton growth and high light levels (Ortega-Retuerta et al. 2009),

implying that the observed mechanisms could be seasonal (Mari et al., 2017). Regardless, our data suggest that future biological pump studies should characterize POC composition, including TEP, to help gain a mechanistic understanding of how these gels influence particle sinking velocities and, in turn, the role of particle dynamics in ocean biogeochemical cycles across different productivity systems and seasons.

Potential mechanisms explaining small particles at depth

Our observations suggest that suspended particles were increasingly reworked with depth; e.g., a larger fraction of POC was remineralized with depth, leading to the relative increase in the ratio between ballasting material and POC with depth. Sinking POC did not decrease with depth, suggesting that either the attenuation of the sinking particle population was negligible, or an input of sinking material balanced the expected losses. If we assume that sinking particles collected at 500 m were produced at 30 m (within the mixed layer) and sank at 18 m d^{-1}, those particles would require 26 days to reach 500 m. We can estimate the loss rate assuming a temperature-dependent remineralization rate of 0.04 d^{-1} measured experimentally using a temperature of 7°C (average temperature between 30 and 500 m from CTD data) and a Q_{10} of 3.5 (Iversen and Ploug, 2013; Giering et al., 2017). If particles were to sink undisturbed, 30% of the POC would have been remineralized by bacteria during that time window (26 days). Yet, such a decrease was not observed.

One theoretical explanation for a lack of flux attenuation of sinking particles would be rapid physical transport processes (Omand et al., 2015; Giering et al., 2016; Siegel et al., 2023). Particle subduction or convective mixing can be excluded, however, as during our visit density stratification beneath the mixed layer was strong and consistent and lateral density gradients were weak (Siegel et al., 2021).

Alternatively, an input of sinking particles at depth may have balanced their loss. Large sinking phytodetrital aggregates were rare, implying that disaggregation of sinking aggregates was not the prevailing source of small sinking particles. However, if suspended POC existed as loosely packed aggregates within a buoyant TEP matrix (e.g., low-density aggregates; Mari et al., 2017), their disaggregation would allow dense components to sink, albeit at a relatively slow velocity. Such disaggregation could be caused by zooplankton (Passow and Alldredge, 1999) or by microbially mediated degradation processes (Passow, 2002). During microbially mediated degradation, lighter C-components may be consumed preferentially, leaving denser and more recalcitrant material in the sinking fraction (Hamanaka et al., 2002). In fact, extracellular particulate carbohydrates released by phytoplankton (i.e., TEP) are remineralized by bacteria at a faster rate than non-TEP carbon (i.e., 0.53 and 0.21 d^{-1}, respectively; Harvey et al., 1995; Mari et al., 2017).

Particle flux was dominated by fecal pellets during EXPORTS (approximately 80%; Durkin et al., 2021; Steinberg et al., 2023). Specifically, mini-pellets (ESD <100 μm) contributed up to 46% of the total carbon flux in the upper mesopelagic (Durkin et al., 2021), with mesozooplankton and salp pellets contributing the majority of the sinking flux (Durkin et al., 2021; McNair et al., 2023). Fragmentation of fecal pellets, e.g., due to sloppy feeding or swimming motions (Steinberg and Landry, 2017), could have produced small and dense particles, which may have constituted the bulk of the small sinking particle pool we collected. Such pellet fragments would likely contain a high percentage of organic carbon and a low percentage of TEP, similar to our sinking particle pool. Though we did not observe large fast-sinking pellets in the MSCs, this absence could have been caused by an overall low abundance of pellets or because the MSCs were deployed during the daytime

when a large fraction of the zooplankton community likely resided at depth (e.g., Steinberg et al., 2023).

Microzooplankton grazing of suspended POC, and the resulting production of mini-pellets (Stemmann et al., 2004), may have also contributed to the production of small, dense sinking particles. Consumption of small particles by zooplankton and incorporation of their carbon and biogenic silica into sinking particles (Dagg et al., 2003) is especially important for carbon flux if it occurs within relatively short-path food webs (Richardson, 2019). This mechanism could also have been important during our study: compound-specific isotope analyses performed during our field campaign (Connor Shea, personal communication, 2023) found that the mesopelagic zooplankton food web at Station P was based mainly (72–96%) on small particles (<6 μm).

Although we cannot say with certainty why sinking flux of POC did not decrease with depth, likely a series of biologically mediated aggregation or fragmentation processes led to a replenishment of the small sinking particle pool at depth. The described mechanisms are potentially significant contributors in dictating the efficiency of the biological carbon pump, especially in stable low-productivity systems, characterized by small particles in low concentrations.

Comparison of fluxes derived from different methods during EXPORTS

Our background POC fluxes compared to the cruise mean POC fluxes, obtained using both neutrally buoyant and surface-tethered sediment traps (Estapa et al., 2021) and water column Thorium-234 assessment (Buesseler et al., 2020), were similar in the upper 100 m, but larger below 100 m (Figure 6). These differences between the estimates for depths >100 m existed even when the lower-bound estimate (assuming a sinking velocity of 18 m d^{-1};

Section 3.4) was used. In contrast, bSi flux estimates obtained from the MSC were in good agreement with those derived from the traps, but lower than the Thorium-234-based values (Roca-Martí et al., 2021; Figure 6).

These three approaches for determining sinking particle fluxes differ in the design, spatiotemporal resolutions, and size of collected particles; thus, they may not be directly comparable, and comparisons should be made cautiously. The approaches mainly diverge in four ways: temporal coverage, spatial coverage, and minimum and maximum size of collected particles. Temporally, the MSC provided virtually instantaneous estimates, whereas drifting sediments trap (Gardner, 1977) and water column Thorium-234 carbon flux determinations (Buesseler et al., 1992) integrate over periods of 3–6 days (time to collect sinking particles) and 24 days (the half-life of ^{234}Th), respectively. Spatially, the MSC deployments have the smallest spatial resolution among these methods, with 39 discrete deployments as each MSC deployment assesses the flux from a single, approximately 100 L sample. Drifting sediment traps sampled sinking particles from an area ≤10 km^2 (Siegel et al., 2008). Due to the long integration times and abundance of samples (nearly 1000), ^{234}Th particle fluxes average over even larger spatial scales. In terms of minimum size of collected particles, differences in pore sizes of filters can lead to differences in measured biogeochemical concentrations. Here we measured POC using filters with a pore size of approximately 0.3 μm, while POC from sediment traps (Estapa et al., 2021) and water column Thorium-234 samples (Buesseler et al., 2020) were determined using filters with a pore size of approximately 1 μm. The filter pore sizes used to estimate bSi were 0.6 μm, approximately 1 μm and 0.8 μm for MSC, sediment traps and Thorium-234, respectively. Additionally, drifting sediment traps often underestimate small particles due to

hydrodynamics (Buesseler et al., 2007). In terms of maximum size of collected particles, the MSC likely under-sampled the rare larger particles as it collects a limited amount of seawater. During EXPORTS, sediment trap samples were highly impacted by zooplankton "swimmers" and fluxes were corrected to account for the removed biomass (Estapa et al., 2021).

The potential sources of discrepancies between fluxes measured from sediment traps and water column Thorium-234 were addressed in Estapa et al. (2021). Briefly, Thorium-234 fluxes measured in sediment traps were roughly 3-fold smaller than water column Thorium-234 fluxes. The different temporal coverages did not play a major role due to the stability in production and export before the EXPORTS cruise (McNair et al., 2023). The mismatch was attributed largely to under-sampling of both small particles (<32 μm) due hydrodynamic biases and rare, large particles (>1 mm) and zooplankton active-migrant flux by the sediment traps (Estapa et al., 2021). The size of particles collected in the polyacrylamide gel traps, which ranged from 75 to 1461 μm (median of 282 μm), supported this hypothesis (Estapa et al., 2021). Estimates from the MSC account for the contribution of those small particles close to approximately 0.3 μm. Thus, the discrepancy between MSC and sediment traps may be partially explained by an under-characterization of very small (<1 μm) particles by the traps. We cannot assess whether this statement is applicable when comparing to Thorium-234-based POC fluxes. Th-derived POC fluxes were estimated assuming the POC/Th ratios of 5–51 μm particles, which should be representative of all sinking particles regardless of their size (Buesseler et al., 2020).

However, the MSCs did not capture large, rare particles such as aggregates, salp fecal pellets or the active flux due to migration (Steinberg et al., 2023). We would therefore have

expected to see the opposite trend: higher flux measured by traps if large, rare particles played an important role in overall flux at the site. This comparison suggests that POC flux from the MSCs is at least partially complementary to those measured from Thorium-234 and traps. Most importantly, it suggests that small sinking particles were a relevant part of the sinking POC flux in the upper mesopelagic zone, likely exceeding the contribution of rare, large sinking particles. The fact that the MSCs and sediment traps produced similar estimates of bSi fluxes reinforced our finding that the population of sinking particles collected by the MSCs included small sinking particles of organic carbon missed by the other methods, whereas bSi, which was mostly associated with slightly larger particles (Roca-Martí et al., 2021; Estapa et al., 2021; Brzezinski et al., 2022), was equally sampled by all three methods.

Outliers – patchiness or artifacts?

The dataset obtained from the MSC holds the potential of highlighting patchiness in the ecosystem through the collection of spatially heterogeneous features. Patchiness in the ocean exists both vertically and horizontally spanning from the microscale to the mesoscale (Cassie, 1962; Siegel, 1998; Robinson et al., 2021) and is in general difficult to map with most oceanographic approaches (McNair et al., 2023). Several of our biogeochemical measurements resulted in values considerably higher than average concentrations for their collection depth (Figure 2, Table S5). These "outliers" may be attributed to patchiness or could be due to methodological artifacts. Methodological artifacts could be caused by misfiring of the MSCs at a shallower depth than intended or by contamination of the filter. The latter is improbable as replicate filters and comparisons between T_0 and suspended plus sinking particle fractions would have indicated "contamination". Additionally, filters were

always inspected visually for visible particles, such as macrozooplankton, which, if present, were removed. These outliers were specific to the MSC; no outliers were detected by the 12 L Niskin bottles of the CTD on board R/V *Roger Revelle*.

Three of the five outliers in POC were observed on August 16, at 55 m, 95 m, 195 m, one on August 21 at 195 m, and one on September 1 at 350 m. The outlier concentrations of sinking POC measured at 55 m and 95 m, which were an order of magnitude higher than any other sinking POC values, are likely reflective of in situ patchiness: the respective T_0 and suspended POC concentrations were also within the upper range of the values measured at those depths. The POC measured in the T_0 fraction at 55 m equals the sum of POC measured in the suspended and sinking particle fraction, confirming that the MSC samples were not contaminated. Associated sinking PON values were also marked as outliers and the molar C-to-N ratios were reasonable (10.4 and 12.5 at 55 m and 95 m, respectively), albeit somewhat higher than those of the T_0 and suspended fractions (7.3 and 6.4 at 55 m and 8.3 and 9.7 at 95 m, respectively). Lastly, while the associated sinking TEP concentrations were high (with the observation at 95 m being an outlier), suspended TEP concentrations agreed with TEP measured from water collected with Niskin bottles at those depths (Figure S3). These observations and the fact that the MSC deployment depths were chosen specifically to target "interesting" areas as seen by the CTD or UVP profiles, lead us to believe that the 100 L sample we collected may have included patches of unusually high biochemical concentrations.

The three outlier POC concentrations for suspended POC at 195 m, 195 m and 350 m were associated with outlier values of PON, and could reflect POC and PON concentrations measured at 50–65 m. However, the associated suspended TEP concentrations (2.8, and 3.1

μg XGeq L^{-1}) suggest samples stemmed from below 50–65 m (Figure S3). Although uncertain, these concentrations could also reflect patchiness.

One value of biogenic silica (176 nmol Si L^{-1}) at 500 m was >3-fold higher than the bSi measured on other days at that depth either with the Niskin bottles or the MSC (57 and 45 nmol Si L^{-1}, respectively). However, associated POC concentrations were consistent with the deployment depth, and the molar bSi-to-C ratio of this observation (0.35) matched the one measured for particles >5 μm (bSi:POC = 0.16–0.94) collected with in situ pumps (Roca-Martí et al., 2021). Thus, we assume that this sample included a higher-than-average presence of diatoms or Rhizaria. Hot spots of bSi accumulation have previously been found in low productivity systems (Crombet et al., 2010), and this depth was targeted because the UVP profile directly before the MSC deployment indicated a Rhizaria maximum. Similarly, the elevated PIC concentration associated with sinking particles (21.5 μg PIC L^{-1}) could potentially be attributed to the presence of foraminifera test fragments or coccoliths.

In summary, the "outliers" measured with the MSC are likely reflective of patchiness in concentrations of small particles in this low productivity system. Patchiness in the distribution of salp swarms was also a prevalent feature during this study (Steinberg et al., 2023). The sporadic nature of patchiness is challenging to quantify and its importance with respect to standing stocks and fluxes of an entire ecosystem hard to assess, especially in a low productivity system.

Summary and conclusions

Small, slowly sinking particles are usually under-sampled by canonical particle collection methods and thus have been poorly characterized. Hence, little is known about their origins, biogeochemical composition, and role in the ocean biogeochemical cycles.

Our study shows that suspended and sinking particles were small and similarly sized. Unexpectedly, sinking particles were not characterized by a higher contribution of ballast materials (bSi, lSi and PIC), which would have justified their sinking behavior. However, they displayed low TEP-to-POC ratios in comparison to suspended particles. This observation suggests that high TEP contribution may have increased the residence time of suspended POC and thus reduced sinking particle fluxes, impacting the efficiency of the biological carbon pump. Hence, we suggest that the composition of POC (i.e., presence of gels like TEP) should be measured routinely to assess how it affects the sinking of particles.

Our data together with other findings from the field campaign support the hypothesis that the pool of small sinking particles in the mesopelagic formed via fragmentation of sinking fecal pellets and zooplankton-mediated repackaging of suspended particles into fecal pellets. A smaller contribution to the small sinking particulate pool may have been provided via the disaggregation of low-density suspended aggregates. Such mechanisms may be especially important in low productivity systems during late summer months.

A comparison between particle fluxes calculated from the MSC and fluxes measured with drifting sediment traps and Thorium-234 suggests that small slowly sinking particles exceeded the contribution of rare, large sinking particles to POC flux in the upper mesopelagic. Our data suggest that such flux of small sinking particles tends to be underestimated by trap and Thorium approaches. Potentially this flux of small sinking particles may contribute towards resolving the budget discrepancies between sinking flux and metabolic carbon requirements in the mesopelagic (Burd et al., 2010).

Figures

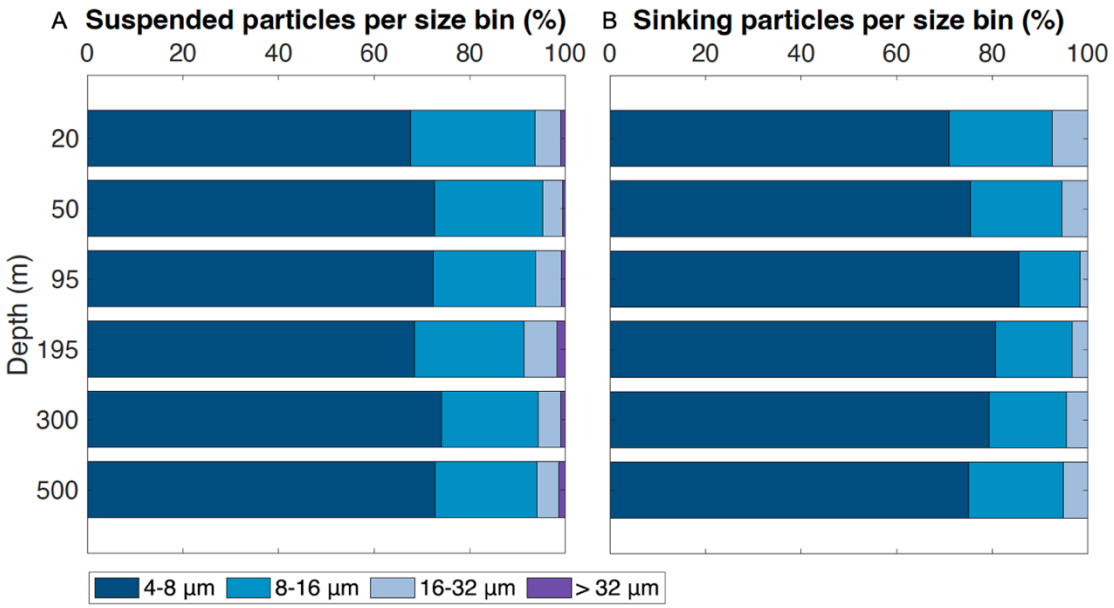

Figure 1. Relative contribution of particle abundances per size (4 to >32 µm) versus depth. Bar plots display the contribution (%) of A) suspended and B) sinking particle concentrations in 4 size bins based on the octave scale (4–8, 8–16, 16–32 and >32 µm) and on the particle equivalent spherical diameter. Concentrations are calculated as cruise-wide averages for 6 depth layers (20–25 m, 50–65 m, 95 m, 195 m, 300–350 m and 500 m). Numbers of stations per depth layer are 2, 10, 10, 2, 4 and 2, respectively, for bins between 4 µm and 32 µm and 2, 4, 5, 2, 2 and 1 for the largest size bin (>32 µm). Sinking particles (>32 µm) were at the detection limit of our method.

A

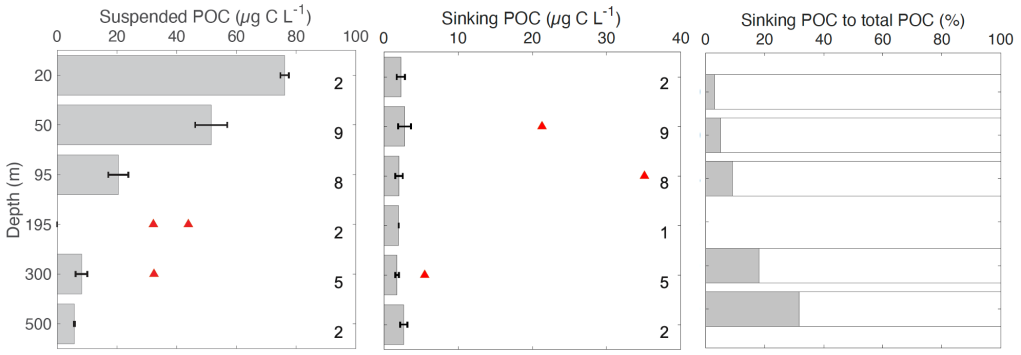
Suspended POC (μg C L-1)
Sinking POC (μg C L-1)
Sinking POC to total POC (%)
Depth (m)
20
50
95
195
300
500

B

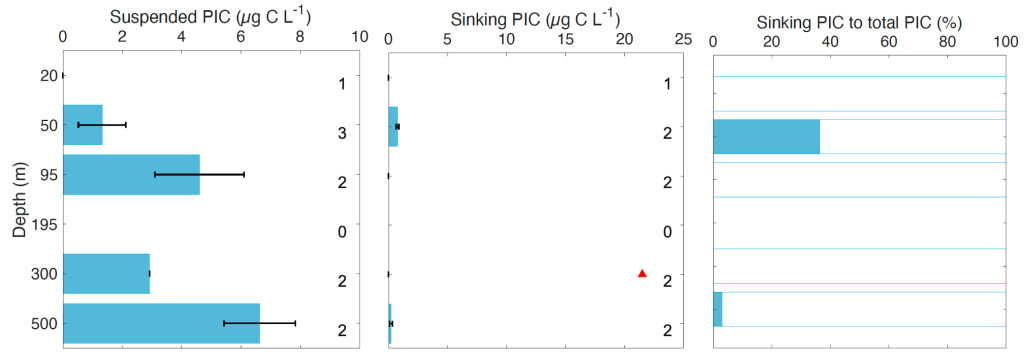
Suspended PIC (μg C L-1)
Sinking PIC (μg C L-1)
Sinking PIC to total PIC (%)
Depth (m)
20
50
95
195
300
500

C

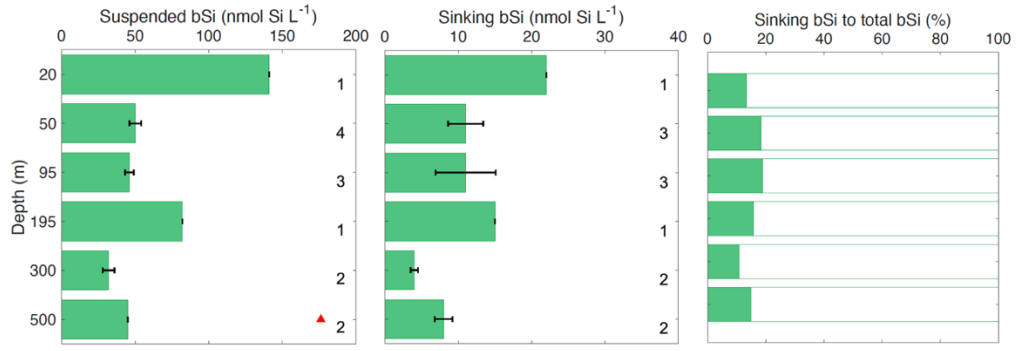
Suspended bSi (nmol Si L-1)
Sinking bSi (nmol Si L-1)
Sinking bSi to total bSi (%)
Depth (m)
20
50
95
195
300
500

D

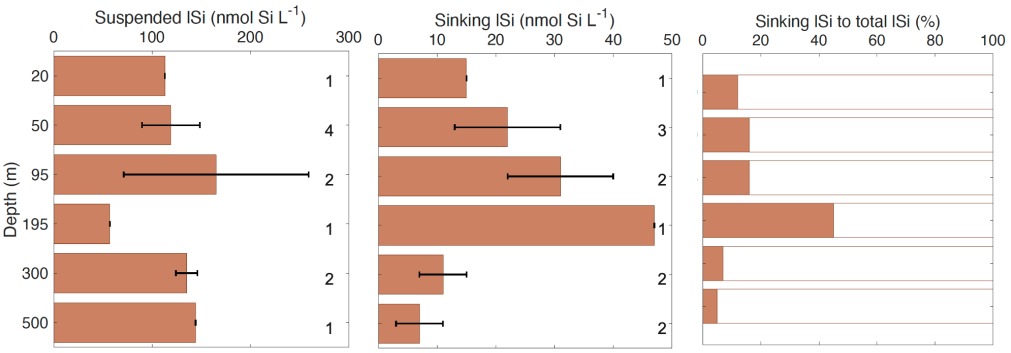
Suspended lSi (nmol Si L-1)
Sinking lSi (nmol Si L-1)
Sinking lSi to total lSi (%)
Depth (m)
20
50
95
195
300
500

E

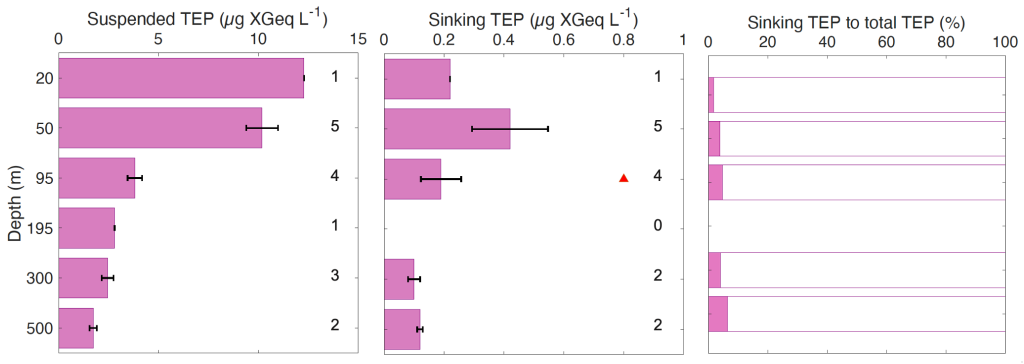

Figure 2. Concentrations of biogeochemical components in suspended and sinking particles and contributions of sinking to total. Bar graphs display time-averaged concentrations of A) particulate organic carbon (POC), B) particulate inorganic carbon (PIC), C) biogenic silica (bSi), D) lithogenic silica (lSi), and E) transparent exopolymer particles (TEP) in (left) suspended particles and (middle) sinking particles, along with (right) the contribution (%) of sinking particle to total concentrations. Outliers are represented as red triangles. The values are cruise-wide averages calculated for six depth layers (20–25 m, 50–65 m, 95 m, 195 m, 300–350 m and 500 m). Error bars are the standard deviations of the concentrations averaged within each depth layer and thus reflect dataset variability rather than the propagated uncertainty of each datapoint. Numbers to the right of each bar indicate total number of observations per depth layer including outliers. The differences in number of observations between sinking and suspended particles reflect loss of samples during analysis. Note differences in scales.

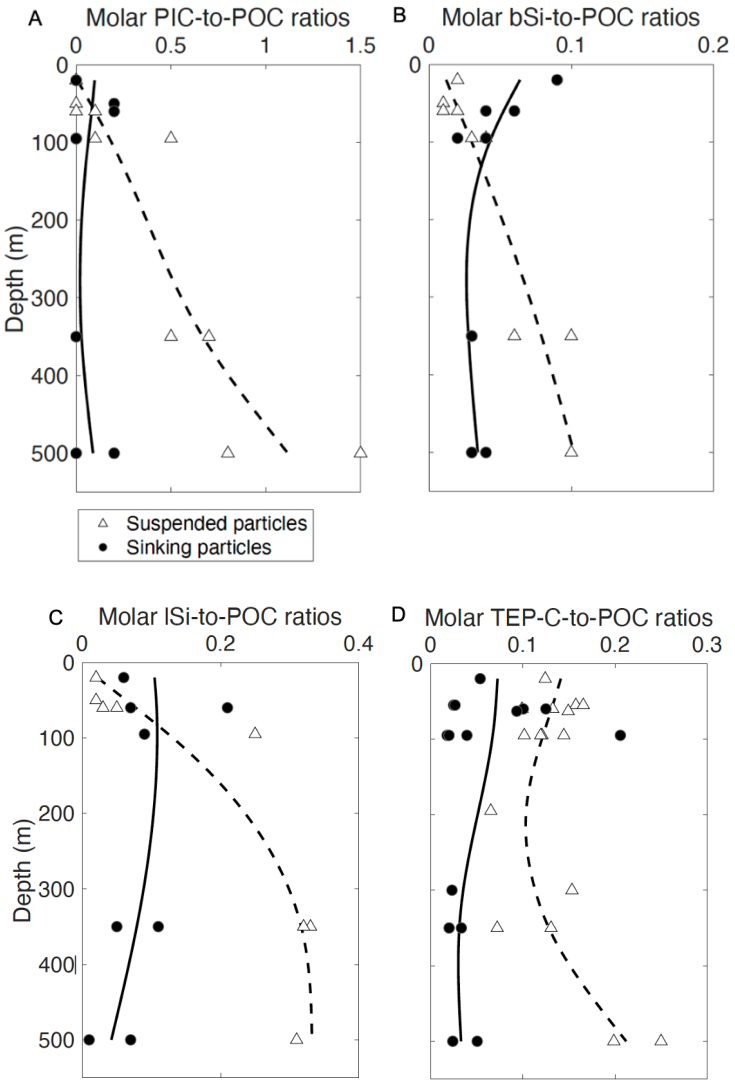

Figure 3. Ratios of ballast minerals and TEP to POC in suspended and sinking particles with depth. Depth profiles of molar ratios of A) particulate inorganic carbon to particulate organic carbon (PIC:POC), B) biogenic silica to POC (bSi:POC), C) lithogenic silica to POC (lSi:POC) and D) transparent exopolymer particles to POC (TEP-C:POC) calculated for suspended (white triangles) and sinking (black circles) particles. Dashed and continuous lines are smoothing spline used to enhance visualization of trends and thus do not have statistical significance. Outliers of the suspended molar bSi-to-POC ratio (0.35 at 500 m) and sinking PIC-to-POC ratio (12.4 at 350 m) have been removed to better display depth trends, which are not affected by their exclusion.

A

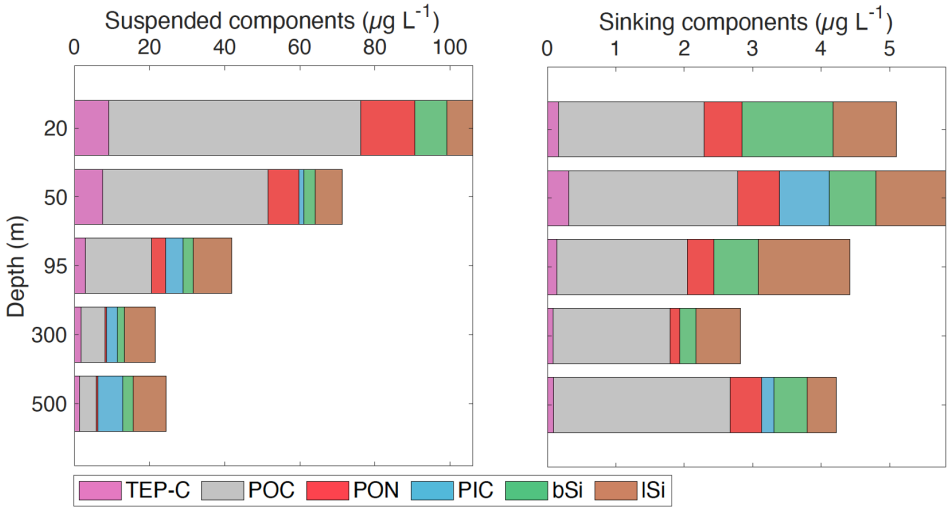

B

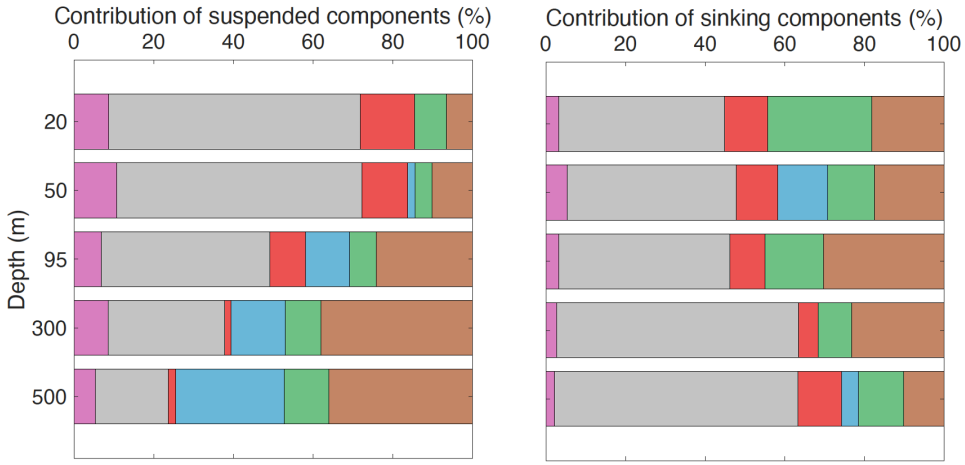

Figure 4. Concentrations of organic and inorganic components in suspended and sinking particles and contributions to totals. Bar plots display A) the summed biogeochemical concentrations (in µg L^{-1}) of the measured organic (TEP-C, POC, PON) and inorganic (PIC, bSi and lSi) components and B) their relative contributions (%) in (left) suspended and (right) sinking particles at five depth layers (50–65 m, 95 m, 300–350 m and 500 m). Biogenic silica (bSi) and lithogenic silica (lSi) were converted to mass units using a molar mass of 61 g mol^{-1}. Here we display particulate organic carbon (POC, grey) as total POC minus transparent exopolymer particle carbon (TEP-C). The compositional plots display background concentrations; i.e., outliers were removed.

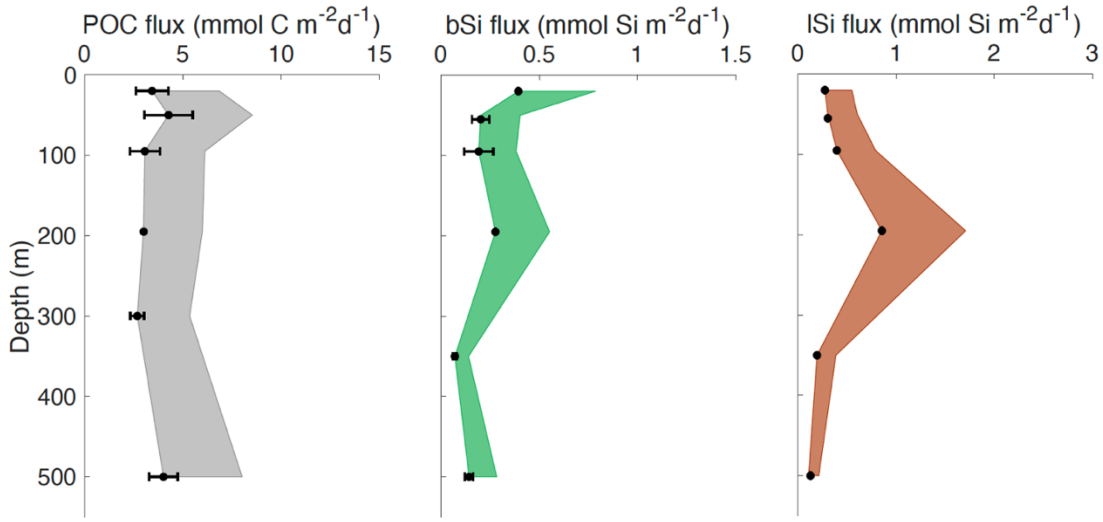

Figure 5. Calculated fluxes of particulate organic carbon, biogenic and lithogenic silica with depth. Plots represent fluxes of particulate organic carbon (POC, grey), biogenic silica (bSi, green) and lithogenic silica (lSi, brown) calculated using the background biogeochemical concentrations (outliers removed) and a conservative sinking velocity of 18 m d^{-1}. The filled area represents the upper bound fluxes estimated using a sinking velocity of 36 m d^{-1}. The values are cruise-wide averages calculated for five depth layers (50–65 m, 95 m, 195 m, 300–350 m and 500 m). Error bars are standard deviations averaged within each depth layer and thus reflect the dataset variability rather than the propagated uncertainty of each datapoint. Only one observation is available for each biogeochemical component at 195 m and only one for bSi and lSi at 20 m; hence, these depths are not well represented by our dataset.

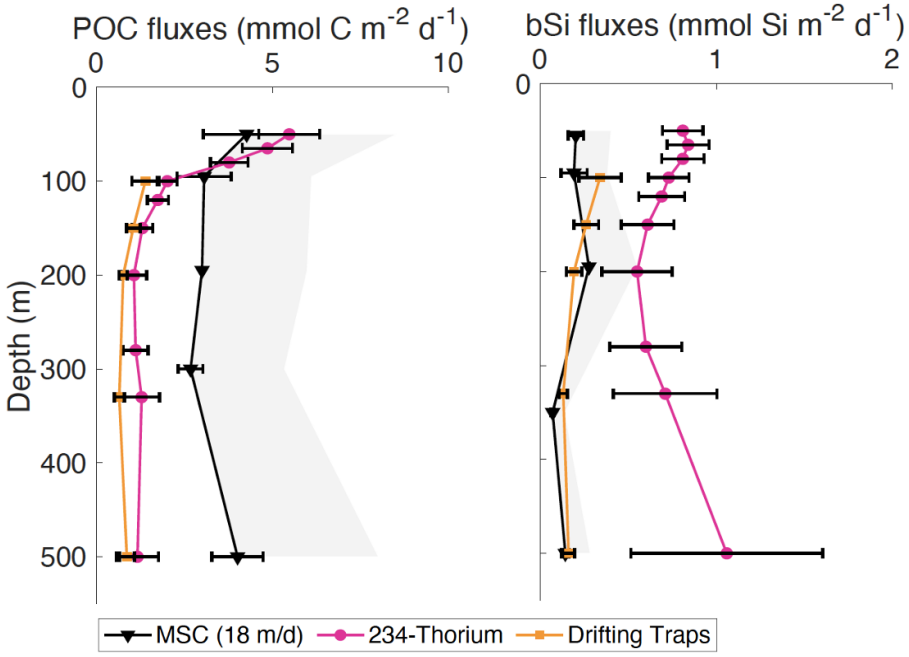

Figure 6. Comparison of particulate organic carbon and biogenic silica fluxes estimated using different approaches during EXPORTS. Depth profiles of fluxes of (left) particulate organic carbon (POC) and (right) biogenic silica (bSi) obtained from the Marine Snow Catchers (MSC), assuming sinking velocities of 18 m d^{-1} (black triangles) to 36 m d^{-1} (filled area), from Thorium-234 assessment (pink circles; Buesseler et al., 2020), and from drifting sediment traps (orange squares; Estapa et al., 2021). The MSC fluxes are calculated using the background biogeochemical concentrations (outliers removed). The 195 m depth is not well represented as only one POC and one bSi observation are available for that depth.

Supplemental material

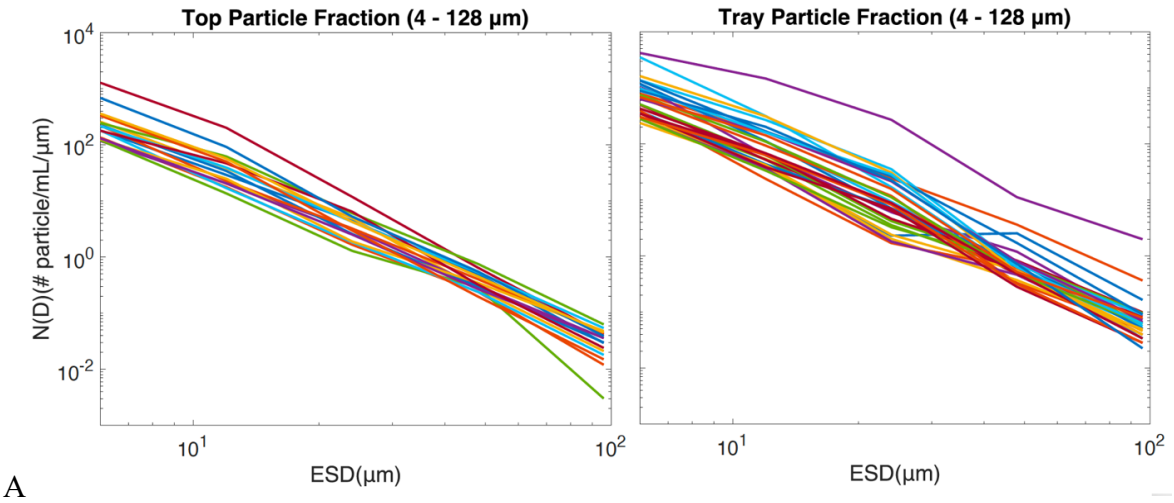

A

B

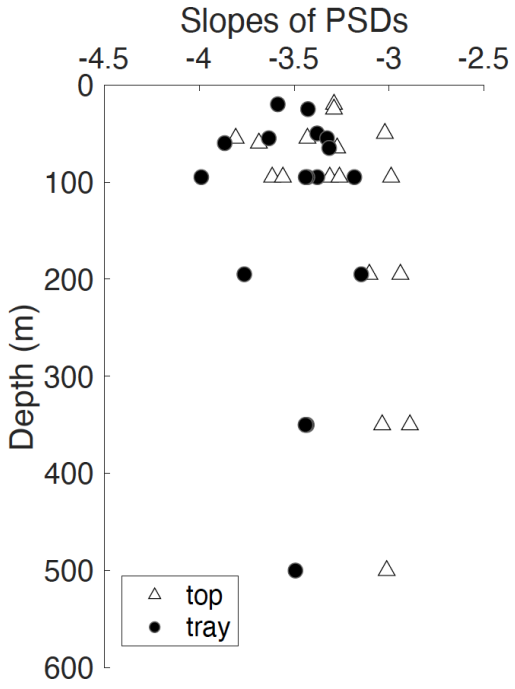

Figure S1. Particle size distribution (PSDs) of *top* and *tray* particle fractions. Panel A shows PSDs calculated using particle concentrations of *top* and *tray* fractions with Equivalent Spherical Diameter (ESD) between 4 µm and 128 µm. Panel B display PSDs slopes versus depth of *top* (white squares) and *tray* (black circles) particle fractions.

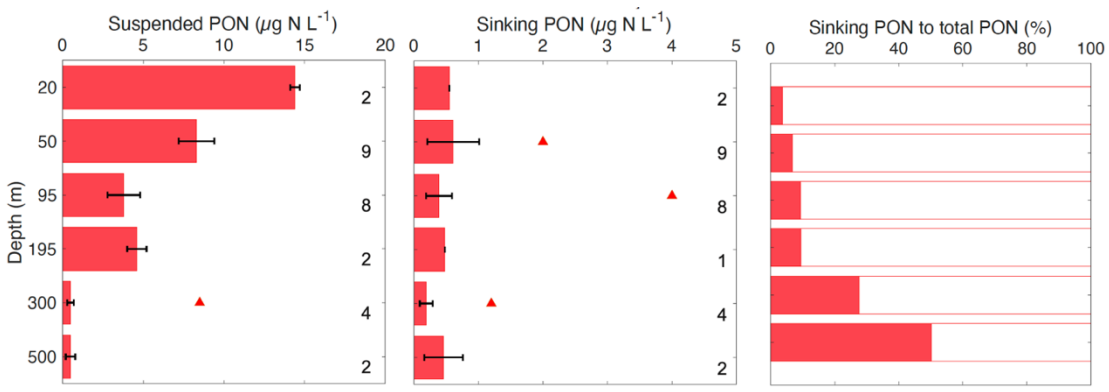

Figure S2. Time-averaged concentration of PON in suspended and sinking particles and the partition of sinking particles to total. Bar graphs display background suspended (left) and sinking (middle) and the fractional contribution of sinking particle concentrations to the total (in %; right) for PON concentrations. Outliers are represented as red triangles. The values are cruise-wide averages calculated for six depth layers (20–25 m, 50–65 m, 95 m, 195 m, 300–350 m and 500 m). Error bars are the standard deviations of the concentrations averaged within each depth layer and thus are reflective of the dataset variability rather than the propagated uncertainty of each data point. Numbers on the right are representative of the total number of observations per depth layer.

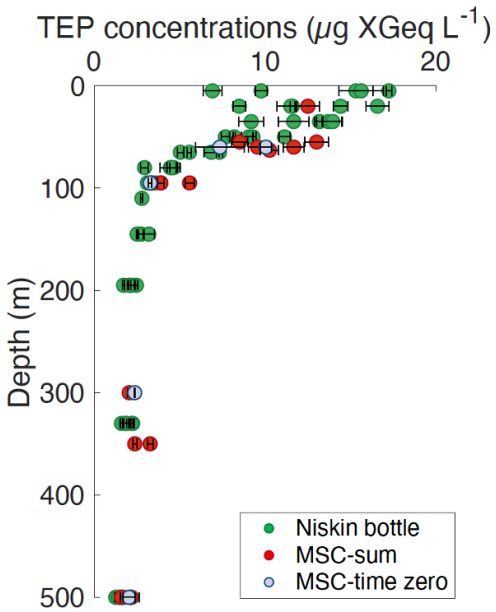

Figure S3. Comparison of transparent exopolymer particles (TEP) concentrations measured on seawater collected with Niskin bottles and the MSCs. Scatter plot displays a comparison of TEP concentrations estimated in the whole water column collected with the Niskin bottles (green), by summing suspended and sinking TEP collected with the MSC (red) and in the MSC T_0 fraction (lilac).

Table S1. Summary of Marine Snow Catcher deployments ordinated through time. Table shows the type of sampling performed for each MSC deployment. Hyphens indicate lack of sampling.

Date in 2018 (UTC)	Depth (m)	Lat (°N)	Long (°E)	BGC measurements	FlowCam	Settling time test (hours)
Aug 16, 04:24	55	50.107	–145.071	POC/N, TEP	X	-
Aug 16, 03:56	95	50.107	–145.071	POC/N, TEP	X	-
Aug 16, 03:03	195	50.107	–145.071	POC/N, TEP	-	-
Aug 17, 23:42	195	50.200	–145.041	POC/N, TC, bSi/lSi	-	-
Aug 18, 00:44	55	50.200	–145.041	POC/N, TC, bSi/lSi	-	-
Aug 18, 00:17	95	50.200	–145.041	TC, bSi/lSi	X	-
Aug 20, 04:38	80	50.320	–145.073	POC/N, bSi	-	4
Aug 20, 04:59	80	50.320	–145.073	POC/N, bSi, TEP	-	2
Aug 20, 05:19	80	50.320	–145.073	POC/N, bSi, TEP	-	1
Aug 20, 23:43	195	50.366	–145.063	POC/N	X	-
Aug 21, 00:48	65	50.366	–145.063	POC/N	X	-
Aug 21, 00:22	95	50.366	–145.063	POC/N	X	-
Aug 24, 01:12	63	50.412	–145.125	POC/N, TEP	X	-
Aug 24, 00:45	95	50.412	–145.125	POC/N, TEP	X	-
Aug 24, 00:08	350	50.412	–145.125	POC/N, TEP	X	-
Aug 25, 23:54	350	50.461	–145.005	POC/N, TC, bSi/lSi	X	-
Aug 26, 00:54	60	50.461	–145.005	POC/N, TC	X	-
Aug 26, 00:32	95	50.461	–145.005	POC/N, TC, bSi/lSi	X	-

Aug 28, 01:22	60	50.476	–144.898	POC/N, TC, TEP	X	-
Aug 28, 01:52	500	50.476	–144.898	POC/N, TC, bSi/lSi, TEP	-	-
Aug 29, 01:07	60	50.489	–144.838	POC/N, TEP	X	-
Aug 29, 00:44	95	50.489	–144.838	POC/N, TEP	X	-
Aug 29, 00:11	300	50.489	–144.838	POC/N, TEP	X	-
Sep 01, 03:58	55	50.584	–144.863	POC/N, TEP	X	-
Sep 01, 06:10	95	50.584	–144.863	POC/N, TEP	X	-
Sep 01, 06:41	350	50.584	–144.863	POC/N, TEP	X	-
Sep 02, 22:58	350	50.577	–144.748	POC/N, TC, bSi/lSi	X	-
Sep03, 00:54	50	50.577	–144.748	POC/N, TC, bSi/lSi	X	-
Sep 03, 00:30	95	50.577	–144.748	POC/N, TC, bSi/lSi	X	-
Sep 05, 00:55	20	50.534	–144.694	POC/N, TC, bSi/lSi, TEP	X	-
Sep 05, 00:14	500	50.534	–144.694	POC/N, TC, bSi/lSi, TEP	X	-
Sep 05, 23:59	95	50.487	–144.717	POC/N	X	-
Sep 06, 00:48	25	50.487	–144.717	POC/N	X	-
Sep 06, 00:24	60	50.487	–144.717	POC/N	X	-
Sep 08, 19:35	60	50.558	–144.677	POC/N, bSi, TEP	-	4
Sep 08, 20:04	60	50.558	–144.677	POC/N, bSi, TEP	-	2
Sep 08, 20:30	60	50.558	–144.677	POC/N, bSi, TEP	-	1

Table S2. FlowCam technical specification and detailed methods explanation. Table shows the protocol implemented to image and count marine particles using the FlowCam. The template we used is a modification of the template offered in Owen et al. (2022).

FlowCam technical specifications	
FlowCam model number	8410
FlowCam unit serial number	10446
Camera resolution	*1920 x 1200 pixels*
Camera	Color
Fluidics	Syringe pump (0.5 mL for 20x, 5.0 mL for 4x)
Software details	VisualSpreadsheet© software version 4.15.1

Sample details	
Preservation methods	Seawater samples preserved with 37% buffered formaldehyde to a final concentration of 1–2%
Pre-filtration details	Subsamples of the *base* and *tray* fractions were pre-filtered before analysis at 20x using a 44 µm mesh filter

FlowCam setup details for analysis with the 20x objective	
Flow cell sizes and types used, and objectives used for each flow cell	50 x 300 µm flow cell (FOV), 20x objective
Calibration factor	0.3380
Image acquisition mode	Auto-image
Flow rate	0.03 mL min^{-1}
Example of full context settings for 20180816_0356_001_NSP	Run: Mode: AutoImage Priming Method: machine prime Flow Rate: 0.030 ml/min Recalibrations: 1 Stop Reason: Sample Volume Processed Sample Volume Aspirated: 1.0000 ml Sample Volume Processed: 0.9990 ml Fluid Volume Imaged: 0.3388 ml Efficiency: 33.9%

Particle Count: 1239

Images:
Total: 38201
Used: 1219
Percentage Used: 3.19%
Particles Per Used Image: 1.02
Particles Per Image: 0.03
Particles Per Image: 0.03
Frame Rate: 19.57 fps
Intensity Mean: 177.09
Intensity Min: 174.78
Intensity Max: 177.72

Date/Time:
Start: 2019-08-22 10:48:26
End: 2019-08-22 11:21:52
Sampling Time: 00:32:31

Environment:
Software: VisualSpreadsheet 4.15.1
Magnification: 20X
Calibration Factor: 0.3380
GumStix Firmware: 23
Calibration Factor: 0.3380
SerialNo: 10446
Number of Processors: 8
Pump: C80 Syringe
Syringe Size: 0.50 ml

Capture Parameters:
Distance To Neighbor = 30
Threshold Dark = 15.0000
Threshold Light = 18.0000
Close Holes = 0
Capture Dark or Light Pixels = 2

FlowCam setup details for analysis with the 4x objective	
Flow cell sizes and types used, and objectives used for each flow cell	300 x 1500 µm flow cell (FOV), 4x objective
Calibration factor	1.8130
Image acquisition mode	Auto-image
Flow rate	0.9 mL min^{-1}

Example of full context settings for 20180817_2205_001_NSP	Run: Mode: AutoImage Priming Method: machine prime Flow Rate: 0.900 ml/min Recalibrations: 0 Stop Reason: Sample Volume Processed Sample Volume Aspirated: 9.9892 ml Sample Volume Processed: 9.9544 ml Fluid Volume Imaged: 6.9242 ml Efficiency: 34.9% Particle Count: 1542 Images: Total: 2648 Used: 1166 Percentage Used: 44.03% Particles Per Used Image: 1.32 Particles Per Image: 0.58 Particles Per Image: 0.58 Frame Rate: 3.99 fps Intensity Mean: 168.49 Intensity Min: 167.68 Intensity Max: 169.85 Date/Time: Start: 2019-09-10 11:04:32 End: 2019-09-10 11:16:10 Sampling Time: 00:11:03 Environment: Software: VisualSpreadsheet 4.15.1 Magnification: 4X Calibration Factor: 1.8130 GumStix Firmware: 23 Calibration Factor: 1.8130 SerialNo: 10446 Number of Processors: 8 Pump: C80 Syringe Syringe Size: 5.00 ml Capture Parameters: Distance To Neighbor = 50 Threshold Dark = 15.0000 Threshold Light = 18.0000 Close Holes = 0 Capture Dark or Light Pixels = 2

Measurement outputs	
Measurement type(s) used	Equivalent spherical diameter (ESD)
Justification for this choice	Measurement type chosen based on particles type: particles were very small, mostly round, and transparent (see example of images below). VisualSpreadsheet© software version 4.15.1. identifies pixels that comprise a particle by distinguishing them from the image background taken automatically at each run. Among other parameters, the software estimates the area-based diameter (hereafter ABD) and the ESD. ABD is the diameter calculated based on a circle with an area equal to the ABD area. The ABD area is determined by the number of dark pixels in the binary imaged particle, excluding inner light pixels. ESD is the mean value of 36 feret measurements. Feret measurements are the perpendicular distance between parallel tangents touching opposite sides of the particle (VisualSpreadsheet 5 Particle Analysis Software manual). ABD would be expected to underestimate the size of particles with internal transparent components, while ESD would be expected to overestimate the size of particles with protrusions or flagella (Owen et al., 2022).

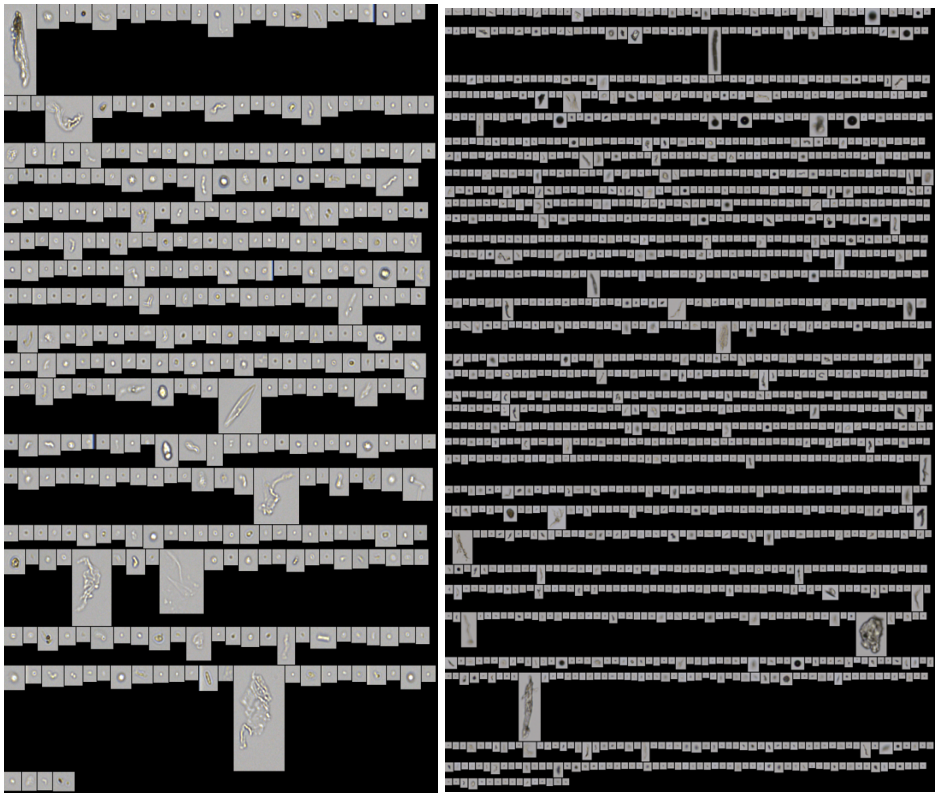

Examples of suspended particles imaged at 200x (left) and 40x (right).

Table S3. Relative standard deviations (σ^2) used as part of the Monte Carlo method to account for uncertainties propagation.

Biogeochemical component	**σ^2 of suspended particles (%)**	**$\sigma^2$of slow-sinking particles (%)**	**$\sigma^2$of fast-sinking particles (%)**
POC	17	6	28
PON	20	14	28
TEP	11	13	19

Table S4. Particle concentrations estimated within 5 size bins based on particle equivalent spherical diameters (ESD) spanning from 4 µm to 128 µm. The table shows suspended and sinking particle concentration (particles mL^{-1}) grouped in size bins according to their equivalent spherical diameter (ESD). The abbreviation "na" indicates unmeasured values. Zeros reflect negative or null concentrations.

Date in 2018 (UTC)	Depth (m)	Suspended particles (ml^{-1})					Sinking particles (mL^{-1})		
		4–8 µm	8–16 µm	16–32 µm	32–64 µm	64–128 µm	4–8 µm	8–16 µm	16–32 µm
Aug 16, 03:56	95	741	413	251	na	na	144	17	5
Aug 16, 04:24	55	3036	1273	359	na	na	125	7	0
Aug17, 23:42	195	720	233	71	16	2	126	41	11
Aug 18, 00:17	95	540	142	27	8	1	1373	150	7
Aug 18, 00:44	55	1032	305	80	9	1	65	16	2
Aug 20, 23:43	195	469	165	50	10	2	254	35	4
Aug 21, 00:22	95	484	109	21	9	0	68	22	4
Aug 21, 00:48	65	723	136	30	8	1	74	26	8
Aug 24, 00:08	350	1025	373	151	na	na	142	43	3
Aug 24, 00:45	95	941	263	62	na	na	16	3	0
Aug 24, 01:12	63	2143	686	90	na	na	768	201	69
Aug 25, 23:54	350	1982	497	92	na	na	297	26	5
Aug 26, 00:32	95	1702	463	144	na	na	226	38	3
Aug 26, 00:54	60	528	201	44	na	na	410	60	18
Aug 28, 01:33	60	1183	298	67	na	na	144	33	12
Aug 28, 01:53	500	1344	331	71	na	na	24	7	3
Aug 29, 00:11	95	1082	238	23	na	na	152	72	33
Aug 29, 00:44	95	629	165	21	na	na	142	26	6

Aug 29, 01:07	60	2391	343	29	na	na	351	114	26
Sep 01, 03:58	55	5115	1615	190	21	3	56	21	6
Sep 01, 06:10	95	900	274	41	9	2	84	26	6
Sep 01, 06:41	350	880	183	52	13	3	142	23	7
Sep 02, 23:58	350	508	200	30	11	3	345	56	12
Sep 03, 00:30	95	521	164	40	9	2	148	47	9
Sep 03, 00:54	50	982	497	97	24	4	35	20	6
Sep 05, 00:14	500	865	316	68	17	3	57	15	3
Sep 05, 00:55	20	714	375	103	10	2	255	58	18
Sep 05, 23:59	95	2745	736	84	18	2	165	27	4
Sep 06, 00:24	60	1327	402	48	6	1	180	61	13
Sep 06, 00:48	25	1441	455	68	14	3	63	38	16

Table S5. Concentrations of suspended and sinking particulate biogeochemical components. Particulate organic carbon and nitrogen (POC and PON), particulate inorganic carbon (PIC), biogenic and lithogenic silica (bSi and lSi) and transparent exopolymer particles (TEP) concentrations associated with suspended (SU) and sinking (S) particles. Values in bold are the outliers discussed in Section 4.5. The abbreviation "na" indicates that values were not collected or were lost during analysis. The propagated uncertainty is denoted as "sd".

Date in 2018 (UTC)	Depth (m)	POC (µg C L^{-1})				PON (µg N L^{-1})				PIC (µg C L^{-1})		bSi (µmol Si L^{-1})		lSi (µmol Si L^{-1})		TEP (µg GXeq L^{-1})			
		SU	SUsd	S	Ssd	SU	SUsd	S	Ssd	SU	S	SU	S	SU	S	SU	SUsd	S	Ssd
Sep 05, 00:55	20	74.2	12.4	3.1	1.5	13.9	2.6	0.6	0.3	0.0	0.0	0.14	0.02	0.1	0.02	12.3	1.4	0.2	0.2
Sep 06, 00:48	25	78.1	13.0	1.5	1.1	14.8	2.7	0.5	0.3	na	na	na	na	na	na	na	na	na	na
Sep 03, 00:54	50	45.9	7.7	4.0	1.2	8.8	1.6	1.0	0.3	1.0	0.9	0.05	na	0.1	0.0	na	na	na	na
Aug 16, 04:24	55	58.7	9.8	**21.3**	4.7	10.7	2.0	**2.0**	0.5	na	na	na	na	na	na	na	1.4	0.7	0.1
Aug 18, 00:44	55	na	na	na	na	na	na	na	na	na	na	0.04	0.02	0.1	0.01	na	na	na	na
Sep 01, 03:58	55	37.8	6.3	5.0	1.2	10.3	1.9	1.2	0.4	na	na	na	na	na	na	8.3	0.9	0.2	0.1
Aug 26, 00:54	60	46.0	7.7	1.9	0.6	4.6	0.8	0.3	0.1	3.0	na	0.06	0.01	0.2	0.01	na	na	na	na
Aug 28, 01:33	60	63.9	10.7	2.4	1.1	5.8	1.1	0.4	0.1	0.0	0.6	0.05	0.01	0.1	0.04	11.3	1.2	0.4	0.2
Aug 29, 01:07	60	71.2	11.9	1.2	1.0	6.4	1.2	0.7	0.3	na	na	na	na	na	na	9.4	1.0	0.2	0.1
Sep 06, 00:24	60	44.4	7.4	2.2	0.8	10.9	2.0	0.5	0.2	na	na	na	na	na	na	na	na	na	na

Aug 24, 01:12	63	48.3	8.1	5.2	1.4	8.9	1.6	0.6	0.2	na	na	na	na	na	na	9.6	1.1	0.6	0.0
Aug 21, 00:48	65	48.0	8.0	0.4	0.5	7.9	1.5	0.1	0.1	na	na	na	na	na	na	na	na	na	na
Aug 16, 03:56	95	35.0	5.8	**35.1**	7.5	4.2	0.8	**4.0**	0.9	na	na	na	na	na	na	4.7	0.5	**0.8**	0.0
Aug 18, 00:17	95	na	na	na	na	na	na	na	na	na	na	0.04	0.02	0.0	0.04	na	na	na	na
Aug 21, 00:22	95	12.9	2.2	0.9	0.2	4.1	0.8	0.1	0.1	na	na	na	na	na	na	na	na	na	na
Aug 24, 00:45	95	23.5	3.9	3.8	0.9	3.8	0.7	0.4	0.1	na	na	na	na	na	na	3.8	0.4	0.1	0.1
Aug 26, 00:32	95	18.6	3.1	2.5	0.7	0.2	0.0	0.3	0.1	2.5	0.0	0.05	0.00	na	0.00	na	na	na	na
Aug 29, 00:44	95	19.5	3.3	2.4	0.5	1.7	0.3	0.7	0.2	na	na	na	na	na	na	3.8	0.4	0.1	0.1
Sep 01, 06:10	95	18.7	3.1	1.3	0.4	5.2	1.0	0.4	0.1	na	na	na	na	na	na	3.0	0.3	0.3	0.1
Sep 03, 00:30	95	14.6	2.4	2.3	0.6	4.3	0.8	0.5	0.2	6.7	0.0	0.05	0.01	0.3	0.02	na	na	na	na
Sep 05, 23:59	95	20.7	3.5	1.1	0.4	6.6	1.2	0.3	0.1	na	na	na	na	na	na	na	na	na	na
Aug 20, 23:43	195	**43.9**	7.3	2.0	0.5	**5.4**	1.0	0.5	0.1	na	na	na	na	na	na	na	na	na	na
Aug 16, 03:03	195	**32.2**	5.4	na	na	3.8	0.7	na	na	na	na	na	na	na	na	2.8	0.3	na	na
Aug 17, 23:42	195	na	na	na	na	na	na	na	na	na	na	0.08	0.02	0.1	0.05	na	na	na	na

Aug 29, 00:11	300	9.6	1.6	2.2	0.6	0.0	0.0	0.0	0.0	na	na	na	na	na	na	2.0	0.2	0.1	0.0
Aug 24, 00:08	350	13.1	2.2	2.0	0.4	0.8	0.1	0.1	0.0	na	na	na	na	na	na	2.3	0.2	0.1	0.0
Aug 25, 23:54	350	4.3	0.7	1.7	0.3	0.0	0.1	0.1	0.0	3.0	**21.5**	0.04	0.00	0.1	0.02	na	na	na	na
Sep 01, 06:41	350	**32.4**	5.4	**5.5**	0.9	**8.5**	1.6	**1.2**	0.3	na	na	na	na	na	na	3.1	0.3	0.1	0.0
Sep 02, 23:58	350	5.6	0.9	1.2	0.2	0.7	0.1	0.3	0.1	2.9	0.0	0.03	0.00	0.2	0.00	na	na	na	na
Aug 28, 01:53	500	6.0	1.0	2.0	0.3	0.0	0.1	0.2	0.0	4.9	0.4	**0.18**	0.01	na	0.01	2.0	0.2	0.1	0.0
Sep 05, 00:14	500	5.6	0.9	3.4	0.6	0.9	0.2	0.7	0.2	8.3	0.0	0.04	0.01	0.1	0.00	1.5	0.2	0.1	0.0

Table S6. Concentrations of biogeochemical components of sinking particles after 1, 2 and 4 hours of settling. Table illustrates the results of the settling time test. POC, PON, bSi and TEP concentrations (average of replicate filters) and associated uncertainties (standard deviations) measured in sinking particles after 1, 2 and 4 hours of settling. The three marine snow catchers were deployed at two stations at 80 m and 60 m, respectively.

Date in 2018 (UTC)	**Depth (m)**	**Settling time (hours)**	**Sinking POC (µg L^{-1})**	**Sinking PON (µg L^{-1})**	**Sinking bSi (nmol L^{-1})**	**Sinking TEP (µg XGeq L^{-1})**
Aug 20	80	1	5.4 ± 1.1	0.4 ± 0.1	8 ± 1	0.4 ± 0.1
Aug 20	80	2	6.1 ± 0.5	0.5 ± 0.2	8 ± 0	0.2 ± 0.0
Aug 20	80	4	5.6 ± 0.7	0.7 ± 0.0	8 ± 0	0.3 ± 0.1
Sep 08	60	1	3.9 ± 0.2	0.5 ± 0.1	12 ± 3	0.4 ± 0.2
Sep 08	60	2	3.4 ± 0.1	0.4 ± 0.1	10 ± 2	0.1 ± 0.1
Sep 08	60	4	3.6 ± 0.2	0.6 ± 0.1	15 ± 1	0.2 ± 0.1

II. Storms affect sinking particle fluxes after the North Atlantic spring bloom

Elisa Romanelli, Sarah Lou Carolin Giering, Margaret Estapa, David A. Siegel, Uta Passow

Abstract

Sinking of large particles (i.e., marine snow) is a key pathway for efficient carbon export to the ocean interior during the decline of spring diatom blooms. Recent work has suggested that particles smaller than marine snow can also substantially contribute to carbon export. However, a detailed characterization of small and large particles at the end of blooms is missing. Here, we collected suspended, and small and large sinking particles using Marine Snow Catchers and assessed their biogeochemical composition at the demise of the North Atlantic spring bloom in May 2021. When we arrived, 70% of the diatoms had already been exported from the upper ocean. During the following three weeks, when four intense storms (≥ 9 on the Beaufort scale) created high turbulence and deepened the mixed layer, we observed two sedimentation events. First, during the storms, sedimentation was dominated by small (diameter < 0.1 mm), slow-sinking (∼18 md^{-1}), silica-rich particles that carried a moderate POC flux (< 6 mmol C m^{-2} d^{-1}) to 500 m depth. The second event was dominated by large (diameter > 0.1 mm) fast-sinking (> 90 md^{-1}), carbon-rich marine snow. Once the storms ceased, the volume of marine snow increased exponentially and POC fluxes at 100 m depth were more than fourfold greater (28±15 mmol C m^{-2} d^{-1}) than those during the previous event. This marine snow exported a mixed post-bloom plankton community. Our

data suggest that the storms delayed the formation and sinking of marine snow allowing the sedimentation of non-diatom species.

Introduction

Spring phytoplankton blooms account for a significant fraction of the annual oceanic primary production and substantially contribute to carbon sequestration by the ocean (Henson et al., 2019; Siegel et al. 2023). The termination of a diatom bloom is often viewed as one single event of diatom mass aggregation and subsequent sedimentation of carbon-rich, fast-sinking marine snow triggered when nutrient limitation occurs, causing bloom senescence (Alldredge and Gotschalk, 1989; Kiørboe et al., 1996). The result is the efficient export of particulate organic carbon (POC) to the ocean interior (Honjo, 1982; Smetacek, 1985). The transition between bloom growth and export via marine snow is difficult to predict and observe in the open ocean due to its ephemeral and spatially heterogeneous nature. We therefore lack an understanding of the spatiotemporal dynamics of sinking particles during the declining phase of a bloom.

At the end of spring phytoplankton blooms, fast-sinking marine snow (sinking velocity > 50 m d^{-1}) is considered the main vector for efficient carbon transport (Alldredge and Silver 1988; Alldredge and Gotschalk, 1989; Riebesell, 1991b). Marine snow produced after diatom blooms form via coagulation of particles in the presence of high particle concentration (e.g., phytoplankton bloom) and increased levels of stickiness that enable attachment of particles that have collided (Jackson, 1990). Marine snow is composed of microbial cells and organic and inorganic particulate material embedded in a matrix of transparent exopolymer particles (TEP). Transparent exopolymer particles are gel-like particles largely composed of polysaccharides exuded as extracellular, surface-active

exopolymers (Passow, 2002), especially under nutrient-limited conditions (Obernosterer and Herndl, 1995). Due to their sticky nature, the presence of TEP favor the formation of marine snow by increasing the probability that the collision of particles will result in aggregation (Passow et al., 1994; Jackson, 1995). However, TEP are inherently positively buoyant (Engel and Schartau, 1999; Azetsu-Scott and Passow, 2004), and their role in regulating the efficiency of POC export is uncertain and dependent on the oceanic ecosystem (Romanelli et al., 2023). Another important factor controlling the formation of marine snow is the intensity of turbulent shear (Jackson, 1990; Stemmann et al., 2004) In the open ocean, turbulent kinetic energy dissipation rates in the mixed layer vary between 10^{-10} W kg^{-1} to 10^{-1} W kg^{-1} (D'Asaro, 2014), with the highest rates occurring under intense storm conditions. Turbulence needs to be large enough so that particle-particle contact rates will lead to coagulation. However, when turbulent dissipation energy is intense ($\varepsilon > 10^{-6}$ W kg^{-1}), disaggregation of marine snow may be more important than aggregation in dictating marine snow size (Dyer and Manning, 1999; Ruiz and Izquierdo, 1996; Takeuchi et al., 2019). The impact of storm severity on sedimentation of marine snow is yet to be observed in situ.

Here we present detailed observations of the sedimentation dynamics after the main spring diatom bloom sedimentation episode. This period immediately after the main sedimentation event was characterized by a series of intense storms that impacted sedimentation dynamics. To understand these different post-bloom sedimentation events we characterized suspended, small sinking particles and fast-sinking marine snow collected using Marine Snow Catchers (MSC; Lampitt et al., 1993) during the NASA-led Export

Processes in the Ocean from RemoTe Sensing (EXPORTS) North Atlantic field campaign, which provided a broad suite of contextualizing observations (Johnson et al., 2023).

Materials and Methods

Study site

Observations of suspended and sinking particle characteristics were obtained in spring 2021 (May 1–June 1, 2021) on board the RRS James Cook, which targeted biogeochemical and ecological processes within an anticyclonic particle retentive eddy in a semi-Lagrangian fashion (Johnson et al., 2023). The eddy was located ~170 km east of the site of the Porcupine Abyssal Plain Sustained Observatory (PAP-SO) (Erickson et al. 2023). During the cruise four storms substantially deepened the mixed layer (ML, 0.05 kg^{-3}) by 25–40 m (Figure 1), advecting and exchanging between 23% to 73% of the ML water. (Johnson et al., 2023). For this reason, the eddy can be considered retentive only below depths of ~100 m (eddy core waters) and within 15 km from its center (Johnson et al., 2023). The deployments of the MSCs were performed at 7 ± 4 km from the eddy center except on May 12 where samples were collected at 17 km. To better investigate temporal trends, we grouped our observations in five time periods (P) constrained by the four storms (P1: May 4–7; P2: May 12–14; P3: May 16–19; P4: May 22; P5: May 25–29; Figure 1). The first storm (May 7–10) exchanged 73% of the ML water, and we hence refrain from drawing conclusions regarding temporal trends between P1 and P2, but P1 observations are included in the results and figures. The estimated exchange above the ML caused by the three subsequent storms was < 47% each (Johnson et al., 2023), and we interpret P2 to P5 as a time series, especially as our data was collected from below the ML.

Collection of suspended and sinking particles

Suspended and sinking particles were collected with four 100-liter Marine Snow Catchers (MSC, OSIL), between 40 and 500 m depth at 16 stations in the morning (03:00–10:00 UTC, local time) except for two casts (on May 13 and 25) collected at 16:30 UTC. At each station, one MSC was deployed 10 m below the ML, one 110 m below the ML, one at 300 or 500 m and one at a variable depth matching the deployment depths of the Neutrally Buoyant Sediment Traps (NBST, Estapa et al., 2023).

The MSC methodology is described in detail in Romanelli et al. (2023). Briefly, the MSC is a water sampler with a top and base section (82.2 L and 7.6 L, respectively) allowing the collection of particles according to their sinking velocity (Riley et al., 2012; Giering et al., 2016). To separately collect slow- and fast-sinking particles, a circular plastic tray (polypropylene, diameter: 18.5 cm; height: 4 cm; volume: ~1L) was placed at the bottom of the MSC's base. We defined three particle fractions according to their sampling location within the MSC immediately after 2 hours of settling: top (t), base (b) and tray (tr). The top fraction was collected from the central tap and contained suspended particles. After draining and removing the top section, water overlying the tray in the base section was collected constituting the base particle fraction. The particle fraction in the tray was designated as the tray fraction. At 9 stations, fast-sinking marine snow (defined here as ESD > 0.1 mm, examples in Figure S1) was removed from the tray, visually sized using the aid of a ruler (± 10 %) in size bins of 0.5–1, 1–2, 2–4, 4–8 mm (ESD) and preserved in 4% formaldehyde to perform microscopy later (Table 1). On May 27, fast-sinking marine snow was removed from the tray to measure its POC mass (Table 1) At 3 stations the entire particulate pool in the tray was processed as the tray fraction (i.e., marine snow was not

removed) to enable estimates of the average sinking velocity of fast-sinking particles using the method detailed in section 2.6 (Table 1).

Before sampling, top, base and tray fractions were homogenized through shaking and subsampled using a graduated cylinder. Finally, particulate organic carbon and nitrogen (POC and PON), total particulate carbon (TC) and biogenic silica (bSi) were measured (Table 1). In addition, the concentrations of POC and Transparent Exopolymer Particles (TEP) were assessed on samples collected with Niskin bottles mounted on a CTD-rosette at 7 stations located in the eddy core and within the mixed layer (21±5 m). Analytical methods are detailed below.

Biochemical analysis

Concentrations of particulate organic carbon and nitrogen (POC and PON) were determined by filtering subsamples onto two pre-combusted (450 °C, 30 minutes) replicate GF/F filters (25 mm, Whatmann, UK). We filtered 1 L of the samples collected with the Niskin bottles, 1L of the MSC top fractions, 0.6–1 L of the MSC base fraction and 0.2 L of the MSC tray fraction. The filters were dried at 40°C, stored at room temperature and analyzed using a CEC 44OHA elemental analyzer (Control Equipment, US) after treatment with 150µl of 10% HCl (v/v) to remove particulate inorganic carbon (PIC). Before calculating the concentration of POC and PON, their measured mass was blank corrected to account for contamination using the cruise-wide EXPORTS' average of 26 blanks (7.905 µg for POC; 1.782 µg for PON) obtained using a multiple volume regression approach (Moran et al., 1999) of water collected with Niskin bottles from the CTD-rosette system within the ML (campaign-wide correction, method similar to Graff et al., 2023). We found that 29 of the 423 PON values were below the detection limit. Those values were removed and only

one of the two replicate values used. Negative values were within the relative standard deviation (RSD) of replicate measurements and therefore set to 0 μg N L^{-1}. The RSD of replicate measurements associated with each fraction ranged between 9 and 12% for POC and between 24 and 32% for PON (Table S1). These values substituted for the uncertainty of the measurements that lacked replicates (2 POC values and 3 PON values).

Total particulate carbon (TC) was measured like POC but without prior acidification. Only one filter per fraction was collected due to sample volume constraints. Filtered volumes were the same as for POC. After subtraction of POC from TC, 39 out of 168 PIC values were negative (23%). These values were substituted with a 0 μg PIC L^{-1}.

Concentrations of biogenic and lithogenic silica (bSi and lSi) were determined by filtering subsamples onto 0.6-μm pore size polycarbonate membrane filters (47 mm PC, Isopore, Millipore), which were frozen at sea in cryovials at -20°C, transported to shore frozen, dried at 60°C, and then stored at room temperature until analysis. Concentrations of biogenic and lithogenic silica were assessed spectrophotometrically via the molybdosilicic acid spectrophotographic method (Strickland and Parsons, 1968, Tréguer et al., 1992).

Concentrations of TEP were determined colorimetrically on triplicate samples of 400 mL each. Subsamples were filtered onto 0.4-μm pore size polycarbonate filters (25 mm, Whatmann, UK), stained with Alcian blue, and stored frozen at -20°C until analysis. The preparation of filter blanks and the Alcian blue calibration curve were performed as in Romanelli et al., (2023) and the absorption at 787 nm was measured spectrophotometrically (Thermo Scientific GENESYS 10S UV- VIS; Passow and Alldredge, 1995). The Alcian blue calibration f-factor was 34. Our results are expressed as standardized Gum Xanthan equivalents (XGeq; Bittar et al., 2018). For significant values of TEP to be determined the

absorbance value of a sample at 787 nm must be at least twice the absorbance value of the blank at 787 nm (Passow and Alldredge, 1995). Ratios of TEP-C-to-POC were based on estimates of the carbon concentration of TEP using a conversion factor of 0.75 μg TEP-C per 1 μg XGeq TEP (Engel and Passow, 2001).

Calculations of particle concentrations

The concentrations of suspended and sinking particles were calculated from the measured concentrations of top, base and tray particle fractions by subtracting the top fraction from the base fraction and the base fraction from the tray fraction. The differences were scaled for the volume ratios as follows:

Suspended particles = top concentration (2)

Slow-sinking particles = (base – top concentrations) × V_{base} / V_{MSC} (3)

Fast-sinking particles = (tray – base concentrations) × V_{tray} / (A_{tray} × h_{MSC}) (4)

The volume of the base fraction (V_{base}) associated with each deployment was calculated as:

$$V_{base} = V_{bottom} - (V_{tray} / 0.466) \quad (5)$$

where V_{MSC} = 89.8 L, V_{bottom} = 7.6 L, Vtray is the volume of seawater we collected in the tray at each deployment (between 0.7 and 1.2 L) and 0.466 is a scaling factor obtained by accounting for the fact that the area of the tray covers only 46.6% of the area of the bottom of the MSC. V_base ranged between 5.1 and 6.1 L.

At 9 stations, fast-sinking marine snow (ESD > 0.1 mm) was removed from the tray fraction before biochemical analysis. The remaining particles in the tray were smaller than 0.1 mm (ESD). This separation allowed us to assess the concentration of small fast-sinking particles (ESD < 0.1 mm) separately from larger fast-sinking marine snow (ESD > 0.1 mm).

During sampling, we did not observe any marine snow in the base fraction, therefore we can assume that on average the slow-sinking particle population was smaller than 0.1 mm (ESD). Hence, for data interpretation, we summed the concentrations of slow-sinking particles and the concentrations of small, fast-sinking particles into a single particle fraction termed "small sinking particles" (Table 2).

The concentration of fast-sinking marine snow present in the water column was calculated by dividing the number of marine snow particles present in each tray by the associated V_{tray} and multiplied by the volume ratio (V_{tray} / (A_{tray} × h_{MSC}). The volumetric concentration (mm3 L-1) of fast-sinking marine snow was calculated assuming the volume of a sphere and an average diameter of 0.5, 1.5, 3 and 6 mm (midpoint of the 4 size bins: 0.1–1, 1–2, 2–4, 4–8 mm).

In our result section we describe the spatiotemporal variability of the following three particle fractions: suspended particles, small sinking particles, and fast-sinking marine snow (Table 2).

POC concentrations associated with fast-sinking marine snow

We estimated the POC and PON mass (µg) associated with fast-sinking marine snow collected from MSC trays on May 27 at 60 m (below the MLD, 30 m). We placed 10–24 marine snow (approx. 1 mm, ± 10%) on GF/F filters (n = 8) and measured the POC and PON mass as in section 2.3. The POC and PON mass (µg) of a single fast-sinking marine snow was calculated by dividing the blank corrected POC and PON mass by the number of marine snow per filter. The dissolved organic carbon contained in the marine snow porewater (Alldredge, 2000) was likely lost during filtration. Thus, the POC mass is surely an underestimation of the total organic carbon transported by marine snow. The POC and

PON mass (μg) associated with 2.5 mL of tray water was subtracted from the measured mass to account for contamination with smaller particles during pipetting. Values of PON below the detection limit of the analytical instrument were 5 out of 8. The POC mass measured on 1 mm aggregates was on average 0.7 ± 0.1 μg agg-1 (Table S2). This value is consistent with the one obtained using the fractal relationship of Alldredge (1998): POC (μg C) = 0.99 V0.52 (V is volume in mm3) for aggregate with an ESD of 1 mm. We hence used this fractal relationship to calculate the amount of POC in the collected fast-sinking marine snow with an average diameter of 0.5, 1.5, 3, and 6-mm and used a ± 25% uncertainty, which account for the standard deviation of the replicated measurements of the POC mass of marine snow (15%) and the error associated with the marine snow sizing (10%).

Concentrations of POC associated with fast-sinking marine snow were obtained by multiplying the calculated POC mass (μg C) by the concentration of fast-sinking marine snow per each size bin.

To validate our method, we compared the POC concentrations directly measured in the particle fractions B and C (B+C) to the POC concentrations calculated by summing the concentrations of POC in E and F so that B+C = E+F (see Table 2 for nomenclature). The percent difference between the POC concentrations in "B+C" and "E+F" measured in adjacent stations was on average 15% (n = 9), which is less than the standard deviation of the POC concentrations. We are therefore confident that our method is appropriate.

Lastly, the phytoplankton community composition of fast-sinking marine snow was qualitatively evaluated on the 4% formaldehyde fixed samples collected on May 12, 17, 26 and 29 at 50–60 m depth using an Echo Revolve Microscope (Echo Laboratories, USA) with a 10x objective.

Particle sinking velocity and POC fluxes

Particle fluxes were calculated by multiplying the concentration of sinking particles by an estimate of their average sinking velocity (Giering et al., 2016). Errors associated with the POC flux were obtained by propagating the standard deviation of the measurements through each calculation. The sinking velocity of slow-sinking particles collected with the MSCs is on average 18 m d^{-1} (Giering et al., 2016), and the sinking velocity of fast-sinking particles is > 18 m d^{-1}. This method does not allow to constrain the sinking velocity of fast-sinking particles further. We therefore used a novel approach that involves the co-deployment of MSCs and drifting sediment traps to estimate the sinking velocity of fast-sinking particles (small, fast-sinking particles + fast-sinking marine snow) assuming that sediment traps collect both slow-sinking and fast-sinking particles. There is evidence that traps may partially underestimate small particles due to hydrodynamics (Buesseler et al., 2007), therefore our sinking velocity and POC fluxes should be considered a lower bound. Two types of drifting sediment traps (a surface-tethered, drifting mooring and neutrally buoyant sediment traps) were deployed three times during the cruise as described by Estapa et al. (2023). Methods similar to those described by Estapa et al. (2021) were used to measure bulk POC fluxes. Three times (May 12, 17 and 25), we deployed the MSCs at the same depths as the drifting sediment traps (73 m and 174 m, 75 m and 175 m, and 95 m, 145 m, 195 m, and 500 m, respectively). To calculate the average sinking velocity of fast-sinking particles, we first calculated the POC flux due to fast-sinking particles measured by traps by subtracting the MSC POC flux due to slow-sinking particles from the POC fluxes measured with traps. Then we divided those fast-sinking POC fluxes by the POC concentrations measured in the MSC fast-sinking particle fraction. The calculated sinking velocities were

used here to calculate POC fluxes from the MSCs. The error associated with each sinking velocity and POC flux was calculated by propagating the standard deviation of the measurements through each calculation.

Results

Turbulent kinetic energy dissipation rates in the mixed layer

The four storms created intense turbulence in the ML (Figure 1). The five sampling periods (P1 to P5) were characterized by ε levels in the mixed layer less than 10^{-6} W $kg^{-1}$and were separated by intense storm events during which near-surface ε values were larger than 10^{-4} W kg^{-1} (Figure 1; Siegel et al., in prep). Estimates of turbulent kinetic energy dissipation rates (ε, W kg^{-1}) were derived from established scaling relationships (Lombardo and Gregg, 1989; D'Asaro, 2014) using air-sea momentum and buoyancy flux determinations calculated from bulk formulae (Johnson et al. 2023).

Concentrations of POC and TEP in the mixed layer

The concentration of POC in water collected at approximately 20 m depth in the mixed layer decreased from 17 ± 2 µmol C L^{-1} to 12 ± 1 µmol C L^{-1} (n = 6) between P2 and the end of P5 and showed the steepest decline between P3 and the beginning of P5. Specifically, POC concentrations in the ML remained somewhat constant between P2 and P3 and decreased by 1.4-fold from P3 to P5 (Figure 2a). This change in POC over time mirrored the decline in mixed layer Chlorophyll a, POC and bSi concentration observed during the cruise (Johnson et al., 2023). The corresponding concentrations of TEP (Figure 2b) increased from 35 ± 1 µg XGeq L^{-1} in P2 (n = 1, May 11) to 51 ± 6 µg XGeq L^{-1} in P3 (n = 1, May 17), remained somewhat constant between P3 and P4 and decreased to 30 ± 1 µg XGeq L^{-1} (n =

1) by the end of P5 (May 29). Concurrently, the relative contribution of TEP-C to POC (TEP-C-to-POC ratios) increased from 0.13±0.01 in P2 (n = 1, May 11) to 0.25 ± 0.02 at the beginning of P5 (n = 1, May 24) (Figure 2c). The steepest decline in TEP and TEP-C-to-POC ratios occurred during P5.

Characteristics of suspended particles below the mixed layer

The POC concentrations of suspended particles collected at 60–75 m were the highest after the first storm in P2 (May 13, 10 ± 0.7 μmol C L^{-1}, n = 1) and after the second storm in P3 (May 17, 9.3 ± 0.02 μmol C L^{-1}, n = 1) (Figure 3a). Concentrations of POC of suspended particles at 50–75 m depth decreased significantly over time from P3 to P5 between May 17 and May 29 (R^2 = 0.61, $p < 0.05$, n = 8) and remained somewhat constant at 90–140 m, 330 m, and 500 m depth (eddy core waters) (R^2 = 0.04–0.30, p = 0.21–0.82, n = 4–10) (Figure 3a). The PON and bSi concentrations of suspended particles broadly mirrored the spatiotemporal trend of POC concentrations (FigureS2a,b).

The molar bSi-to-POC ratio of suspended particles was the highest in P3 and decreased significantly over time from P3 to P5 at 50–75 m, 90–140 m and 330 m (R^2 = 0.56–0.99, $p < 0.05$, n = 3–8, Figure 3b). This observation indicates a decrease in the relative contribution of bSi to POC suggesting removal of bSi from the suspended particle pool between P3 and P5. No significant temporal trend in the molar bSi-to-POC ratio of suspended particles was observed at 500 m depth (R^2 = 0.36, p = 0.28, n = 5).

Characteristics of small sinking particles below the mixed layer

The concentration of POC in small sinking particles at 60 m peaked during P3 (May 17) m depth (0.95±0.05 μmol C L^{-1}, n = 1) and halved by the end of P5 (May 29, 0.47±0.06

μmol C L^{-1}, 60 m) (Figure 3c); the decrease at 50–65 m from P3 to P5 was significant (R^2 = 0.94, $p < 0.007$ n = 5). In the eddy core waters, POC concentrations in small sinking particles did not show a significant change over time (R^2 = 0–0.29, p = 0.21–0.82 n = 4–10). The concentration of PON in small sinking particles mirrored the evolution of POC (Figure S2c).

The concentrations of bSi in small sinking particles at 60 m were the highest during P3 (May 17) and at the beginning of P5 (May 26). Between 90 and 330 m depth (eddy core waters), bSi concentrations increased mostly from P2 to P3, whereas at 500 m, a significant increase was observed from P4 to P5 (R^2 = 0.74, p = 0.05, n = 5) (Figure S2d).

The molar ratios of bSi-to-POC of small sinking particles doubled from P3 to the beginning of P5 (May 26) at 60 m depth and halved within P5 from May 26 to May 29. The ratios increased significantly from P2 to P5 at 90–140 m depth (eddy core waters) (R^2 = 0.70, $p < 0.003$, n = 10) and at 500 m depth (eddy core waters) (R^2 = 0.5, p = 0.05 n = 5) (Figure 3d).

Molar PIC-to-POC ratios in small sinking particles did not show any significant temporal evolution throughout the cruise (R^2 = 0–0.46, p = 0.30–0.77, n = 4–8) (Figure S2e). Similarly, molar POC-to-PON ratios did not show any spatiotemporal trend over time or depth. However, molar lSi-to-POC ratios of small sinking particles (n = 3) showed a sharp decrease over time due to the complete disappearance of lSi in small sinking particles observed at the end of P5 (May 28) (Figure S2f). This observation mirrored the decrease in molar bSi-to-POC ratios observed in suspended particles, which indicated removal of silica-rich particles from the suspended particulate pool at the end of the study period.

Characteristics of fast-sinking marine snow below the mixed layer

The highest concentration and size of fast-sinking marine snow was observed at 60 m at the end of P5 (May 29). Specifically, the volumetric concentration ($mm^3\ L^{-1}$) of fast-sinking marine snow increased exponentially throughout the cruise (from P2 to P5) between 40 m and 500 m depth with P5 characterized by the highest volume concentrations of the cruise (Adjusted R2= 0.65–0.95, RMSE: 1.13–1.78, n = 4–8) (Figure 3f). At 100 and 350 m, the peak volumetric concentration ($2.3 \pm 0.1\ mm^3\ L^{-1}$, n = 3) occurred on May 26, in early P5. By May 28 the volume at 90 m increased to $3.9\ mm^3\ L^{-1}$, decreased by 3-fold at 150 m and approx. $0\ mm^3\ L^{-1}$ at 330 m.

The POC concentrations of fast-sinking marine snow increased significantly over time from P2 to P5 above 200 m (R2 = 0.66–0.81, $p < 0.05$ n = 6) and were the largest in P5 accounting for 0.52 and 0.02 μmol C L^{-1} at 60 m and 500 m, respectively at the end of P5 (May 29) (Figure 3e).

The plankton community composition associated with fast-sinking marine snow collected at 50–60 m transitioned during the cruise. Overall, we observed an increased contribution of heterotrophs, as well as healthy diatoms from P2 to the end of P5. On May 12 (P2), fast-sinking marine snow contained detrital diatoms mainly Chaetoceros spp. and Navicula –type pennates, but also Rhizosolenia spp., silicoflagellates (Haptophytes), and Tintinnids (heterotrophs). By May 17 (P3), dinoflagellates had become relevant, including autotrophs (Ceratium spp.), and hetero- or mixotrophic taxa, whereas Silicoflagellates and Chaetoceros spp. appeared less important compared to May 12. On May 26 (beginning of P5), marine snow composition was similar to the one observed on May 17 with the addition of a few radiolarians. By the last day of P5 (May 29), marine snow did not contain

silicoflagellates and was possibly largely composed by heterotrophs (dinoflagellates, tintinnids); an increased in intact diatoms was also observed (see supplemental material).

Sinking velocity of fast-sinking particles

The sinking velocity of fast-sinking particles (small, fast-sinking particles plus fast-sinking marine snow) as calculated by a comparison between sediment traps and MSC data are given in Figure 4. The sinking velocity of fast-sinking particles above 200 m depth increased over time from an average (± variability among estimates) of 16 ± 4 m d^{-1} (n = 6) during P2 and P3 to an average of 97 ± 30 m d^{-1} (n = 4) during P5 (Figure 4). This increase was concurrent with the increase in the volumetric concentration of fast-sinking marine snow observed during P5 (Figure 2f). From P2–P3 to P5, the contribution of small silica-rich particles to the total POC content of sinking particles decreased from being on average 99 % to 54 %. This indicates that sinking velocities estimated in P2 and P3 were almost fully representative of the sinking velocity of small silica-rich particles, whereas the sinking velocity in P5 increased due to the contribution of fast-sinking marine snow. Notably, in P2 and P3, fast-sinking particles had approximately the same average sinking velocity of slow-sinking particles. At the beginning of P5 at 500 m depth, the sinking velocity of fast-sinking particles was 42 ± 5 m d^{-1} (n = 1) (Figure 4). The sinking velocity of fast-sinking particles was assessed only on three days and at a few depths. For this reason, we averaged the sinking velocities to be able to calculate the POC fluxes of particles collected in between such values (Table 3).

POC fluxes

The POC flux due to the total sinking particle pool (slow-sinking particles plus fast-sinking particles) peaked at the end of P5 (May 29). Overall, values increased significantly over time from P2 to P5 at 60–75 m, 90–125 m and 160–185 m depth (R^2 = 0.66–0.97, $p < 0.05$, n = 6–12) and increased, although not significantly, at 500 m depth (R^2 = 0.37, p = 0.20, n = 6) (Figure 5a). Specifically, at 90–125 m fluxes were 6±2 mmol C m^{-2} d^{-1} (n = 6) during P2–4 and a factor of 4.5 higher (28±15 mmol C m^{-2} d^{-1}) during P5 (n = 4). At 500 m fluxes almost doubled from P2–4 to P5 (2±1 mmol C m^{-2} d^{-1}, n = 4 versus 6±1 mmol C m^{-2} d^{-1}, n = 2).

The contribution of fast-sinking particles to the total POC flux (slow-sinking plus fast-sinking particles) was the highest in P5 above 200 m depth (95%, 50–70 m depth). The contribution of fast-sinking particles to the total POC flux increased significantly from P2 to P5 between May 13 and May 29 (R2 =0.66–0.88, $p < 0.02$, n = 8–9) at 50–75 m and 90–125 m depth (Figure 5b) and at 160–185 m depth between May 16 and May 29 (R^2 =0.67, $p < 0.05$, n = 6). No significant temporal trend was observed at 500 m (R^2 = 0.20, p = 0.37, n = 6).

Discussion

Our sampling regime started at the end of a bloom of diatoms with 72% of the bSi produced during the bloom already exported when the cruise started (Brzezinski et al., in prep). The extremely low silicate (SiO_4 ~ 0.2 µmol L^{-1}) and high nitrate concentrations observed in the mixed layer during the cruise suggest that a likely trigger of the diatom bloom decline was silicate limitation (Johnson et al., 2023; Brzezinski et al., in prep). Consistent with this interpretation, the phytoplankton community in the mixed layer was

dominated by diatoms at the beginning of the study (P1) but their absolute and relative abundances declined (Meyer et al., 2023; Erin Jones, personal communication). An appreciable shift in the phytoplankton community from diatoms to haptophytes and chlorophytes was observed in the mixed layer during the cruise (Meyer et al., 2023; Erin Jones personal communication), indicating that the phytoplankton bloom was transitioning because of silica limitation (Sieracki et al., 1993). Nevertheless, diatom contribution to POC export during the cruise has been estimated to be at 40–70% (Brzezinski et al., in prep).

Under these conditions, we observed two sedimentation events that followed the main sedimentation of diatoms (Figure 6). The first sedimentation event was dominated by small, silica-rich particles that sank in the upper mesopelagic regardless of the presence of three intense storms. The second sedimentation event consisted of fast-sinking marine snow, which increased when the storms ceased. In the following sections, we characterize each sedimentation event and discuss their implication for efficient carbon transport in the upper mesopelagic.

Moderate sedimentation event during the storms

The molar bSi-to-POC ratios measured in small sinking particles indicate increased sinking of small silica-rich particles during the storm periods (P2–P4) reaching 500 m depth by the end of P5. Our findings are consistent with an increased flux of sinking diatom cells between P2 and P4 detected in polyacrylamide gel sediment traps (Bodel, 2023). Diatoms were both intact and empty/fragmented and their community composition did not change over time (Bodel, 2023). Our observations also indicate accumulation of TEP in the mixed layer from P2 to P4. Enhanced TEP production has been linked to stressed and senescent phytoplankton and therefore it is expected in the termination phase of diatom blooms

(Passow and Alldredge, 1995). Together these observations suggest that during the cruise physiologically stressed diatoms were releasing TEP and sinking in the upper mesopelagic.

We expected the combination of senescent diatoms, increased TEP concentrations and elevated particle encounter rates due to high levels of mixed layer turbulence (Figure 1, see section 4.2 to follow) to drive the formation of fast-sinking marine snow. Instead, while TEP was accumulating in the ML, sinking fluxes were mostly dominated by small silica-rich particles (i.e., diatoms and their detritus).

Overall, our POC flux estimates suggest that the export of small silica-rich particles created a moderate POC flux to 500 m depth (< 6 mmol C m^{-2} d^{-1}). Small silica-rich particles contributed on average 97% of the POC concentration measured in the sinking particle population at 500 m depth. Hence, sinking diatoms were the main contributors of POC flux at 500 m depth during the cruise. However, the export ratio (here calculated as the fraction of net primary production (NPP, Meyer et al., 2023) that is exported as vertical carbon flux from 100 m depth) was 0.1± 0.04 (n = 5) in P2–P4, which is considered modest, and is typical of low productivity systems (Buesseler et al., 2020). These small silica-rich particles were sinking slowly (approximately 18 m d^{-1}) and therefore their POC content was likely mostly recycled through the food web in the shallow mesopelagic, rather than efficiently exported to below 500 m. This statement is also supported by the lack of increase in the POC concentration of small sinking particles below 200 m depth (section 3.2).

Different mechanisms may explain the observed sinking of small, silica-rich particles (i.e., diatoms and their detritus) to depth and concurrent increased of TEP in the ML. Some small silica-rich particles may have been already below the ML as a result of the main diatom export event that happened just prior to the cruise (Brzezinski et al., *in prep*) or due

to storm-driven deepening of the ML. In addition, the high turbulence caused by the storms may have largely disaggregated marine snow in the ML (see section 4.2), allowing TEP to remain buoyant and accumulate in the ML and dense silica-rich particles to sink deeper. Detrital diatom frustules may have originated from the preferential remineralization of POC over bSi in sinking senescent diatoms (Brzezinski et al., in prep). Single diatom cells may have decreased their buoyancy and therefore sink in response to silica depletion as intact cells (Bienfang et al., 1982). Lastly, sediment traps deployed in P4 from May 22 to May 24 indicated an increase in aggregate and bSi fluxes in the upper mesopelagic above 500 m depth. Hence, at least partially, some of the small silica-rich particles may have originated from disaggregation of diatom aggregates while sinking rather than single sinking diatoms or their frustules.

Overall, we observed a first sedimentation event that developed during the storms and was characterized by small, silica-rich particles sinking in the upper mesopelagic and TEP accumulating in the ML water. Sinking diatoms were dominating a moderate POC flux, which reached 500 m depth by the end of the cruise and showed modest export ratio at 100 m depth.

High POC fluxes due to fast-sinking marine snow after the storm

We observed large and rapid sedimentation of fast-sinking marine snow during P5, after the storms ceased and more than three weeks after the actual diatom bloom. The composition of fast-sinking marine snow changed during the cruise and shifted from being dominated by detrital diatoms to a community that presented increased contributions of heterotrophic taxa (i.e., dinoflagellates and tintinnids) and intact diatoms by the end of P5. High concentrations of dinoflagellates and tintinnids have been observed before at the end of

diatom blooms indicating that these heterotrophs may be significant consumers of bloom-forming diatoms (Passow and Peinert, 1993; Tiselius and Kuylenstierna, 1996; Sherr and Sherr, 2007). The intact diatoms observed in P5 may have originated from the coagulation of healthy diatoms that were growing using the silicic acid injected by the mixed layer entrainment caused the storms (Brzezinski et al., *in prep*).

Concurrent with the increased sinking of marine snow in the upper mesopelagic, the concentration of TEP in the ML substantially decreased indicating that TEP coagulated forming marine snow as to be expected (Logan et al., 1995). Between P2 and P5, intense winds and surface waves generated by four strong storms (≥ 9 on the Beaufort wind force scale) led to strong turbulent kinetic energy dissipation rates (ε) in the ML (ML mean $\varepsilon > 10^{-5}$ W kg^{-1}) (Figure 1; Siegel et al., *in prep*) and a deepening of the ML depth by 25 to 45 m (Johnson et al., 2023). Turbulence has been found to enhance marine snow formation up to $\varepsilon = 10^{-6}$ W kg^{-1} (Takeuchi et al., 2019; Siegel et al. *in prep*.). However, for higher ϵ, disaggregation may outcompete aggregation and limit marine snow size (Alldredge et al., 1990; Takeuchi et al., 2019). After the last storm (P5), the turbulent dissipation energy in the ML decreased to values less than 10^{-7} W kg^{-1} which favors particle aggregation (Figure 1a; Siegel et al., in prep), and likely allowed the observed, exponential formation of fast-sinking marine snow. Turbulence may also help retain some large aggregates in the mixed layer (Alldredge et al., 1987), while mixed layer deepening may dilute particles. During P5 the shoaling of the ML to approximately 30 m may have allowed particles to concentrate in a relatively shallow water layer, potentially increasing collision rates between particles. It is therefore likely that the combination of moderate turbulence levels and a shallow ML depth triggered the rapid, exponential formation of fast-sinking marine snow that we observed in

the eddy core waters during P5. Data obtained using the Underwater Visual Profiler (Picheral et al., 2015) indicates the formation of large particles and loss of small particles above 150 m depth during P4–P5 (Siegel et al. in prep). Similar to these observations collected during EXPORTS, Giering et al., (2016) found a 2 orders-of-magnitude increase in the concentration of large particles above 100 m depth after a strong storm (9–10 on the Beaufort wind force scale) in the high latitudes of the North Atlantic. This data indicates the potential role of intense storms in delaying the formation and therefore sinking of marine snow.

The POC flux in P5 was on average 28±15 mmol C m^{-2} d^{-1} (n = 4) at 90–110 m and was 4.5 higher than the fluxes during the first sedimentation event. The largest POC flux at 100 m was estimated at the end of P5 (May 29) (51±15 mmol C m^{-2} d^{-1}) and was on the high end of observed upper ocean export fluxes (Mouw et al., 2016; Giering et al., 2023 spring bloom in South Georgia, 54 mmol C m^{-2} d^{-1}, 95 m). The export ratio at 100 m depth was also high, on average 0.6±0.3 (n = 4). We could not track fast-sinking marine snow below 200 m depth after May 29 because the cruise ended. However, their large carbon content (0.7 µg C agg^{-1}) and the high average sinking velocities of fast-sinking particles (97±30 m d-1, n = 3) suggest that this sedimentation event had the potential to rapidly transport and sequester POC below the winter ML (600 m in the North Atlantic, de Boyer Montégut et al., 2004). The measured average sinking velocity represents an average of the entire fast-sinking particle population, including particles smaller than 0.1 mm in diameter. Hence the large marine snow that we observed was likely sinking faster than our estimates. In addition, the sinking velocity measured at the beginning of P5 (May 25) may be an underestimation of the sinking velocity of the fast-sinking particles present in the water at the end of P5 (May 29). In fact, the

volumetric concentration of fast-sinking marine snow at 60 m depth increased by 3.5-fold during P5 increasing the proportion of marine snow to the total fast-sinking particle pool.

Our data indicates that the two sedimentation events likely overlapped. In P4, 24% of the POC concentration measured in sinking particles was due to fast-sinking marine snow at 85 m depth; however, between 125 m and 500 m depth, sinking diatoms were still dominating (99% of POC in sinking particles). Hence, our data suggests that most of marine snow did not sink below 85 m on May 22. By May 25 the contribution of fast-sinking marine snow increased to 39 % at 50–330 m. This comparison indicates that the contribution of marine snow to the POC flux was growing starting from P4. The overlap of the two events is also supported by drifting sediment traps data that show increased fluxes of biogenic silica, aggregates and POC in P4 (traps were deployed on May 22-24, Estapa et al., 2023).

Overall, our data indicate that storms delayed the formation and sinking of marine snow and by doing so created a second sedimentation event that allowed the sinking of POC, TEP-C and a transitioning, mixed plankton community, which likely would have not sunk otherwise.

Conclusions

Our work demonstrated that observations from the MSCs may complement the traditional suite of measurements (e.g., Niskin bottle, sediment traps and more recently UVP) taken at sea allowing determinations of particles not only according to their size but also sinking velocity. The MSCs enabled to observe the presence of two sedimentation events that contributed differently to POC flux following the main diatom export event at the end of a large spring diatom bloom. We found that a significant amount of the POC export of a spring diatom bloom may happen weeks after the main event. In addition, our

data suggests that intense storms may be important control factors in determining the efficiency of POC export and the plankton community that contributes to POC export during the decline of diatom blooms. Finally, we found that small silica-rich particles were the main contributors of a moderate POC flux event; while important in the upper mesopelagic, small sinking particles may not be efficient carbon exporters. This observation implies that export effectiveness does depends on the type of sinking particle. Ultimately, our findings suggest that increased storm severity due to climate change (e.g., Knutson et al., 2010) may have important implication on the efficiency of the biological carbon pump.

Tables

Date	Particulate organic carbon and nitrogen (POC and PON)	Total Particulate Carbon (TC)	Biogenic silica (bSi)	Lithogenic silica (lSi)	Sinking velocity of fast-sinking particles	Marine snow removed from the tray
May 7	X	X	X	X		X
May 12	X	X	X			X
May 13	X	X	X		X	X
May 14	X					
May 16	X	X	X	X		X (No counts)
May 17	X	X	X		X	X
May 18	X					
May 19	X	X	X			X
May 22	X	X	X			X
May 25	X				X	
May 26	X	X	X			X
May 27			X			X (Measured POC of marine snow)
May 28	X	X	X	X		X
May 29	X	X	X			X

Table 1. Analyses performed at each station sampled. The last column indicates in which station marine snow was sized, counted, and removed from the MSC tray. On May 16 such data were lost. On May 27, marine snow was filtered to measure the POC and PON mass but not counted quantitatively in the entire MSC trays.

<table>
<tr><th>Particle fraction from MSC</th><th colspan="3">Corrected particle fraction</th><th>Minimum size</th><th>Maximum size</th></tr>
<tr><td>Top</td><td colspan="3">Suspended particles</td><td>Filter pore size: approx. 0.3 µm</td><td>Unconstrained</td></tr>
<tr><td>Base</td><td colspan="2">(A) Small, slow-sinking particles</td><td rowspan="2">(E) Small sinking particles</td><td>Filter pore size: approx. 0.3 µm</td><td rowspan="2">ESD: 0.1 mm, sized visually with ruler</td></tr>
<tr><td rowspan="2">Tray</td><td rowspan="2">(B) Fast-sinking particles</td><td>(C) Small, fast-sinking particles</td><td>Filter pore size: approx.0.3 µm</td></tr>
<tr><td colspan="2">(D) Fast-sinking marine snow</td><td>ESD: 0.1 mm, sized visually with ruler</td><td>ESD: 6 mm, sized visually with ruler</td></tr>
</table>

Table 2. Nomenclature of distinct particle fractions sampled with the MSC and characterized in the present work. Bold text refers to the three particle fractions described in the results section. Letters (A)-(F) are used to identify particle fractions.

Depth (m)	P1–2	P3	P4	P5
40–100	23 ± 3 m d^{-1}	13 ± 3 m d^{-1}	43 ± 43 m d^{-1}	73 ± 10 m d^{-1}
125–150	17 ± 5 m d^{-1}	16 ± 4 m d^{-1}	16 ± 4 m d^{-1}	115 ± 35 m d^{-1}
175–500	15 ± 4 m d^{-1}	15 ± 4 m d^{-1}	15 ± 4 m d^{-1}	-
160–195	-		-	82 ± 9 m d^{-1}
300–500	-		-	42 ± 5 m d^{-1}

Table 3. Calculated average sinking velocities used to calculate POC fluxes due to fast-sinking particles.

Figures

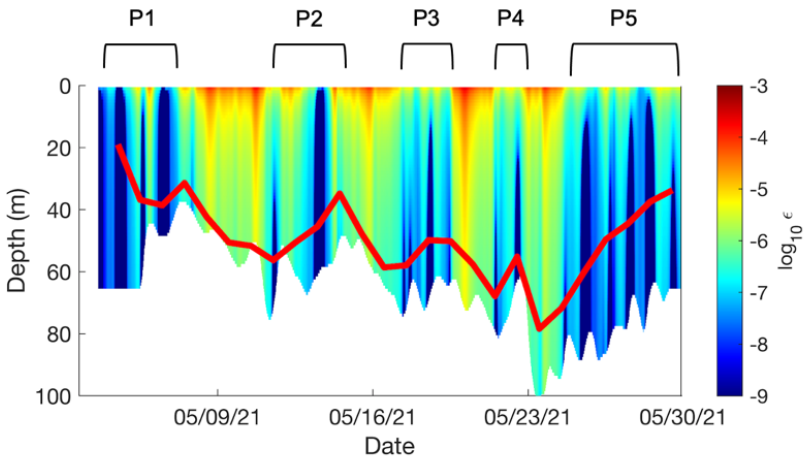

Figure 1. Turbulent kinetic energy dissipation rates (ε, W kg^{-1}) within the mixed layer during the cruise. Red line represents the depth of the mixed layer. The five time periods (P) constrained by the storms (P1: May 4–7; P2: May 12–14; P3: May 16–19; P4: May 22; P5: May 25–29) are represented above the figure.

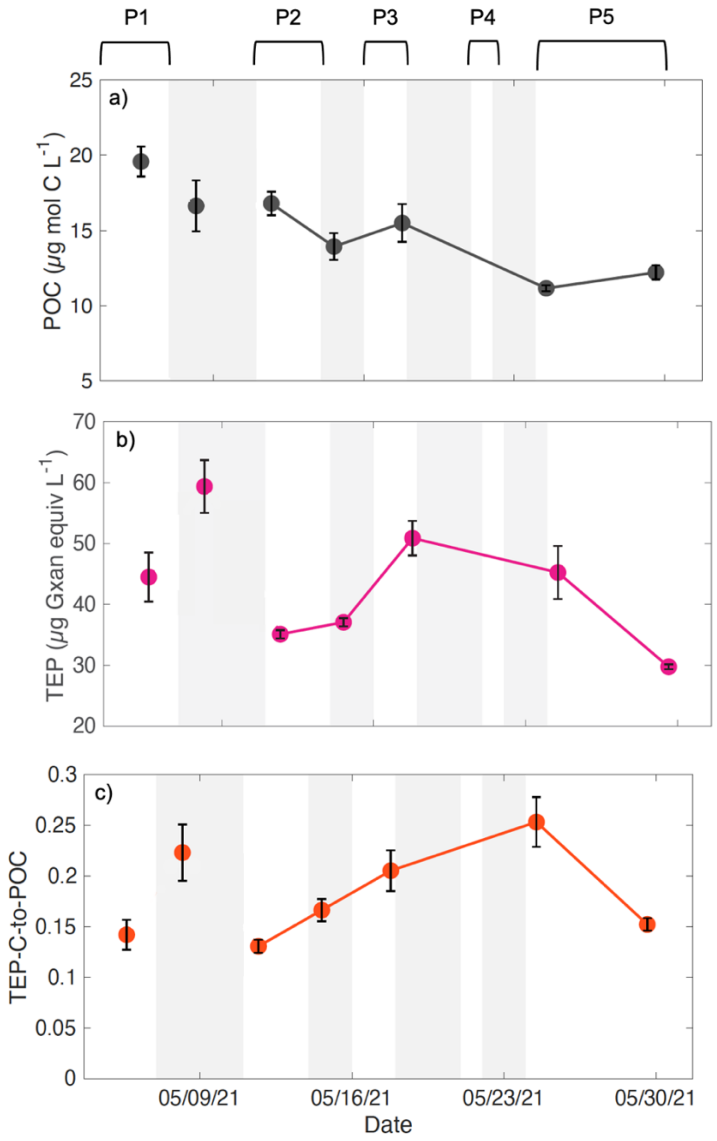

Figure 2. Change in the concentration of (a) POC and (b) TEP, and (c) TEP-C-to-POC ratios over time in seawater collected with Niskin bottles within the mixed layer at 21±5 m depth. Note that the observations from May 5 and 8 are not included in our temporal analysis because 73% of the ML water was exchanged by the first storm. Gray shading represents the storms, which made sampling impossible. The five time periods (P) constrained by the storms (P1: May 4–7; P2: May 12–14; P3: May 16–19; P4: May 22; P5: May 25–29) are represented above panel a).

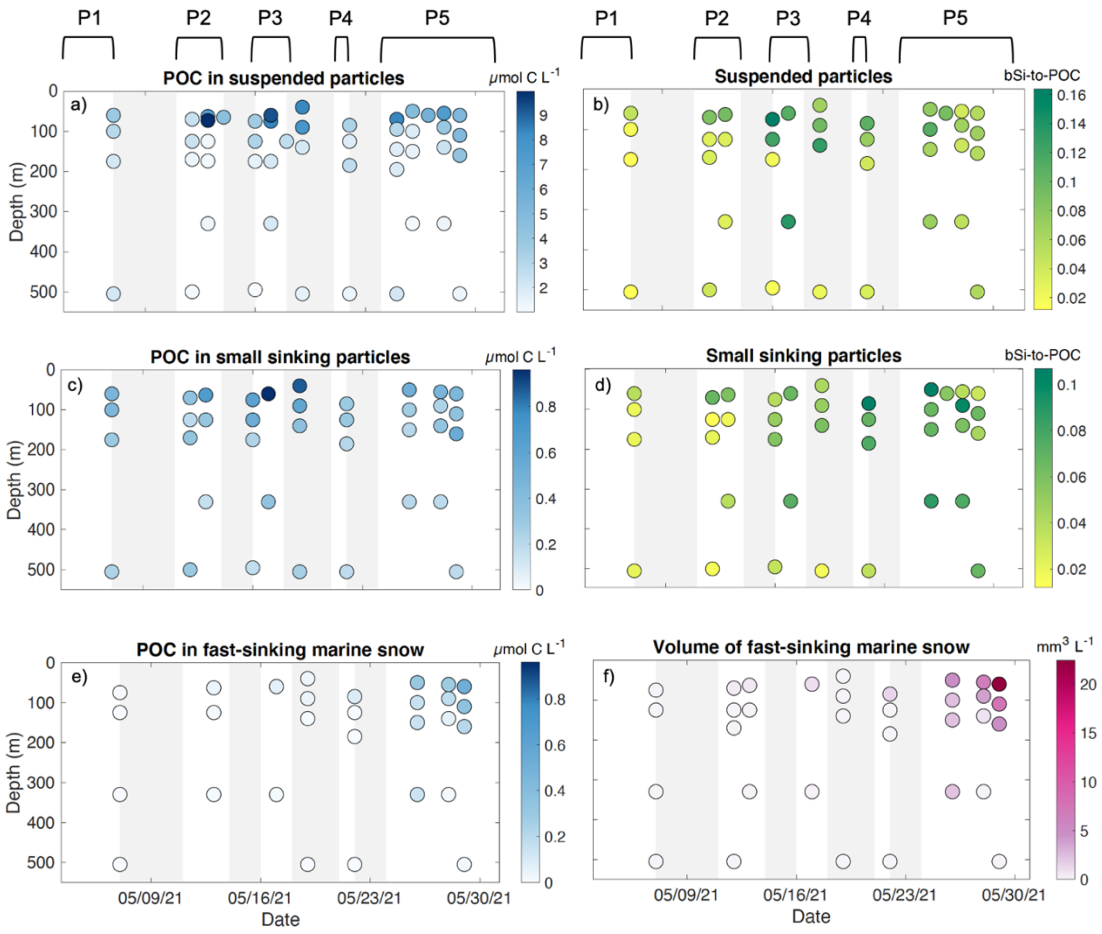

Figure 3. Top panels: Temporal change of (a) POC concentrations and (b) molar bSi-to-POC ratios in suspended particles between 40 and 500 m depth. Middle panels: Temporal change of (c) POC concentrations and (d) molar bSi-to-POC ratios in small sinking particles between 40 and 500 m depth. Bottom panel: Temporal change (e) POC concentrations and (f) volumetric concentrations of fast-sinking marine snow particles between 40 m and 500 m depth. Note: we do not have molar bSi-to-POC ratios of fast-sinking marine snow. Gray shading represents the storm periods. The five time periods (P) constrained by the storms (P1: May 4–7; P2: May 12–14; P3: May 16–19; P4: May 22; P5: May 25–29) are represented above plot a) and b).

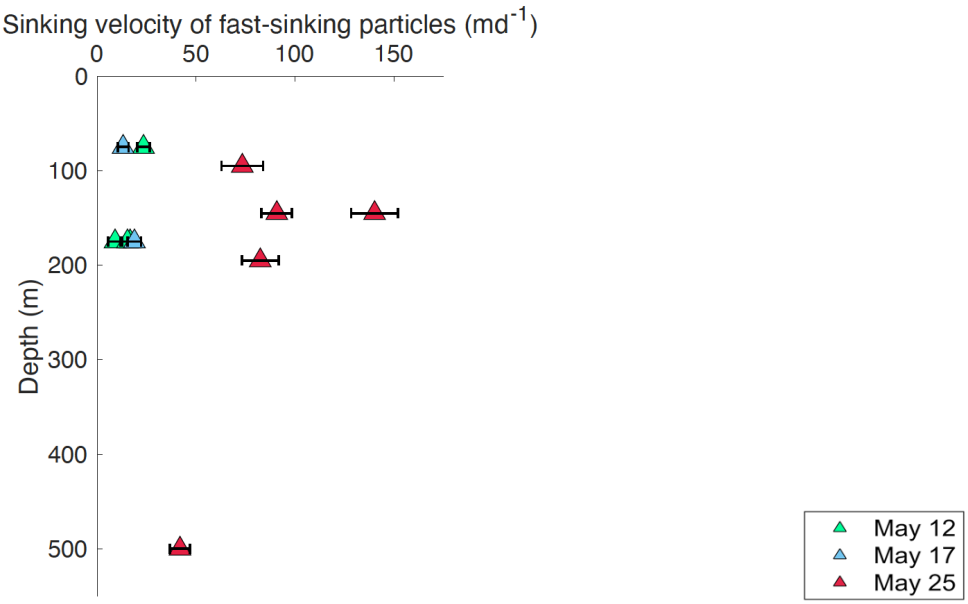

Figure 4. Temporal and vertical variability in the estimated the sinking velocities of fast-sinking particles (small, fast-sinking particles plus fast-sinking marine snow). Error bars are the propagated measurement standard deviations.

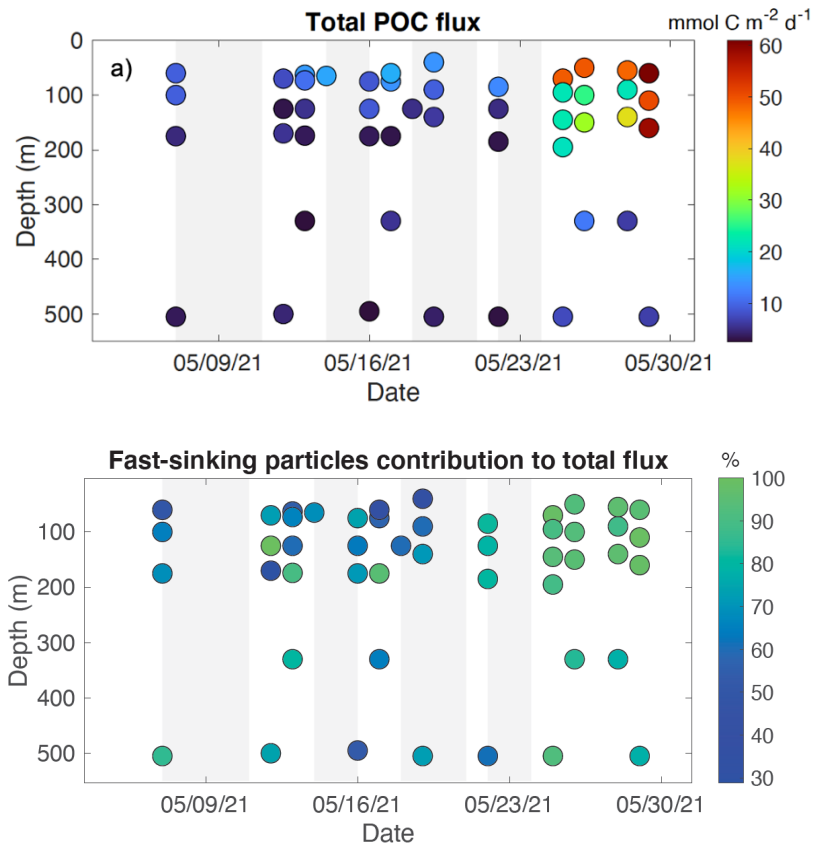

Figure 5. Temporal change of (a) total POC flux (due to both slow-sinking and fast-sinking particles) and (b) fractional (%) contribution of POC flux due to fast-sinking particles to total POC flux.

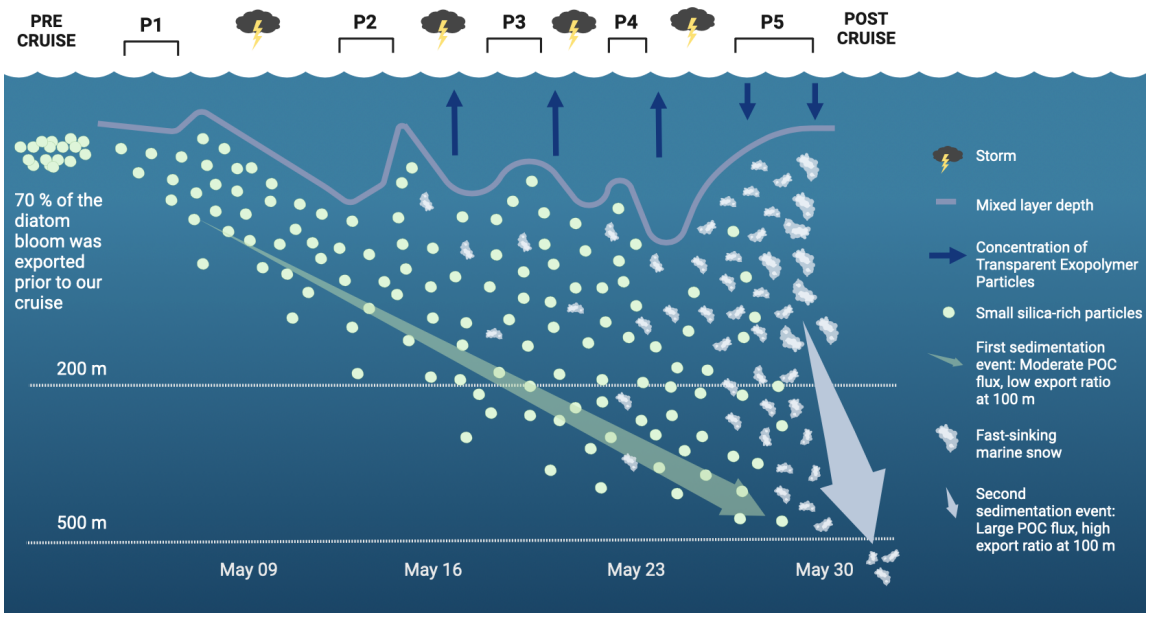

Figure 6. Schematic of the of the two sedimentation events that followed the main diatom export at the end of the diatom spring bloom.

Pre-cruise: Nutrient and biomass analysis revealed that a large diatom bloom had occurred and likely sank before our visit (Johnson et al., 2023; Brzezinski et al., *in prep*).

P2-P4: First sedimentation event (transparent green arrow): Small, silica-rich particles sank in the upper mesopelagic regardless of the presence of three intense storms. Concurrently, TEP accumulated in the ML water rather than aggregating and forming marine snow. This event was characterized by a moderate POC flux at 500 m depth and modest export ratio at 100 m depth.

P5: Second sedimentation event (transparent white arrow): The volume of fast-sinking marine snow increased exponentially, while TEP concentrations decreased. Marine snow appeared at the beginning of P5 when the storms ceased, turbulence was moderately intense and the MLD deceased to approximately 30 m depth. This event was characterized by a large POC flux at 200 m depth and high export ratio at 100 m depth.

Supplemental material

Figures

Figure S1. Example of microscopy photos of intact fast-sinking marine snow collected at 50 m on May 12 (a) and on May 29 (b) and of plankton associated with marine snow collected at 50 m on May 12 (c), May 17 (d) and May 29 (e).

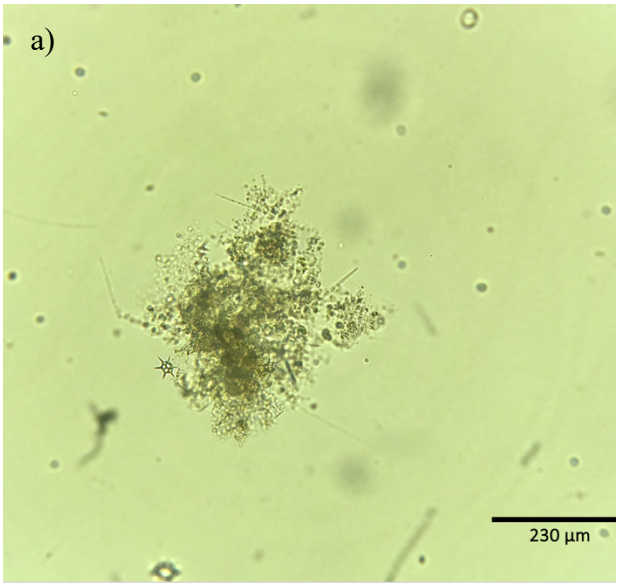

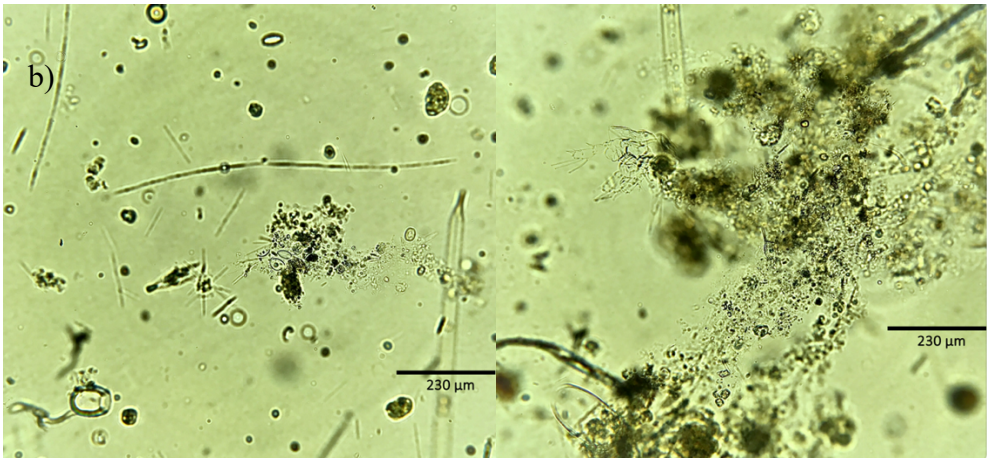

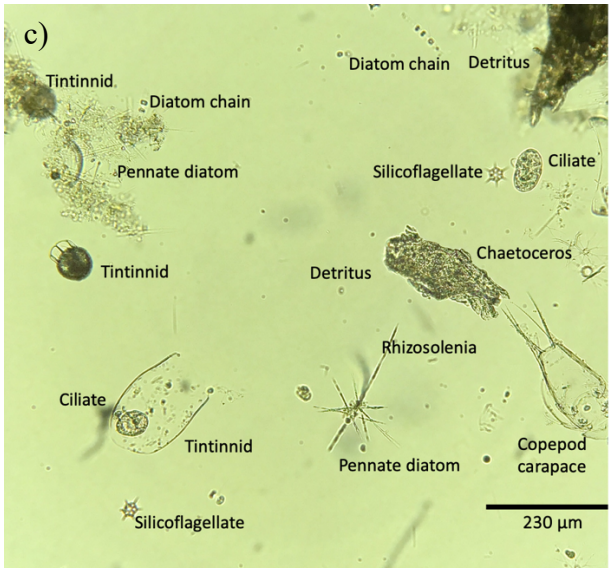
c)
Tintinnid
Diatom chain
Diatom chain
Detritus
Pennate diatom
Silicoflagellate
Ciliate
Tintinnid
Detritus
Chaetoceros
Rhizosolenia
Ciliate
Tintinnid
Pennate diatom
Copepod carapace
Silicoflagellate
230 µm

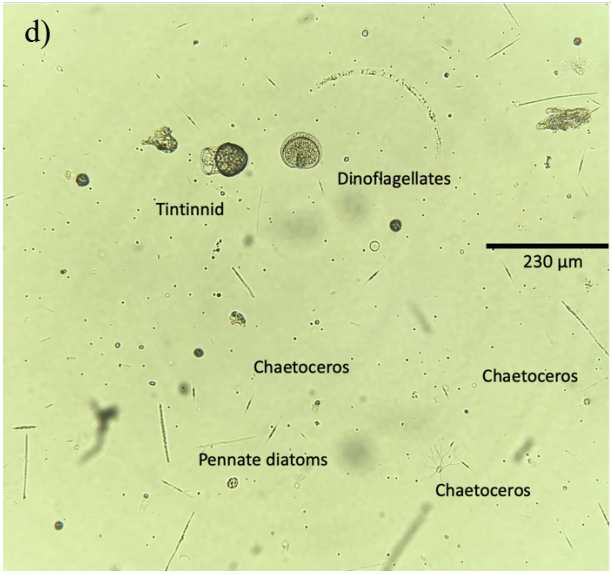
d)
Dinoflagellates
Tintinnid
230 µm
Chaetoceros
Chaetoceros
Pennate diatoms
Chaetoceros

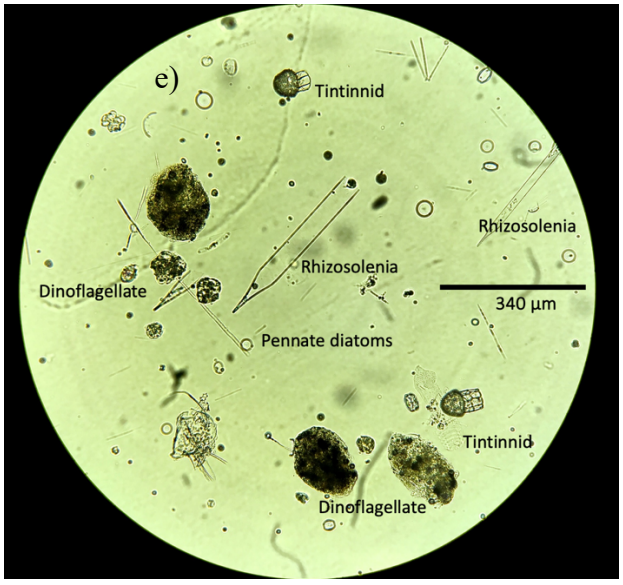
e)
Tintinnid
Rhizosolenia
Rhizosolenia
Dinoflagellate
340 µm
Pennate diatoms
Tintinnid
Dinoflagellate

Figure S2. Top panels: Temporal change of (a) POC (b) bSi concentrations in suspended particles between 40 and 500 m depth. Middle panels: Temporal change of (c) POC (d) bSi concentrations in small sinking particles between 40 and 500 m depth. Bottom panels: Temporal change of (e) molar PIC-to-POC ratios and (f) molar lSi-to-POC ratios in small sinking particles between 40 and 500 m depth.

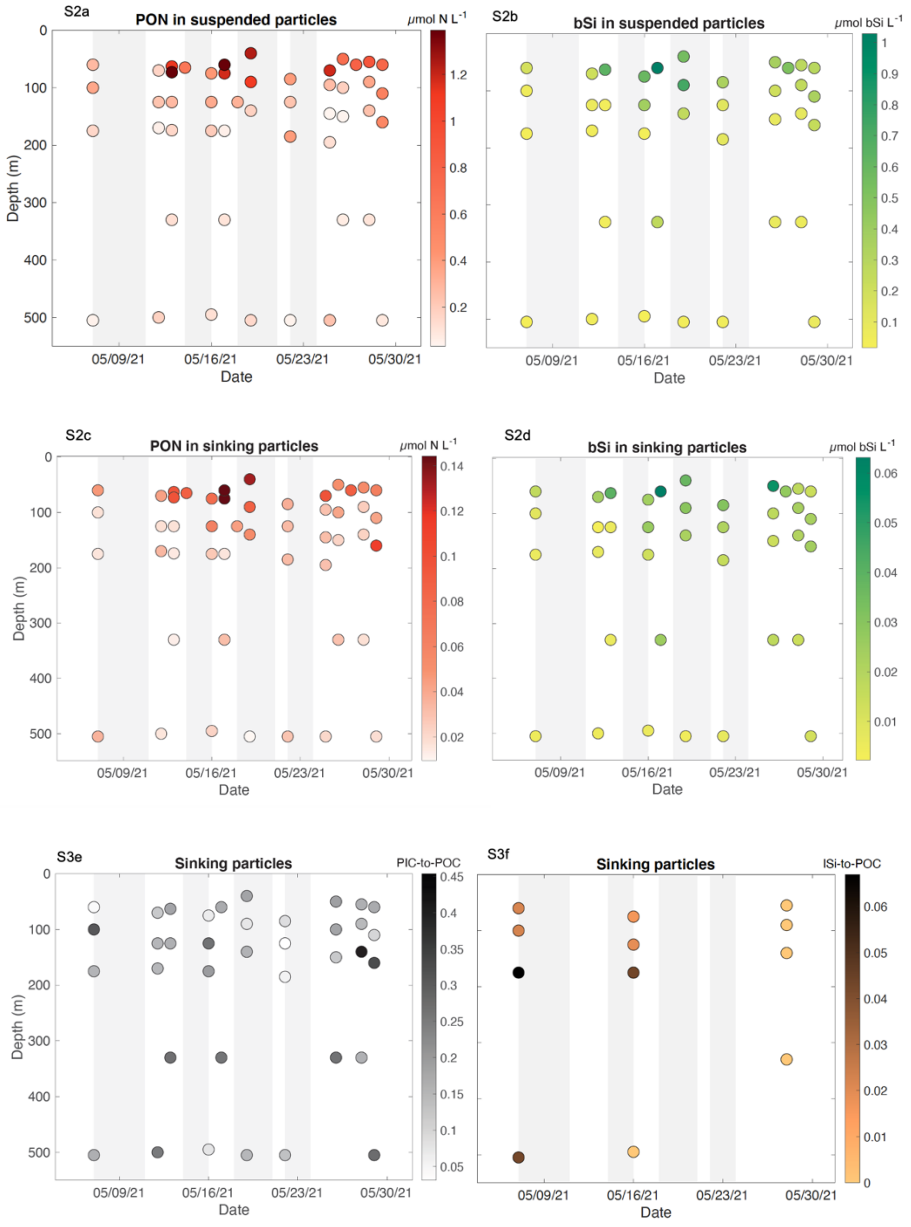

Tables

Table S1: The average relative standard deviation (RSD) of replicate measurements of POC and PON concentrations in each particle fraction collected with the Marine Snow Catcher.

RSD (%)	**T0**	**top**	**base**	**tray**
POC	9	8	12	10
PON	8	30	24	32

Table S2: The measured POC mass of fast-sinking marine snow of 1mm equivalent spherical diameter (ESD). Marine snow was collected at 60 m on May 27. Values marked as DL were below the detection limit (DL) of the analyzer.

Filtered fast-sinking marine snow	**Average POC**	**Average PON**
number	µg C aggregate^{-1}	µg N aggregate^{-1}
20	0.64	DL
20	0.58	0.08
20	0.66	0.14
10	0.58	DL
20	0.67	DL
20	0.44	DL
24	0.74	DL
20	0.93	0.23
Average	**0.65**	**0.07**
SD	**0.10**	**0.04**

III. Microbial activity on suspended and sinking particles during a Phaeocystis bloom in the Labrador Sea

Elisa Romanelli, Carolina Cisternas-Novoa, Rebecca Stevens-Green, Julie LaRoche, David A. Siegel, Craig A. Carlson, Uta Passow

Abstract

Microbial degradation of organic carbon below the euphotic zone exerts a direct control on the amount of carbon that the ocean stores in its interior. Spring *Phaeocystis* blooms in high latitudes produce a large amount of biomass (i.e., organic carbon); however, the role of microbes in controlling the fate of such carbon is yet to be elucidated. Here we quantified microbially driven removal of total organic carbon (TOC) within the suspended and sinking particle fractions from Marine Snow Catchers (MSCs). Samples were collected at three stations just below the Euphotic Zone (90–150 m) at different stages of a spring *Phaeocystis pouchetii* bloom in the Labrador Sea. The carbon-specific degradation rates differed between suspended and sinking particle fractions at two stations: rates for fast-sinking (> 18 m d^{-1}) and slow-sinking (~ 18 m d^{-1}) particles were similar (range: 0.03–0.07 d^{-1}) but were one order of magnitude larger than those found for the suspended fraction (0.002 d^{-1}, n = 2) at non-bloom stations. However, at the station characterized by abundant free-floating *Phaeocystis* colonies, the suspended fraction sustained approximately one order of magnitude higher degradation rates (0.01 d^{-1}) similar to those of the sinking fractions at all stations. This observation suggests that the presence of *Phaeocystis* colonies may have enhanced TOC's microbial removal rate. The fact that the TOC removal rates of slow- and

fast-sinking particles were on the same order of magnitude suggests that, under our sampling conditions, sinking velocity was an important factor controlling the transfer of carbon to depth.

Introduction

Sinking particles are the dominant pathway transporting organic carbon from the surface ocean into the ocean interior (e.g., Nowicki et al., 2022). The depth to which particulate organic carbon (POC) sinks and remineralized directly affects atmospheric CO_2 concentrations on climatologically relevant timescales (Kwon et al., 2009). There are two competing mechanisms that control the fates of sinking organic matter in the mesopelagic: particle sinking velocity and biotic consumption of particles. The relationship between these two mechanisms is complex and not well understood. Marine particles can be suspended in the water column, advected horizontally or sink vertically. Depending on the trophic state of the ecosystem (e.g., oligotrophic vs eutrophic), the sinking of particles may be differently influenced by particle size, density, porosity, and shape in a way that cannot always be predicted by Stokes' law (e.g., Iversen and Lampitt, 2020; Cael et al., 2021; Romanelli et al., 2023). The standard view is that particle transfer efficiency in the water column is positively linked to particle sinking velocity: i.e., the faster a particle sinks, the more efficiently organic matter is transported (most importantly POC) to depths where carbon is removed from the atmosphere for timescales > 100 years (i.e., deep mesopelagic, 500 m).

In the mesopelagic, zooplankton and heterotrophic prokaryotic bacteria rely on sinking particles as their main source of organic matter (Buesseler et al., 2007b; Steinberg et al., 2008). The interaction of zooplankton and heterotrophic bacteria with particles can retard particle sinking velocity by changing particle morphology and composition, and density.

Zooplankton and bacteria can directly respire POC into dissolved inorganic carbon (DIC), with bacteria being largely responsible for this remineralization (e.g., Ploug et al., 1999; Giering et al., 2014; McDonnell et al., 2015). In addition, particle-attached bacteria can perform mechanical disaggregation and enzymatic solubilization on POC (Azam and Malfatti, 2007), transforming POC into suspended or dissolved forms of organic matter that are then accessible to the free-living bacterial communities (Cho and Azam, 1988, Collins et al., 2015). Zooplankton can mechanically disaggregate POC via sloppy feeding and egest and excrete organic carbon as dense faecal pellets or DOC (Stemmann et al., 2004; Collins et al., 2015). Depending on the system, one or more of these processes may be predominantly contributing to the attenuation of the flux of POC in the mesopelagic (e.g., Giering et al., 2014; Steinberg et al., 2023).

Heterotrophic prokaryotic bacteria (or Archaea) can be operationally defined as free-living, or particle-attached. Taxa associated with particles generally show higher concentrations and activities than their free-living counterparts (e.g., Smith et al., 1992; Grossart et al., 2007) and can be phylogenetically distinct (Delong et al., 1993; Farnelid et al., 2018; Duret et al., 2019).

It is challenging to measure microbial activity in the mesopelagic zone. First, rates of bacterial processes are slow (Cho and Azam, 1988), hence they are difficult to detect and measure. Second, we lack a mechanistic understanding of how the environmental (e.g., temperature), biochemical (e.g., nutrient limitation) and ecological (e.g., particle sinking velocity, particle lability, competition) variables control the activity of bacteria on organic matter (Iversen and Ploug, 2013; Collins et al., 2015; Alcolombri et al., 2021, Amoano et al., 2022).

Here we present a novel approach to calculate carbon-specific removal rates on suspended, slow-sinking, and fast-sinking particle fractions collected with two Marine Snow Catchers (MSC; Lampitt et al., 1993). Particles were sampled during a *Phaeocystis pouchetii* bloom in the Labrador Sea at the base of the euphotic zone, where the export source material resides. *P. pouchetii* are ubiquitous and ecologically important phytoplankton that produce large free-floating colonies. The colonies are visible with the naked eye and are composed of cells embedded in a polysaccharide gel matrix (Pouchet,1982). The carbohydrates matrix may provide substrate for bacteria (Harvey et al., 1995); however, little is known about the relationship between *P. pouchetii* colonies and associated bacterial activity (Delmont et al., 2014). The goal of the present work was to investigate such a relationship.

Materials and Methods

Study site

Particle profiles were collected during "The North Atlantic as a climate ocean: Projecting future changes in productivity and the biological carbon pump" (NWA-BCP) field campaign in spring 2022 (May 19–June 2) on board the R/V *Celtic Explorer*. The cruise targeted different stages of an unusually large *P. pouchetii* bloom in the Eastern Labrador Sea. Three distinct areas were surveyed and are defined here according to the Chlorophyll *a* concentration measured in the water column between 80 m and 150 m depth (range of the base of the euphotic zone across stations). The station characterized by *Phaeocystis* in the bloom phase, will be called the *Phaeocystis* bloom station (PB) (58.650° N, -49.360° E), the station characterized by the lowest Chlorophyll *a* concentration is designated the low biomass station (LB) (59.507° N, -49.674° E) and the station characterized by Chlorophyll *a* concentrations that were intermediate between the PB and

LB station will be named the moderate biomass station (MB) (57.724° N, -50.066° E) (Figure 1).

Collection and characterization of suspended and sinking particles

Suspended and sinking particles were collected with two 100-liter Marine Snow Catchers on May 22 at station PB, on May 27 at station MB and on June 1 at station LB. Deployment depth was set to approximately 10 m below the base of the euphotic zone and was 150 m for PB, 130 m for MB and 90 m for LB. The MSC is a water sampler with a detachable top that enable separate collection of suspended particles, slow-sinking particles, and fast-sinking particles after a pre-defined settling time of 2 hours (Riley et al., 2012; Giering et al., 2016). The MSC methodology used here is described in Romanelli et al., 2023. Briefly, we collected three particle fractions according to their sampling location within the MSC directly after 2 hours of settling: *top*, *base*, and *tray* particle fraction. The top fraction was collected from the central tap and contained suspended particles. To separate slow- from fast-sinking particles, a circular plastic tray (polypropylene, diameter: 18.5 cm; height: 4 cm; volume: ~1L) was placed at the bottom of the MSC's base. After draining and removing the top section of the MSC, water overlying the tray in the base section was collected constituting the *base* particle fraction. The particle fraction in the tray was considered the *tray* fraction.

The concentrations of suspended, slow-sinking, and fast-sinking particles were calculated from the measured concentrations of *top*, *base* and *tray* particle fractions by subtracting the *top* fraction from the *base* fraction and the *base* fraction from the *tray* fraction. The differences were scaled for the volume ratios as follows:

Suspended fraction = *top* concentration (*1*)

Slow-sinking particles = (*base* – *top* concentrations) × V_{base} / V_{MSC} (*2*)

Fast-sinking particles = (*tray* – *base* concentrations) × V_{tray} / (A_{tray} × h_{MSC}) (*3*)

where V_{MSC} = 89.8 L, V_{base} = 5 L, V_{tray} = 1 L, and h_{MSC}= 1.5 m.

The sinking velocity of slow-sinking particles is on average 18 m d^{-1} and is calculated by dividing the height of the MSC by the settling time of 2 hours (Giering et al., 2016). Fast-sinking particles sank on average at > 18 m d^{-1}; however, the MSC methodology does not allow to constrain the sinking velocity any further.

Experiments to measure total organic carbon removal by bacteria

Magnitude and rates of total organic carbon (TOC) removal over time were determined by performing incubation experiments (maximum length of 11 days) on unfiltered MSC *top*, *base*, and *tray* fractions. The incubations were performed in the dark and at 4.4°C, which is 0.9°C warmer of *in situ* temperature using a refrigerated incubator. *Top*, *base*, and *tray* fractions each were incubated in fifteen (three replicates per each of the five time points) pre-combusted (4 h at 450°C) 40-mL borosilicate glass incubation vials. Samples in the vials did not contain any visible mesozooplankton, therefore we can assume that the measured activity was dominated by bacteria. At each time point triplicate samples from each treatment were fixed with 50 µL of DOC-free 4-N HCl five times over the course of the experiments (Figure 4). Concentrations of TOC in the incubated water was determined on land via the high-temperature combustion method using a modified Shimadzu TOC-V analyzer (Halewood et al., 2022). The precision for most of the analytical runs presented here was within ± 0.7 µM C for this study. All the TOC concentrations measured in the

MSC fractions were > 50 μM C. Concentrations of TOC of the suspended, slow-sinking, and fast-sinking fractions were calculated following equations (1), (2) and (3). Average TOC removal rates (d^{-1}) were calculated from the TOC concentrations calculated as explained in section 2.2 as follow:

$$\frac{\text{TOC (DayBeginning)} - \text{TOC (Day11)}}{\text{TOC (DayBeginning)}} \times \frac{1}{(\text{Day11} - \text{DayBeginning})} \quad (4)$$

We calculated rates associated with slow- and fast-sinking particles starting from the second time point (i.e., Day 2 for station PB and MB and Day 4 for station LB). We removed TOC concentrations measured on Day 0 because TOC concentrations associated with the *base* particle fraction at station PB and MB were lower than the one measured at the second time point. We assume that those vials were not fixed properly. To make the rates comparable, we applied the same "correction" at station LB. Removal rates calculated starting from day 2 and 4 are likely conservative, because degradation rates are expected to decrease over time as bioavailable (labile) material is degraded first.

Samples from the initial incubation water (Day 0) were also analyzed to determine the concentration of particulate organic carbon (POC), amino acids degradation index and the microbial community using 16s rRNA sequencing.

Measurements of POC

Concentrations of particulate organic carbon and nitrogen (POC and PON) were determined by filtering subsamples onto two pre-combusted (450 °C, 30 minutes) replicate GF/F filters (25 mm, Whatman, UK). After treatment with 150 μL of 10% HCl (v/v), samples were analyzed on a Perkin Elmer 2400 CHN Analyzer with acetanilide standards.

The accepted precision of elemental analysis results is 0.4%. Before calculating the concentration of POC and PON, their measured mass was blank corrected to account for contamination using the POC and PON mass measured on two virgin blanks (0.028±0.001 mg for POC; 0.002 mg for PON). Blank values are in the same range as those obtained during the EXPORTS field campaigns in the subarctic North Pacific and Northeast North Atlantic (Graff et al., 2023; Romanelli et al., *in prep*). All samples yielded values greater than the detection limit and the blank.

Heterotrophic prokaryotic community composition

Water samples of 200 mL to 1 L were filtered onto 25 mm, 0.2-µm polycarbonate nucleopore filters using vacuum filtration, until there was enough biomass collected. Filters were immediately stored on board at - 80°C. The DNA was extracted from the filters using the DNeasy Plant Mini Kit (Qiagen, Germany). The protocol was modified as follows: the lysis procedure was augmented by incorporating a 5-minute incubation with 50 µL of 5 mg/mL lysozyme (Fisher BioReagents, UK) followed by a 1-hour incubation with Buffer AP1 and 45 µL of 20 mg/mL Proteinase K (Fisher BioReagents, UK) (Zorz et al., 2019). DNA was eluted twice in 50 µL of the AE buffer (Qiagen, Germany) and measured on the NanoDrop 2000 (Thermo Scientific, US). The V4-V5 region of the 16S ribosomal RNA was seuqneced with Illumina MiSeq (300 + 300 paired-end sequencing) at the Integrated Microbiome Resource (IMR; Dalhousie University, Halifax, NS). Libraries were prepared as outlined in Comeau et al. (2017) with the 515FB = GTGYCAGCMGCCGCGGTAA and 926R = CCGYCAATTYMTTTRAGTTT primers (Parada et al., 2016; Walters et al., 2016). Sequencing data was processed using the QiiME 2 pipeline (version 2019.7.0) with DADA2 (version 2019.7.0) for quality control and denoising of 16S rRNA gene amplicon sequences

(Bolyen et al., 2012; Callahan et al., 2016). Raw reads were demultiplexed and quality filtered using default parameters in QiiME, including removal of sequences with low quality scores and chimeric sequences. Forward and reverse reads were then truncated at positions F = 267 and R = 199, respectively, to remove low-quality regions. The resulting sequences were then dereplicated and merged, followed by removal of singletons and chimera sequences using the consensus method implemented in DADA2 (Yilmaz, et al., 2014). The remaining high-quality sequences were then classified using the SILVA v138 reference database. To remove chloroplast sequences from the bacterial 16S rRNA gene amplicon data, the resulting chloroplast sequences were then classified using the Phytoref reference database implemented in QiiME 2's feature-classifier plugin to identify phytoplankton taxa (Decelle et al., 2015).

Results

Characterization of suspended and sinking particle fractions

At the PB station, we observed abundant intact *P. pouchetii* colonies with the naked eye (Figure 2) in all MSC fractions, especially in the suspended fraction. No visible colonies were present at stations MB and LB.

Mean ($\pm$ s.d.) concentrations of POC of suspended particles were highest at station PB (6.0 ± 0.5 µmol C L^{-1}, 150 m) and lowest at station LB (3.8 ± 0.3 µmol C L^{-1}, 90 m) (Figure 3). The MB station was characterized by concentrations slightly lower than PB (5.2 ± 0.1 µmol C L^{-1}, 130 m) (Figure 3). In sinking particles, the highest POC concentration (0.82 ± 0.13 µmol C L^{-1}) was measured for fast-sinking particles collected at station MB and slow-sinking particles collected at PB (0.60 ± 0.43 µmol C L^{-1}) (Figure 3). Concentration of POC in the other sinking fractions ranged between 0.13–0.44 µmol C L^{-1}

(Figure 3). The contribution of suspended particles to total POC was similar across stations and the highest across particle fractions (range: 85–89 %). Sinking particles contributed 11–15 % across stations (Figure 3), with no difference between slow- and fast-sinking particles.

The initial TOC concentration (Day 0) of the suspended fraction (unfiltered) was the highest at station PB and the lowest at station MB and was 9-fold greater than the initial POC concentrations for all stations. The TOC concentrations of slow-sinking particles at station PB were 2-fold higher than at station MB and LB throughout the entire experiments starting from Day 2 (Figure 4). Concentrations of TOC of fast-sinking particles were similar across stations on Day 4 (Figure 4). For sinking particles, we can compare concentrations of TOC and POC measured from Day 0 only at station LB (see section 2.3 for explanation), where POC was about 83% of the TOC for fast-sinking particles and about 43 % for slow-sinking particles.

Assessment of TOC removed by microbial processes

We observed a strong and significant linear decrease in the TOC concentrations over the entire incubation time in all particle fractions and stations (R^2 = 0.70–0.93, $p \leq 0.08$, n = 5) except for the suspended fraction and slow-sinking particle fraction of MB station (R^2 =0.51-0.56, p = 0.15–0.28, n = 5) (Table 1). Here TOC concentrations clearly decreased but reached an asymptote before the end of the 11-days incubation (Figure 4).

The significant decrease of TOC concentration over time enabled us to reliably calculate the TOC removal rates.

Total organic carbon removal rates

Sinking particle fractions showed the highest TOC removal rates (Table 2). Overall, the slow- and fast-sinking particle fractions sustained one order of magnitude higher TOC degradation rates in respect to the suspended fraction except for the *Phaeocystis* bloom station (PB) where the rates associated with the suspended fraction and sinking particles were within the same order of magnitude (Table 2). The highest degradation rate measured on sinking particles was associated with fast-sinking particles in the low biomass station (LB) (Table 2). Whereas the rest of the sinking particle fractions had similar degradation rates regardless of station sampled and sinking velocity characterization (Table 2).

Discussion

Cruise context

Preliminary data on nutrients and Chlorophyll *a* concentration, and phytoplankton community composition indicate that in the PB station, we sampled a *P. pouchetii* bloom. Station PB was characterized by abundant suspended Phaeocystis colonies (Figure 2) and by the highest Chl *a* concentration among stations (Figure 1). *P. pouchetii* was the most abundant phytoplankton taxa observed at all stations (Stevens-Green pers. Comm.). However, we did not observe free-floating Phaeocystis colonies at station MB and LB. The moderate biomass (MB) station had nutrient concentration profiles similar to those at station PM, although slightly lower (Figure 6), and was characterized by Chl *a* concentrations measured below the euphotic zone lower than the PB station but higher than the LB station (Figure 1). The low biomass station (LB) had the lowest Chl *a* concentration measured below the euphotic zone (Figure 1), and relative abundance of diatoms was higher compared to the other stations (Stevens-Green pers. Comm.). The LB station was characterized by the

lowest surface nutrient concentrations (NO_3, SiO_4 and PO_4) across stations (Figure 6). The concentration of surface silicic acid at station LB was indeed twice as low in respect to the other two stations and the NO_3 concentrations were at or below the limit of detection at station LB. These observations may indicate that we may have sampled the end of a diatom bloom at station LB.

Methodological considerations

To our knowledge, this is the first time that TOC removal rates has been successfully directly resolved for a variety of sinking particle types. The precision of the TOC analyzer is ± 0.7 μM C at these concentrations; thus, obtaining a signal associated with sinking particles is difficult. By using the MSC methodology we were able to concentrate various particle fractions to concentrations that improved the signal-to-noise ratio and allowed us to confidently resolve changes in TOC. The MSC method has been used before to calculate rates of microbial activity on the different particle fractions (Baumas et al., 2021; Garcia-Marti et al., 2021). However, it does not allow to estimate the microbial activity associated uniquely with particles (Garcia-Marti et al., 2021). As mentioned in section 2.2, the MSC *base* fraction contained suspended and slow-sinking particles, and the *tray* fraction contained all three types of particles. Furthermore, all the incubated MSC fractions contained dissolve organic matter. Based on these considerations, we cannot exclude that, at least partially, the activity calculated on sinking particles may have been due to the activity of free-living bacteria utilizing the DOC present at the beginning of the experiment and/or released by particle-attached bacteria during the incubations. Hence, our experiments include the processes of bacteria remineralization and solubilization performed by free-living and particle-attached bacteria.

The TOC removal measured on the suspended fraction was due to the combined activity of free-living and particle attached bacteria: on Day 0 the contribution of POC to TOC in the suspended fraction was <10 % (Figure 3). In contrast, the subtraction of the MSC *top* fraction from the *base* fraction and of the *base* fraction from the *tray* fraction (section 2.2) should theoretically have removed most of the signal associated with free-living bacteria and DOC from the results of the sinking particle fractions. In the fast-sinking particles fraction collected at station LB, POC was 83 % of the TOC concentrations (TOC =0.40±0.04 μmol C L^{-1}; POC = 0.33±0.08 μmol C L^{-1}, Figure 3). This suggest the measured TOC drawdown on the fast-sinking particle fraction was mainly reflective of microbial activity on POC. However, in the slow-sinking particle fraction POC was 43 % of the TOC concentration (TOC = 0.37±0.06 μmol C L^{-1}; POC = 0.16±0.04 μmol C L^{-1}, Figure 3). The difference between TOC and POC observed on slow-sinking particle may imply rapid solubilization of POC into DOC. Our comparison for sinking particles is limited to the low biomass (LB) station (section 2.3) and hence we cannot assess which process contributed to the signals. It is important to note that sinking particles are not isolated in the ocean, but they are surrounded by suspended particles and dissolved organic matter. Hence free-living bacteria may benefit from the dissolved organic matter released during the remineralization of the sinking particles (Cho and Azam, 1988; Kiørboe & Jackson, 2001; Collins et al., 2015; Garcia-Marti et al., 2021).

Our TOC removal rates are within the reported global literature range of 0.001–0.5 d^{-1} (Iversen and Ploug, 2013; Collins et al., 2015; McDonnell et al., 2015; Belcher et al., 2016; Alcolombri et al., 2021; Garcia-Marti et al., 2021). Furthermore, removal rates calculated for sinking particle align with rates estimated under similarly low temperatures

with artificial diatom aggregates (4.4 °C, Iversen and Ploug, 2013). This comparison supports the validity of our data; however, we refrain from performing an in-depth comparison between our rates and those published because we cannot rule out the possibility that our estimates include the contribution of POC solubilization and subsequent removal of DOC by free-living bacteria. Previous published work also converts oxygen removal rates to carbon-respiration rates by assuming a variable respiration quotient (e.g., (Iversen and Ploug, 2013; Garcia-Marti et al., 2021) making it difficult to reconcile the various approaches. We instead focus on discussing differences in rates across MSC fractions. Microbial respiration is a strong effected by temperature (Hoppe et al., 2008; Iversen and Ploug, 2013); therefore, all incubations were conducted at in situ temperatures; making them directly comparable.

Role of Phaeocystis pouchetii bloom

This study presents the first microbial degradation rates associated with suspended and sinking particles during a *Phaeocystis* bloom.

We found that the TOC removal rate of the suspended fraction at the PB station was approximately one order of magnitude higher than the rates obtained for the suspended fractions at the other two stations (Figure 5, Table 2). The PB station was characterized by abundant and intact suspended *Phaeocystis* colonies embedded in visible gel-like particles (Figure 2). Hence, our data suggest a link between the presence of suspended *Phaeocystis* colonies and the comparatively higher TOC removal rate for the suspended fraction. During the survey, suspended *Phaeocystis* colonies were significantly enriched of two types of gel-like particles (> 0.4 μm, filter pore size): carbohydrates-rich transparent exopolymer particles (TEP), which are a known constituent of *Phaeocystis* colonies (Mari et

al., 2005) and protein-rich coomassie stainable particles (CSP) (Cisternas-Novoa et al., *in prep*). Extracellular particulate carbohydrates (i.e., TEP) released by phytoplankton are remineralized by bacteria at a faster rate than other forms of POC (i.e., biomass) (Harvey et al., 1995). Therefore, our observations suggest that station PB had considerably more bioavailable suspended material than the other two stations. Indeed, the largest TOC removal was measured on the suspended fraction at the bloom station within the first 2 days of incubations. In contrast, the carbon present in the MB station, may have been more recalcitrant.

Data from collaborators will inform on the bloom stage of *Phaeocystis* during our survey. Furthermore, as part of this study, amino acid degradation index will inform on the lability of particles, and sequencing data will inform on the microbial community present at collection. Overall, these data will allow to further investigate the link between *Phaeocystis* colonies and microbial activity on suspended and sinking fraction collected with the MSC.

Rate differences among MSC fractions

We found one order of magnitude higher removal rates on sinking particle compared to the suspended fractions at stations MB and LB. (Figure 5, Table 2). One reason for this substantial difference may be that the suspended fraction was more diagenetically altered and less bioavailable (more recalcitrant) than the sinking particle fraction, which is presumably freshly produced and less diagenetically altered (more labile) (Kaiser and Benner, 2009; Benner and Amon, 2015). In section 4.3, we suggest that the lability of suspended *Phaeocystis* colonies may explain the higher TOC removal rate measured on the suspended fraction at the bloom station (PB) in respect to the non-bloom stations (MB and

LB). Similarly, at the MB and LB stations, the *Phaeocystis* colonies may had already formed sinking aggregates (bloom decline). If that was the case, then sinking particles would be characterized by higher removal rates than the suspended fractions.

Our data also show that TOC degradation rates associated with sinking particles were similar for the slow- and the fast-sinking particle fractions. Sinking velocity is an important factor controlling the transfer of carbon, i.e., for the same TOC removal rates, the remineralization length scale i.e., the depth at which organic carbon is remineralized to inorganic carbon, is longer for fast-sinking particles (e.g., Buesseler and Boyd, 2009). This comparison suggests that slow-sinking particles may have contribute more than fast-sinking particles to the metabolic carbon requirements in the mesopelagic.

Across the spectrum of sinking particles, the highest removal rate (0.07 d^{-1}) was observed on fast-sinking particles collected at the low biomass station (LB). This station was characterized by decreased surface nutrients and the increased presence of diatoms. Diatoms sinking as result of bloom decline may explain the higher removal rate at station LB (Amin et al., 2012).

Amino acidic data and information about the bloom stage at the three stations may help addressing the differences we found across the MSC fractions and stations.

Method limitations

Our method has some important limitations. One is the so called “bottle effect”: our incubations are performed in small, closed vials as such our experiments may have enhanced bacterial degradation and favor the colonization of bacteria that would not dominate under natural conditions (Ionescu et al. 2015). Something else to consider is that incubation of small volumes likely underestimates degradation rates. Large carbon-rich aggregates are hot

spot of microbial activity and are rare and heterogeneously distributed in the water column, hence they are underrepresented in small volume incubations. Lastly our experiments have been performed under ambient pressure, but water and associated microbes were collected between 90 m and 150 m depth. Pressure has been found to significantly slow down microbial degradation and impact prokaryotic diversity (Tamburini et al., 2009; Tamburini et al., 2021; Amano et al., 2022). However, little is known about the effect of pressure between our depth range. It would be useful to apply our approach using pressure chambers to test the effect of hydrostatic pressure on TOC drawdown.

Conclusions

We presented a novel approach to directly measure the TOC removal rates on suspended and sinking particles collected with the MSC. Furthermore, we provided the first TOC removal rates associated with suspended and sinking particles during different stages of a *P. pouchetii* bloom. Our results indicate that suspended colonies of *P. pouchetii* may have enhanced the TOC removal rate measured on the suspended fraction at the *Phaeocystis* bloom station. The consequence would be a decreased efficiency of the BCP and of the POC export below the euphotic zone. Our work also highlights the importance of investigating the lability of gels-like particles and not only measuring their abundance as these particles may have different lability depending on bloom phase. Finally, microbial rates were comparable across slow- and fast-sinking particles: hence, sinking velocity was an important factor controlling the efficient transport of POC at depth.

Tables

Station	**Suspended fraction**	**Slow-sinking particle fraction**	**Fast-sinking particle fraction**
Phaeocystis Bloom (PB)	Slope = -0.45 SE = 0.17 p = 0.07 R^2 = 0.70	Slope = -0.017 SE = 0.006 p = 0.09 R^2 = 0.83	Slope = -0.008 SE = 0.001 **p = 0.02** R^2 = 0.96
Moderate biomass (MB)	Slope = -0.086 SE = 0.044 p = 0.15 R^2 = 0.56	Slope = -0.011 SE = 0.008 p = 0.28 R^2 = 0.51	Slope = -0.009 SE = 0.002 **p = 0.05** R^2 = 0.89
Low biomass (LB)	Slope = -0.14 SE = 0.02 **p = 0.008** R^2 =0.93	Slope = -0.012 SE = 0.002 **p = 0.009** R^2 = 0.92	Slope = -0.025 SE = 0.005 **p = 0.016** R^2 = 0.89

Table 1. Slope, standard error (SE), significance (p-values, in bold if ≤0.05) and strength (R^2) of a linear regression model (fitlm, matlab) used to test the correlation between the decreased in the TOC concentration over time during the incubation experiments across all fractions. Yellow highlights incubations where most of the degradation happened rapidly within two time points and hence a linear model is not the most appropriate fit. Light blue highlights the incubations where the TOC drawdown plateaued before the end of the experiments, here as well a linear model is not the most appropriate fit.

MSC fraction	Phaeocystis bloom (PB) station	Moderate biomass (MB) station	Low biomass (LB) station
Suspended fraction	0.01 ± 0.0003	0.002 ± 0.0001	0.002 ± 0.0001
Slow-sinking particle fraction	0.02 ± 0.002	0.04 ± 0.003	0.03 ± 0.004
Fast-sinking particle fraction	0.03 ± 0.002	0.03 ± 0.001	0.07 ± 0.003

Table 2. TOC degradation rates (d^{-1}) associated with the suspended fraction and, the slow-sinking and fast-sinking particle fraction for the three stations (PB, MB and LB). SD is the standard deviation of the means of the replicates (n = 3) propagated through the applied calculations (section 2.2 and 2.3).

Figures

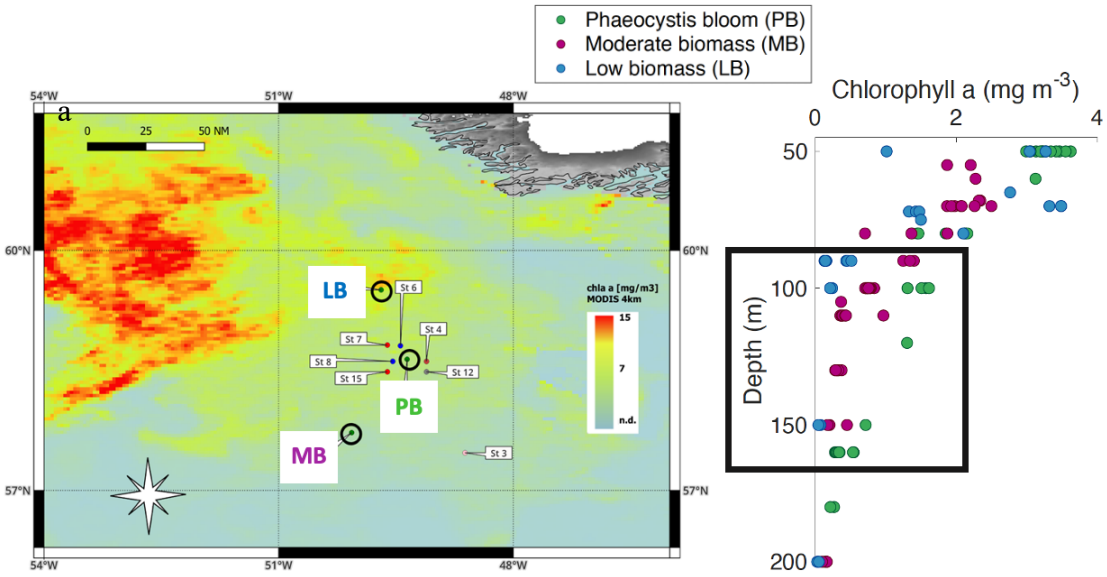

Figure 1. (a) Map of 4 km monthly average Chlorophyll *a* data from NASA's Moderate Imaging Spectroradiometer (MODIS). (Cisternas-Novoa et al., *in prep*), black circles indicate the three stations (PB, MB, LB) where the MSCs were deployed. (b) Vertical profile of Chlorophyll *a* concentration (mg m^{-3}) measured on water collected with Niskin bottles at the three stations. Black square highlights the MSC deployment depths and shows that PB station had the highest Chlorophyll *a* concentration among the three stations, whereases LB had the lowest.

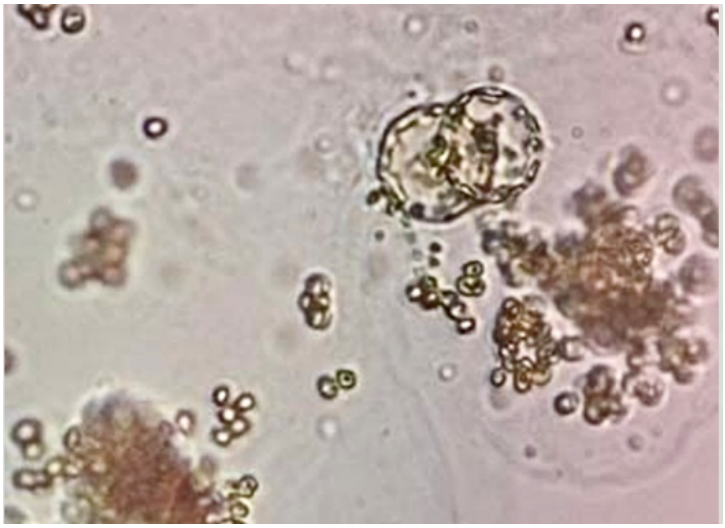

Figure 2. Suspended *P. pouchetii* colonies and two diatoms collected on May 23 in the station characterized by a *P. pouchetii* bloom. Water was collected using a Niskin bottle and imaged with the PlanktonScope. Image courtesy of Dr. Loay Jabre.

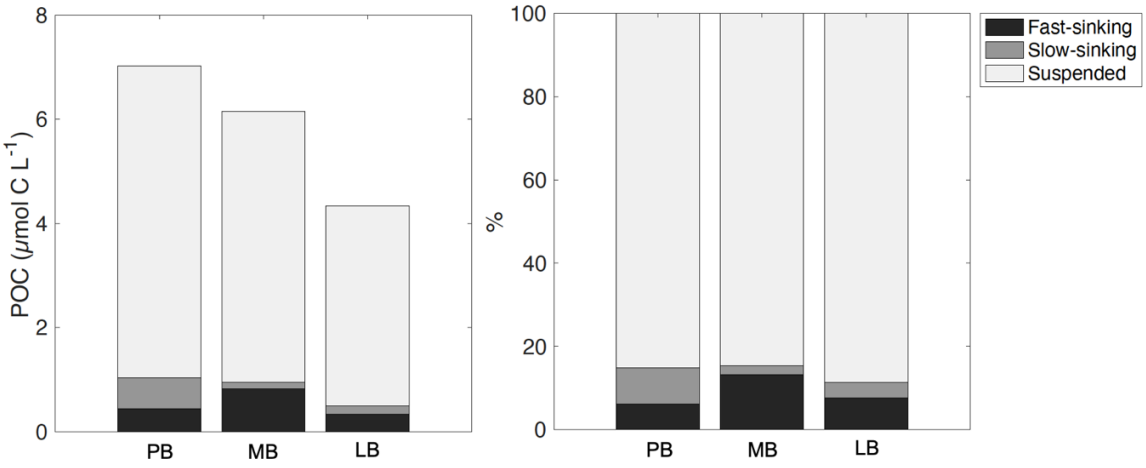

Figure 3. Concentrations of POC (µmol C L^{-1}) measured at the beginning of the experiments (Day 0) in the suspended fraction (light grey), the slow-sinking particle fraction (dark grey) and the fast-sinking particle fraction (black) (left) and the relative contributions (%) of each fraction to the total concentration of POC (right).

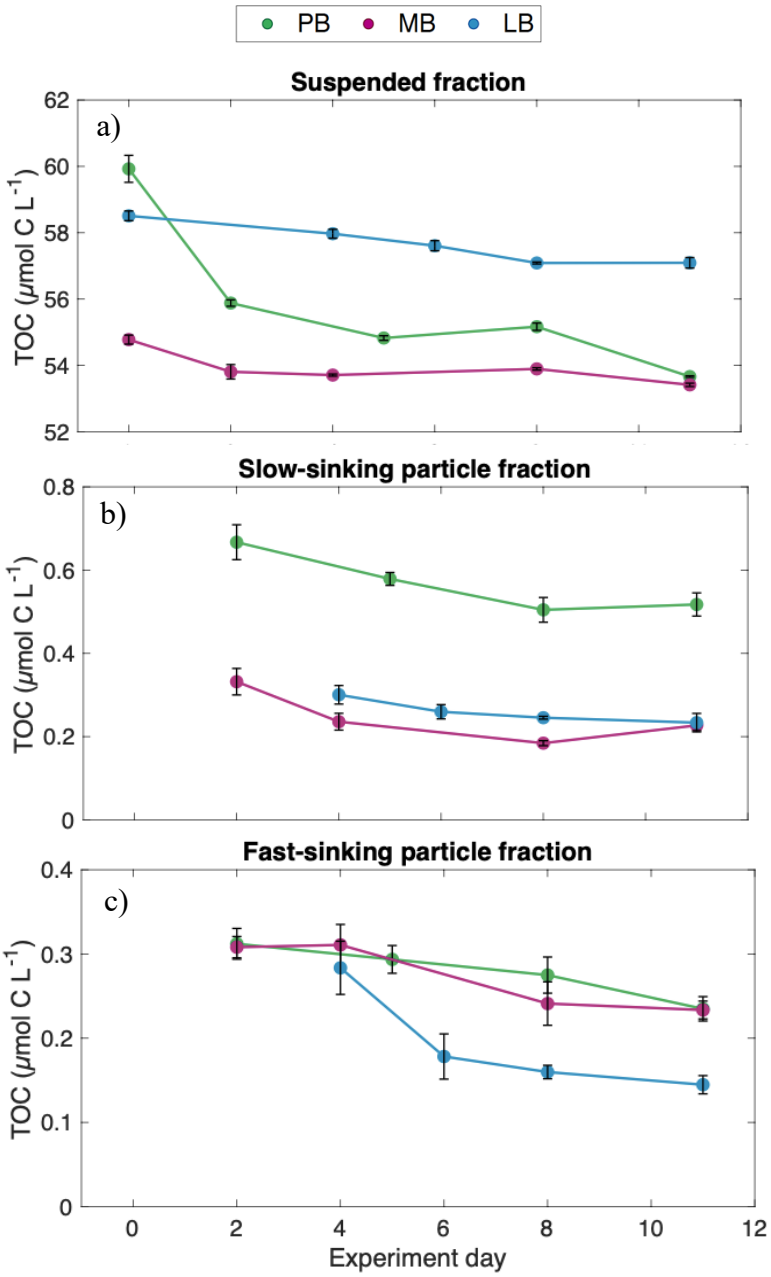

Figure 4. Time series of TOC concentrations measured during the TOC degradation experiments performed with fractions collected at station PB (green, *Phaeocystis* bloom station), station MB (pink, moderate biomass station) and station LM (blue, low biomass station). Data represent the change in TOC concentrations on the suspended fraction (a) and on the slow-sinking (b), and fast-sinking (c) particle fractions. Error bars indicate the standard deviation of the means of replicates (n = 3) propagated through the MSC calculations (section 2.3).

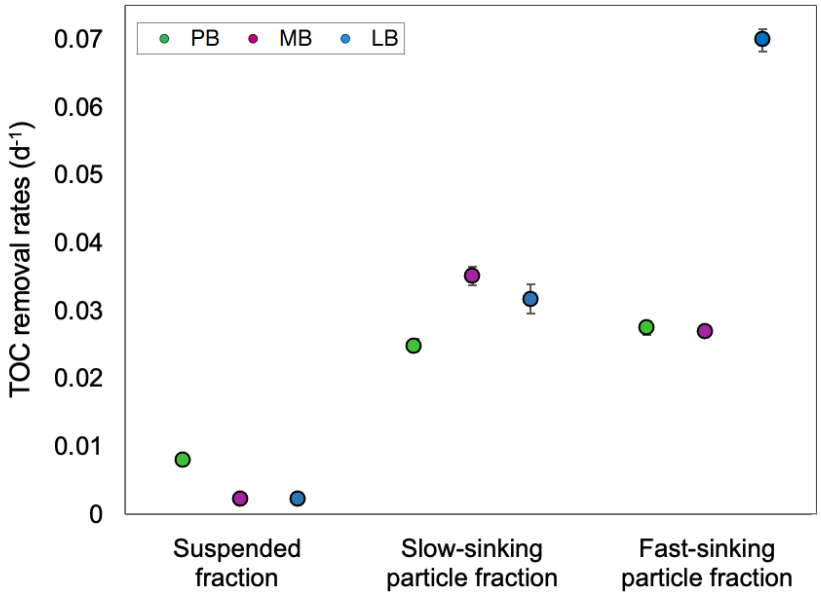

Figure 5. TOC degradation rates (d^{-1}) associated with the suspended fraction and, the slow-sinking and fast-sinking particle fraction for the three stations (PB, MB and LB). SD is the standard deviation of the means of the replicates (n = 3) propagated through the applied calculations (section 2.2 and 2.3).

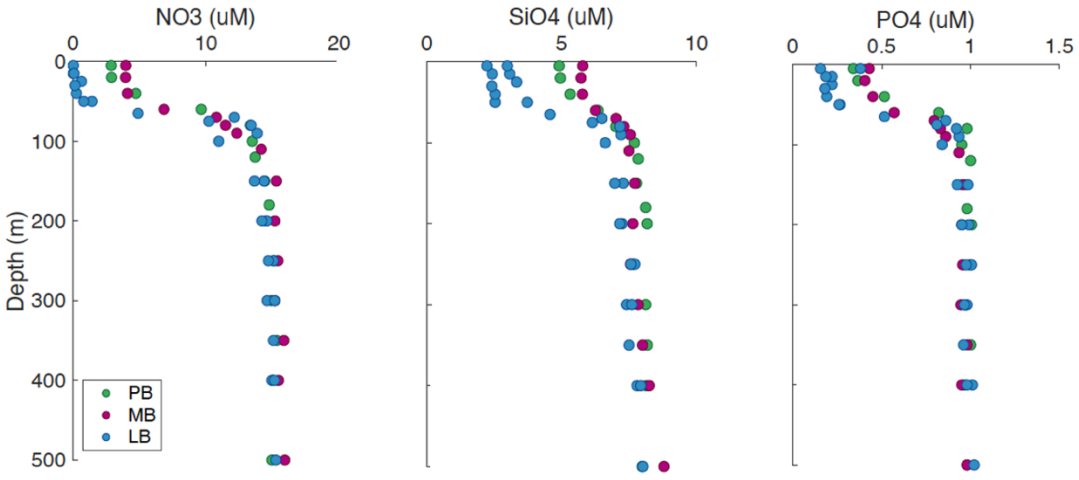

Figure 6. Depth profiles of the concentration of nitrate (NO_3), silicic acid (SiO_4) and phosphate (PO_4) measured on water collected with Niskin bottles at station PB (green, *Phaeocystis* bloom station), station MB (pink, moderate biomass station) and station LM (blue, low biomass station) on the same days of our MSC deployments.

References

Alcolombri, U., Peaudecerf, F.J., Fernandez, V.I., Behrendt, L., Lee, K.S. and Stocker, R., 2021. Sinking enhances the degradation of organic particles by marine bacteria. *Nature Geoscience*, *14*(10), pp.775-780.

Alldredge, A., 1998. The carbon, nitrogen and mass content of marine snow as a function of aggregate size. *Deep Sea Research Part I: Oceanographic Research Papers*, *45*(4-5), pp.529-541.

Alldredge, A.L. and Cohen, Y., 1987. Can microscale chemical patches persist in the sea? Microelectrode study of marine snow, fecal pellets. *Science*, *235*(4789), pp.689-691.

Alldredge, A.L. and Gotschalk, C.C., 1989. Direct observations of the mass flocculation of diatom blooms: characteristics, settling velocities and formation of diatom aggregates. *Deep Sea Research Part A. Oceanographic Research Papers*, *36*(2), pp.159-171.

Alldredge, A.L. and Silver, M.W., 1988. Characteristics, dynamics and significance of marine snow. *Progress in oceanography*, *20*(1), pp.41-82.

Alldredge, A.L., 2000. Interstitial dissolved organic carbon (DOC) concentrations within sinking marine aggregates and their potential contribution to carbon flux. *Limnology and Oceanography*, *45*(6), pp.1245-1253.

Alldredge, A.L., Granata, T.C., Gotschalk, C.C. and Dickey, T.D., 1990. The physical strength of marine snow and its implications for particle disaggregation in the ocean. *Limnology and Oceanography*, *35*(7), pp.1415-1428.

Alldredge, AL, Passow, U, Logan, BE. 1993. The abundance and significance of a class of large, transparent organic particles in the ocean. Deep Sea Research Part I: Oceanographic Research Papers 40(6): 1131–1140. DOI: https://doi.org/10.1016/0967-0637(93)90129-Q.

Álvarez, E, López-Urrutia, Á, Nogueira, E, Fraga, S. 2011. How to effectively sample the plankton size spectrum? A case study using FlowCAM. *Journal of Plankton Research* 33(7): 1119–1133. DOI: https://doi.org/10.1093/plankt/fbr012.

Amano, C., Zhao, Z., Sintes, E., Reinthaler, T., Stefanschitz, J., Kisadur, M., Utsumi, M. and Herndl, G.J., 2022. Limited carbon cycling due to high-pressure effects on the deep-sea microbiome. *Nature Geoscience*, *15*(12), pp.1041-1047.

Armstrong, RA, Lee, C, Hedges, JI, Honjo, S, Wakeham, SG. 2001. A new, mechanistic model for organic carbon fluxes in the ocean based on the quantitative association of POC with ballast minerals. *Deep Sea Research Part II: Topical Studies in Oceanography* 49(1–3): 219–236. DOI: https://doi.org/10.1016/S0967-0645(01)00101-1.

Azetsu-Scott, K, Passow, U. 2004. Ascending marine particles: Significance of transparent exopolymer particles (TEP) in the upper ocean. *Limnology and Oceanography* 49(3): 741–748. DOI: https://doi.org/10.4319/lo.2004.49.3.0741.

Baetge, N., Behrenfeld, M.J., Fox, J., Halsey, K.H., Mojica, K.D., Novoa, A., Stephens, B.M. and Carlson, C.A., 2021. The seasonal flux and fate of dissolved organic carbon through bacterioplankton in the Western North Atlantic. *Frontiers in Microbiology*, *12*, p.669883.

Baker, CA, Henson, SA, Cavan, EL, Giering, SL, Yool, A, Gehlen, M, Belcher, A, Riley, JS, Smith, HE, Sanders, R. 2017. Slow-sinking particulate organic carbon in the Atlantic Ocean: Magnitude, flux, and potential controls. *Global Biogeochemical Cycles* 31(7): 1051–1065. DOI: https://doi.org/10.1002/2017GB005638.

Baumas, C.M., Le Moigne, F.A., Garel, M., Bhairy, N., Guasco, S., Riou, V., Armougom, F., Grossart, H.P. and Tamburini, C., 2021. Mesopelagic microbial carbon production correlates with diversity across different marine particle fractions. *The ISME Journal*, *15*(6), pp.1695-1708.

Belcher, A, Iversen, M, Giering, S, Riou, V, Henson, SA, Berline, L, Guilloux, L, Sanders, R. 2016. Depth-resolved particle-associated microbial respiration in the northeast Atlantic. *Biogeosciences* 13(17): 4927–4943. DOI: https://doi.org/10.5194/bg-13-4927-2016.

Belcher, A., Saunders, R.A. and Tarling, G.A., 2019. Respiration rates and active carbon flux of mesopelagic fishes (Family Myctophidae) in the Scotia Sea, Southern Ocean. *Marine Ecology Progress Series*, *610*, pp.149-162.

Benner, R. and Amon, R.M., 2015. The size-reactivity continuum of major bioelements in the ocean. *Annual review of marine science*, *7*, pp.185-205.

Bisson, K, Siegel, DA, DeVries, T. 2020. Diagnosing mechanisms of ocean carbon export in a satellite-based food web model. *Frontiers in Marine Science* 7: 505. DOI: https://doi.org/10.3389/fmars.2020.00505.

Bittar, TB, Passow, U, Hamaraty, L, Bidle, KD, Harvey, EL. 2018. An updated method for the calibration of transparent exopolymer particle measurements. *Limnology and Oceanography: Methods* 16(10): 621–628. DOI: https://doi.org/10.1002/lom3.10268.

Blanco, JM, Echevarría, F, García, CM. 1994. Dealing with size-spectra: some conceptual and mathematical problems. *Scientia Marina* 58(1-2):17–29.

Bodel, Annie, "The Solitary Sinking Phytoplankton Cell and the Biological Carbon Pump" (2023). *Capstone Projects and Master's Theses*. 1504.

Boyd, P.W. and Trull, T.W., 2007. Understanding the export of biogenic particles in oceanic waters: Is there consensus?. *Progress in Oceanography*, *72*(4), pp.276-312.

Boyd, PW, Claustre, H, Levy, M, Siegel, DA, Weber, T. 2019. Multi-faceted particle pumps drive carbon sequestration in the ocean. *Nature* 568(7752): 327–335. DOI: https://doi.org/10.1038/s41586-019-1098-2.

Boyd, PW, Muggli, DL, Varela, DE, Goldblatt, RH, Chretien, R, Orians, KJ, Harrison, PJ. 1996. In vitro iron enrichment experiments in the NE subarctic Pacific. *Marine Ecology Progress Series* 136: 179–193. DOI: 10.3354/meps136179.

Boyd, PW, Trull, TW. 2007. Understanding the export of biogenic particles in oceanic waters: Is there consensus? *Progress in Oceanography* 72(4): 276–312. DOI: https://doi.org/10.1016/j.pocean.2006.10.007.

Briggs, N, Dall'Olmo, G, Claustre, H. 2020. Major role of particle fragmentation in regulating biological sequestration of CO_2 by the oceans. *Science* 367(6479): 791–793. DOI: https://doi.org/10.1126/science.aay179.

Brzezinski, MA, Varela, DE, Jenkins, BD, Buck, KN, Kafrissen, SM, Jones, JL. 2022. The upper ocean silicon cycle of the subarctic Pacific during the EXPORTS field campaign. *Elementa: Science of the Anthropocene* 10(1): 00087. DOI: https://doi.org/10.1525/elementa.2021.00087.

Buesseler, K.O., Antia, A.N., Chen, M., Fowler, S.W., Gardner, W.D., Gustafsson, O., Harada, K., Michaels, A.F., Rutgers van der Loeff, M., Sarin, M. and Steinberg, D.K., 2007. An assessment of the use of sediment traps for estimating upper ocean particle fluxes. *Journal of Marine Research*, *65*(3), pp.345-416.

Buesseler, K.O., Boyd, P.W., Black, E.E. and Siegel, D.A., 2020. Metrics that matter for assessing the ocean biological carbon pump. *Proceedings of the National Academy of Sciences*, *117*(18), pp.9679-9687.

Buesseler, K.O., Boyd, P.W., Black, E.E. and Siegel, D.A., 2020. Metrics that matter for assessing the ocean biological carbon pump. *Proceedings of the National Academy of Sciences*, *117*(18), pp.9679-9687.

Buesseler, KO, Antia, AN, Chen, M, Fowler, SW, Gardner, WD, Gustafsson, O, Harada, K, Michaels, AF, Rutgers van der Loeff, M, Sarin, M, Steinberg, D.K. 2007. An assessment of the use of sediment traps for estimating upper ocean particle fluxes. *Journal of Marine Research* 65(3): 345–416. DOI: http://dx.doi.org/10.1357/002224007781567621.

Buesseler, KO, Benitez-Nelson, CR, Roca-Martí, M, Wyatt, AM, Resplandy, L, Clevenger, SJ, Drysdale, JA, Estapa, ML, Pike, S, Umhau, BP. 2020. High-resolution spatial and temporal measurements of particulate organic carbon flux using thorium-234 in the northeast Pacific Ocean during the EXport Processes in the Ocean from RemoTe Sensing

field campaign. *Elementa: Science of the Anthropocene* 8(1). DOI: https://doi.org/10.1525/elementa.2020.030.

Burd, AB, Hansell, DA, Steinberg, DK, Anderson, TR, Arístegui, J, Baltar, F, Beaupre, SR,Buesseler, KO, DeHairs, F, Jackson, GA, Kadko, D.C. 2010. Assessing the apparent imbalance between geochemical and biochemical indicators of meso-and bathypelagic biological activity: What the@ $♯! is wrong with present calculations of carbon budgets? *Deep Sea Research Part II: Topical Studies in Oceanography* 57(16):1557–1571. DOI: https://doi.org/10.1016/j.dsr2.2010.02.022.

Cael, B.B., Cavan, E.L. and Britten, G.L., 2021. Reconciling the size-dependence of marine particle sinking speed. *Geophysical Research Letters*, *48*(5), p.e2020GL091771.

Carlson, C.A. and Hansell, D.A., 2015. DOM sources, sinks, reactivity, and budgets. *Biogeochemistry of marine dissolved organic matter*, pp.65-126.

Cassie, RM. 1962. Frequency distribution models in the ecology of plankton and other organisms. *The Journal of Animal Ecology* 31(1): 65–92.

Cavan, EL, Henson, SA, Belcher, A, Sanders, R. 2017. Role of zooplankton in determining the efficiency of the biological carbon pump. *Biogeosciences* 14(1): 177–186. DOI: https://doi.org/10.5194/bg-14-177-2017.

Charette, MA, Moran, SB, Bishop, JK. 1999. 234Th as a tracer of particulate organic carbon export in the subarctic northeast Pacific Ocean. *Deep Sea Research Part II* 46(11–12): 2833–2861. DOI: https://doi.org/10.1016/S0967-0645(99)00085-5-.

Cho, B.C. and Azam, F., 1988. Major role of bacteria in biogeochemical fluxes in the ocean's interior. *Nature*, *332*(6163), pp.441-443.

Collins, J.R., Edwards, B.R., Thamatrakoln, K., Ossolinski, J.E., DiTullio, G.R., Bidle, K.D., Doney, S.C. and Van Mooy, B.A., 2015. The multiple fates of sinking particles in the North Atlantic Ocean. *Global Biogeochemical Cycles*, *29*(9), pp.1471-1494.

Collins, JR, Edwards, BR, Thamatrakoln, K, Ossolinski, JE, DiTullio, GR, Bidle, KD, Doney, SC, Van Mooy, BA. 2015. The multiple fates of sinking particles in the North Atlantic Ocean. *Global Biogeochemical Cycles* 29(9): 1471 –1494. DOI: https://doi.org/10.1002/2014GB005037.

Crombet, Y, Leblanc, K, Queguiner, B, Moutin, T, Rimmelin, P, Ras, J, Claustre, H, Leblond, N, Oriol, L, Pujo-Pay, M. 2011. Deep silicon maxima in the stratified oligotrophic Mediterranean Sea. *Biogeosciences* 8(2): 459 –475. DOI: https://doi.org/10.5194/bg-8-459-2011.

D'Asaro, E.A., Thomson, J., Shcherbina, A.Y., Harcourt, R.R., Cronin, M.F., Hemer, M.A. and Fox-Kemper, B., 2014. Quantifying upper ocean turbulence driven by surface waves. *Geophysical Research Letters*, *41*(1), pp.102-107.

Dagg, MJ, Urban-Rich, J, Peterson, JO. 2003. The potential contribution of fecal pellets from large copepods to the flux of biogenic silica and particulate organic carbon in the Antarctic Polar Front region near 170 W. *Deep Sea Research Part II: Topical Studies in Oceanography* 50(3–4): 675 –691. DOI: https://doi.org/10.1016/S0967-0645(02)00590-8.

Dall'Olmo, G, Mork, KA, 2014. Carbon export by small particles in the Norwegian Sea. *Geophysical Research Letters* 41: 2921–2927. DOI: https://doi.org/10.1002/2014GL059244.

Dall'Olmo, G. and Mork, K.A., 2017. Carbon export by small particles in the Norwegian Sea.
In *Climate Change and the Oceanic Carbon Cycle* (pp. 131-146). Apple Academic Press.

de Boyer Montégut, C., Madec, G., Fischer, A.S., Lazar, A. and Iudicone, D., 2004. Mixed layer depth over the global ocean: An examination of profile data and a profile-based climatology. *Journal of Geophysical Research: Oceans*, *109*(C12).

Delmont, T.O., Hammar, K.M., Ducklow, H.W., Yager, P.L. and Post, A.F., 2014. Phaeocystis antarctica blooms strongly influence bacterial community structures in the Amundsen Sea polynya. *Frontiers in microbiology*, *5*, p.646.

DeLong, E.F., Franks, D.G. and Alldredge, A.L., 1993. Phylogenetic diversity of aggregate-attached vs. free-living marine bacterial assemblages. *Limnology and oceanography*, *38*(5), pp.924-934.

Dever, M, Nicholson, D, Omand, MM, Mahadevan, A. 2021. Size-differentiated export flux in different dynamical regimes in the ocean. *Global Biogeochemical Cycles* 35(3): p.e2020GB006764. DOI: https://doi.org/10.1029/2020GB006764.

DeVries, T, Primeau, F, Deutsch, C. 2012. The sequestration efficiency of the biological pump. *Geophysical Research Letters* 39(13): L13601. DOI: https://doi.org/10.1029/2012GL051963.

Duret, M.T., Lampitt, R.S. and Lam, P., 2019. Prokaryotic niche partitioning between suspended and sinking marine particles. *Environmental microbiology reports*, *11*(3), pp.386-400.

Durkin, CA, Buesseler, KO, Cetinić, I, Estapa, ML, Kelly, RP, Omand, M. 2021. A visual tour of carbon export by sinking particles. *Global Biogeochemical Cycles* 35(10): p.e2021GB006985. DOI: https://doi.org/10.1029%2F2021GB006985.

Durkin, CA, Estapa, ML, Buesseler, KO. 2015. Observations of carbon export by small sinking particles in the upper mesopelagic. *Marine Chemistry* 175: 72–81. DOI: https://doi.org/10.1016/j.marchem.2015.02.011.

Dyer, K.R. and Manning, A.J., 1999. Observation of the size, settling velocity and effective density of flocs, and their fractal dimensions. *Journal of sea research*, *41*(1-2), pp.87-95.

Ebersbach, F, Trull, TW. 2008. Sinking particle properties from polyacrylamide gels during the KErguelen Ocean and Plateau compared Study (KEOPS): Zooplankton control of carbon export in an area of persistent natural iron inputs in the Southern Ocean. *Limnology and Oceanography* 53(1): 212–224. DOI: https://doi.org/10.4319/lo.2008.53.1.0212.

Ebersbach, F. and Trull, T.W., 2008. Sinking particle properties from polyacrylamide gels during the KErguelen Ocean and Plateau compared Study (KEOPS): Zooplankton control of carbon export in an area of persistent natural iron inputs in the Southern Ocean. *Limnology and Oceanography*, *53*(1), pp.212-224.

Engel, A, Endres, S, Galgani, L, Schartau, M. 2020. Marvelous marine microgels: on the distribution and impact of gel-like particles in the oceanic water-column. *Frontiers in Marine Science* 7: 405. DOI: https://doi.org/10.3389/fmars.2020.00405.

Engel, A, Passow, U. 2001. Carbon and nitrogen content of transparent exopolymer particles (TEP) in relation to their Alcian Blue adsorption. *Marine Ecology Progress Series* 219: 1–10. DOI: http://dx.doi.org/10.3354/meps219001.

Engel, A, Schartau, M. 1999. Influence of transparent exopolymer particles (TEP) on sinking velocity of Nitzschia closterium aggregates. *Marine Ecology Progress Series* 182: 69–76. DOI: https://www.jstor.org/stable/24852120.

Engel, A. and Passow, U., 2001. Carbon and nitrogen content of transparent exopolymer particles (TEP) in relation to their Alcian Blue adsorption. *Marine Ecology Progress Series*, *219*, pp.1-10.

Estapa ML, Durkin CA, Slade WH, Huffard CL, O'Neill SP, Omand MM. 2023. A new, global optical sediment trap calibration. EarthArXiv. doi: 10.31223/X5NQ1X.

Estapa, M, Buesseler, K, Durkin, CA, Omand, M, Benitez-Nelson, CR, Roca-Martí, M, Breves, E, Kelly, RP, Pike, S. 2021. Biogenic sinking particle fluxes and sediment trap collection efficiency at Ocean Station Papa. *Elementa: Science of the Anthropocene* 9(1): 00122. DOI: https://doi.org/10.1525/elementa.2020.00122.

Friedlingstein, P, Jones, MW, O'sullivan, M, Andrew, RM, Hauck, J, Peters, GP, Peters, W, Pongratz, J, Sitch, S, Le Quéré, C, Bakker, DC. 2019. Global carbon budget 2019. *Earth System Science Data* 11(4): 1783–1838. DOI: https://doi.org/10.5194/essd-11-1783-2019.

Friedlingstein, P., O'sullivan, M., Jones, M.W., Andrew, R.M., Hauck, J., Olsen, A., Peters, G.P., Peters, W., Pongratz, J., Sitch, S. and Le Quéré, C., 2020. Global carbon budget 2020. *Earth System Science Data Discussions*, *2020*, pp.1-3.

García-Martín, E.E., Davidson, K., Davis, C.E., Mahaffey, C., Mcneill, S., Purdie, D.A. and Robinson, C., 2021. Low contribution of the fast-sinking particle fraction to total plankton metabolism in a temperate shelf sea. *Global Biogeochemical Cycles*, *35*(9), p.e2021GB007015.

Gardner, WD. 1977. Incomplete extraction of rapidly settling particles from water samplers 1. *Limnology and Oceanography* 22(4): 764–768. DOI: https://doi.org/10.4319/lo.1977.22.4.0764.

Giering, S.L. and Evans, C., 2022. Overestimation of prokaryotic production by leucine incorporation—and how to avoid it. *Limnology and Oceanography*, *67*(3), pp.726-738.

Giering, S.L., Sanders, R., Lampitt, R.S., Anderson, T.R., Tamburini, C., Boutrif, M., Zubkov, M.V., Marsay, C.M., Henson, S.A., Saw, K. and Cook, K., 2014. Reconciliation of the carbon budget in the ocean's twilight zone. *Nature*, *507*(7493), pp.480-483.

Giering, S.L.C., Sanders, R., Blackbird, S., Briggs, N., Carvalho, F., East, H., Espinola, B., Henson, S.A., Kiriakoulakis, K., Iversen, M.H. and Lampitt, R.S., 2023. Vertical imbalance in organic carbon budgets is indicative of a missing vertical transfer during a phytoplankton bloom near South Georgia (COMICS). *Deep Sea Research Part II: Topical Studies in Oceanography*, *209*, p.105277.

Giering, S.L.C., Sanders, R., Martin, A.P., Lindemann, C., Möller, K.O., Daniels, C.J., Mayor, D.J. and St. John, M.A., 2016. High export via small particles before the onset of the N orth A tlantic spring bloom. *Journal of Geophysical Research: Oceans*, *121*(9), pp.6929-6945.

Giering, SL, Hosking, B, Briggs, N, Iversen, MH. 2020. The interpretation of partic
Giering, SL, Sanders, R, Lampitt, RS, Anderson, TR, Tamburini, C, Boutrif, M, Zubkov, MV, Marsay, CM, Henson, SA, Saw, K, Cook, K. 2014. Reconciliation of the carbon budget in the ocean's twilight zone. *Nature* 507(7493): 480–483. DOI: https://doi.org/10.1038/nature13123.

Giering, SL, Sanders, R, Martin, AP, Henson, SA, Riley, JS, Marsay, CM, Johns, DG. 2017. Particle flux in the oceans: Challenging the steady state assumption. *Global Biogeochemical Cycles* 31(1): 159–171. DOI: https://doi.org/10.1002/2016GB005424.

Giering, SLC, Sanders, R, Martin, AP, Lindemann, C, Möller, KO, Daniels, CJ, Mayor, DJ, St. John, MA. 2016. High export via small particles before the onset of the North Atlantic spring bloom. *Journal of Geophysical Research: Oceans* 121(9): 6929–6945. DOI: https://doi.org/10.1002/2016JC012048.

Graff, JR, Nelson, NB, Roca-Martí, M, Romanelli, E, Kramer, SJ, Erickson, Z, Cetinić, I, Buesseler, KO, Passow, U, Zhang, X, Siegel DA. n.d. Reconciliation of total particulate organic carbon and nitrogen measurements determined using contrasting methods in the North Pacific Ocean. *Elementa: Science of the Anthropocene* (*submitted*).

Grossart, H.P. and Simon, M., 2007. Interactions of planktonic algae and bacteria: effects on algal growth and organic matter dynamics. *Aquatic Microbial Ecology*, *47*(2), pp.163-176.
Hamanaka, J, Tanoue, E, Hama, T, Handa, N. 2002. Production and export of particulate fatty acids, carbohydrates and combined amino acids in the euphotic zone. *Marine Chemistry* 77(1): 55–69. DOI: https://doi.org/10.1016/S0304-4203(01)00075-5.

Harvey, HR, Tuttle, JH, Bell, JT. 1995. Kinetics of phytoplankton decay during simulated sedimentation: changes in biochemical composition and microbial activity under oxic and anoxic conditions. *Geochimica et Cosmochimica Acta* 59(16): 3367–3377. DOI: https://doi.org/10.1016/0016-7037(95)00217-N.

Halewood, E., Opalk, K., Custals, L., Carey, M., Hansell, D.A. and Carlson, C.A., 2022. Determination of dissolved organic carbon and total dissolved nitrogen in seawater using High Temperature Combustion Analysis. *Frontiers in Marine Science*, *9*, p.1061646.

Henson, S., Le Moigne, F. and Giering, S., 2019. Drivers of carbon export efficiency in the global ocean. *Global biogeochemical cycles*, *33*(7), pp.891-903.

Henson, SA, Sanders, R, Madsen, E, Morris, PJ, Le Moigne, F, Quartly, GD. 2011. A reduced estimate of the strength of the ocean's biological carbon pump. *Geophysical Research Letters* 38(4). DOI: https://doi.org/10.1029/2011GL046735.

Honjo, S., Manganini, S.J. and Cole, J.J., 1982. Sedimentation of biogenic matter in the deep ocean. *Deep Sea Research Part A. Oceanographic Research Papers*, *29*(5), pp.609-625.

Ionescu, D., Bizic-Ionescu, M., Khalili, A., Malekmohammadi, R., Morad, M.R., de Beer, D. and Grossart, H.P., 2015. A new tool for long-term studies of POM-bacteria interactions: overcoming the century-old Bottle Effect. *Scientific reports*, *5*(1), p.14706.

Iversen, M.H. and Lampitt, R.S., 2020. Size does not matter after all: no evidence for a size-sinking relationship for marine snow. *Progress in Oceanography*, *189*, p.102445.

Iversen, MH, Lampitt, RS. 2020. Size does not matter after all: no evidence for a size-sinking relationship for marine snow. *Progress in Oceanography* 189: 102445. DOI: https://doi.org/10.1016/j.pocean.2020.102445.

Iversen, MH, Ploug, H. 2013. Temperature effects on carbon-specific respiration rate and sinking velocity of diatom aggregates–potential implications for deep ocean export processes. *Biogeosciences* 10(6): 4073–4085. DOI: https://doi.org/10.5194/bg-10-4073-2013.

Iversen, MH. 2022. Carbon export in the ocean: A biologist's perspective. *Annual Review of Marine Science* 15: 357–381. DOI: https://doi.org/10.1146/annurev-marine-032122-035153.

Jackson, A.S., Blair, S.N., Mahar, M.T., Wier, L.T., Ross, R.M. and Stuteville, J.E., 1990. Prediction of functional aerobic capacity without exercise testing. *Medicine and science in sports and exercise*, *22*(6), pp.863-870.

Jackson, GA. 1995. Comparing observed changes in particle size spectra with those predicted using coagulation theory. *Deep Sea Research Part II: Topical Studies in Oceanography* 42(1): 159–184. DOI: https://doi.org/10.1016/0967-0645(95)00010-N.

Johnson L, Siegel D, Thompson A, Fields E, Erickson Z, Cetinic. I, Lee C, D'Asaro E, Nelson N, Omand M, Sten M, Traylor S, Nicholson D, Graff J, Steinberg D, Sosik H, Buesseler K, Brzezinski M, Soto Ramos I, Carvalho F, Henson S (2023). Assessment of Oceanographic Conditions during the North Atlantic Export Processes in the Ocean from RemoTe Sensing (EXPORTS).

Kawakami, H, Honda, MC, Matsumoto, K, Fujiki, T, Watanabe, S. 2010. East-west distribution of POC fluxes estimated from ^{234}Th in the northern North Pacific in autumn. *Journal of Oceanography* 66(1): 71–83. DOI: https://doi.org/10.1007/s10872-010-0006-z.

Khatiwala, S., Tanhua, T., Mikaloff Fletcher, S., Gerber, M., Doney, S.C., Graven, H.D., Gruber, N., McKinley, G.A., Murata, A., Ríos, A.F. and Sabine, C.L., 2013. Global ocean storage of anthropogenic carbon. *Biogeosciences*, *10*(4), pp.2169-2191.

Kiørboe, T. and Jackson, G.A., 2001. Marine snow, organic solute plumes, and optimal chemosensory behavior of bacteria. *Limnology and Oceanography*, *46*(6), pp.1309-1318.

Kiørboe, T., Hansen, J.L., Alldredge, A.L., Jackson, G.A., Passow, U., Dam, H.G., Drapeau, D.T., Waite, A. and Garcia, C.M., 1996. Sedimentation of phytoplankton during a diatom bloom: rates and mechanisms. *Journal of Marine Research*, *54*(6), pp.1123-1148.

Klaas, C. and Archer, D.E., 2002. Association of sinking organic matter with various types of mineral ballast in the deep sea: Implications for the rain ratio. *Global biogeochemical cycles*, *16*(4), pp.63-1.

Kaiser, K. and Benner, R., 2009. Biochemical composition and size distribution of organic matter at the Pacific and Atlantic time-series stations. *Marine Chemistry*, *113*(1-2), pp.63-77.

Kriest, I. 2002. Different parameterizations of marine snow in a 1D-model and their influence on representation of marine snow, nitrogen budget and sedimentation. *Deep Sea Research Part I: Oceanographic Research Papers* 49(12): 2133–2162. DOI: http://dx.doi.org/10.1016/S0967-0637(02)00127-9.

Kwon, E.Y., Primeau, F. and Sarmiento, J.L., 2009. The impact of remineralization depth on the air–sea carbon balance. *Nature Geoscience*, *2*(9), pp.630-635.

Kwon, EY, Primeau, F, Sarmiento, JL. 2009. The impact of remineralization depth on the air–sea carbon balance. *Nature Geoscience* 2(9): 630–635. DOI: http://dx.doi.org/10.1038/ngeo612.

Lampitt, R.S., Wishner, K.F., Turley, C.M. and Angel, M.V., 1993. Marine snow studies in the Northeast Atlantic Ocean: distribution, composition and role as a food source for migrating plankton. *Marine Biology*, *116*, pp.689-702.

Lampitt, RS, Wishner, KF, Turley, CM, Angel, MV. 1993. Marine snow studies in the Northeast Atlantic Ocean: distribution, composition and role as a food source for migrating plankton. *Marine Biology* 116(4): 689–702. DOI: https://doi.org/10.1007/BF00355486.

Laurenceau-Cornec, EC, Le Moigne, FA, Gallinari, M, Moriceau, B, Toullec, J, Iversen, MH, Engel, A, De La Rocha, CL. 2020. New guidelines for the application of Stokes' models to the sinking velocity of marine aggregates. *Limnology and Oceanography* 65(6): 1264–1285. DOI: https://doi.org/10.1002/lno.11388.

le size, shape, and carbon flux of marine particle images is strongly affected by the choice of particle detection algorithm. *Frontiers in Marine Science* 7: 564. DOI: https://doi.org/10.3389/fmars.2020.00564.

Logan, B.E., Passow, U., Alldredge, A.L., Grossartt, H.P. and Simont, M., 1995. Rapid formation and sedimentation of large aggregates is predictable from coagulation rates (half-lives) of transparent exopolymer particles (TEP). *Deep Sea Research Part II: Topical Studies in Oceanography*, *42*(1), pp.203-214.

Lombardo, C.P. and Gregg, M.C., 1989. Similarity scaling of viscous and thermal dissipation in a convecting surface boundary layer. *Journal of Geophysical Research: Oceans*, *94*(C5), pp.6273-6284.

Mackinson, B, Moran, S, Lomas, M, Stewart, GM, Kelly, R. 2015. Estimates of micro-, nano-, and picoplankton contributions to particle export in the northeast Pacific. *Biogeosciences* 12(11): 3429–3446. DOI: https://doi.org/10.5194/bg-12-3429-2015.

Mari, X, Passow, U, Migon, C, Burd, AB, Legendre, L. 2017. Transparent exopolymer particles: Effects on carbon cycling in the ocean. *Progress in Oceanography* 151: 13–37. DOI: https://doi.org/10.1016/j.pocean.2016.11.002.

Mari, X., Rassoulzadegan, F., Brussaard, C.P. and Wassmann, P., 2005. Dynamics of transparent exopolymeric particles (TEP) production by Phaeocystis globosa under N-or P-limitation: a controlling factor of the retention/export balance. *Harmful algae*, *4*(5), pp.895-914.

Marsay, C.M., Sanders, R.J., Henson, S.A., Pabortsava, K., Achterberg, E.P. and Lampitt, R.S., 2015. Attenuation of sinking particulate organic carbon flux through the mesopelagic ocean. *Proceedings of the National Academy of Sciences*, *112*(4), pp.1089-1094.

Marsay, CM, Sanders, RJ, Henson, SA, Pabortsava, K, Achterberg, EP, Lampitt, RS. 2015. Attenuation of sinking particulate organic carbon flux through the mesopelagic ocean. *Proceedings of the National Academy of Sciences* 112(4): 1089–1094. DOI: https://doi.org/10.1073/pnas.1415311112.

Martin, JH, Fitzwater, SE. 1988. Iron deficiency limits phytoplankton growth in the north-east Pacific subarctic. *Nature* 331(6154): 341–343. DOI: https://doi.org/10.1038/331341A0.

McDonnell, A.M.P., Boyd, P.W. and Buesseler, K.O., 2015. Effects of sinking velocities and microbial respiration rates on the attenuation of particulate carbon fluxes through the mesopelagic zone. *Global Biogeochemical Cycles*, *29*(2), pp.175-193.

McDonnell, AM, Buesseler, KO. 2010. Variability in the average sinking velocity of marine particles. *Limnology and Oceanography* 55(5): 2085–2096. DOI: https://doi.org/10.4319/lo.2010.55.5.2085.

McKinley, G.A., Fay, A.R., Lovenduski, N.S. and Pilcher, D.J., 2017. Natural variability and anthropogenic trends in the ocean carbon sink. *Annual review of marine science*, *9*, pp.125-150.

McNair, HM, Meyer, MG, Lerch, SJ, Maas, AE, Stephens, BM, Fox, J, Buck, KN, Burns, SM, Cetinic, I, Cohn, MR, Durkin, C. 2023. Quantitative analysis of food web dynamics in a low export ecosystem. *bioRxiv*: 2023–03. DOI: https://doi.org/10.1101/2023.03.17.532807.

McNair, HM, Morison, F, Graff, JR, Rynearson, TA, Menden-Deuer, S. 2021. Microzooplankton grazing constrains pathways of carbon export in the subarctic North Pacific. *Limnology and Oceanography* 66(7): 2697–2711. DOI: https://doi.org/10.1002/lno.11783.

Meyer MG, Gong W, Kafrissen SM, Torano O, Varela DE, Santoro AE, Cassar N, Gifford S, Niebergall AK, Sharpe G, Marchetti A. 2022. Phytoplankton size-class contributions to new and regenerated production during the EXPORTS Northeast Pacific Ocean field deployment. *Elementa: Science of the Anthropocene* 10(1): 00068. DOI: https://doi.org/10.1525/elementa.2021.00068.

Meyer, M.G., Brzezinski, M., Cohn, M.R., Kramer, S.J., Paul, N., Sharpe, G.C., Niebergall, A.K., Gifford, S.M., Cassar, N. and Marchetti, A., 2023. Primary production dynamics during the decline phase of the North Atlantic annual spring bloom.

Mitchell, C, Hu, C, Bowler, B, Drapeau, D, Balch, WM. 2017. Estimating particulate inorganic carbon concentrations of the global ocean from ocean color measurements using a

reflectance difference approach. *Journal of Geophysical Research: Oceans* 122(11): 8707–8720. DOI: https://doi.org/10.1002/2017JC013146.

Moore, JK, Villareal, TA. 1996. Size-ascent rate relationships in positively buoyant marine diatoms. *Limnology and Oceanography* 41(7): 1514–1520. DOI: https://doi.org/10.4319/lo.1996.41.7.1514.

Moran, SB, Charette, MA, Pike, SM, Wicklund, CA. 1999. Differences in seawater particulate organic carbon concentration in samples collected using small-and large-volume methods: the importance of DOC adsorption to the filter blank. *Marine Chemistry* 67(1–2): 33–42. DOI: https://doi.org/10.1016/S0304-4203(99)00047-X.

Mouw, C.B., Barnett, A., McKinley, G.A., Gloege, L
. and Pilcher, D., 2016. Global ocean particulate organic carbon flux merged with satellite parameters. *Earth System Science Data*, *8*(2), pp.531-541.

Nagata, T, Yamada, Y, Fukuda, H. 2021. Transparent exopolymer particles in deep oceans: synthesis and future challenges. *Gels* 7(3): 75. DOI: https://doi.org/10.3390/gels7030075.

Nayar, S, Chou, LM. 2003. Relative efficiencies of different filters in retaining phytoplankton for pigment and productivity studies. *Estuarine, Coastal and Shelf Science* 58(2): 241–248. DOI: https://doi.org/10.1016/S0272-7714(03)00075-1.

Nowicki, M, DeVries, T, Siegel, DA. 2022. Quantifying the carbon export and sequestration pathways of the ocean's biological carbon pump. *Global Biogeochemical Cycles* 36(3): p.e2021GB007083. DOI: https://doi.org/10.1029/2021GB007083.

Nowicki, M., DeVries, T. and Siegel, D.A., 2022. Quantifying the carbon export and sequestration pathways of the ocean's biological carbon pump. *Global Biogeochemical Cycles*, *36*(3), p.e2021GB007083.

Obernosterer, I, Herndl, GJ. 1995. Phytoplankton extracellular release and bacterial growth: dependence on the inorganic N: P ratio. *Marine Ecology Progress Series. Oldendorf* 116(1): 247–257. DOI: http://dx.doi.org/10.3354/meps116247.

Omand, M.M., Govindarajan, R., He, J. and Mahadevan, A., 2020. Sinking flux of particulate organic matter in the oceans: Sensitivity to particle characteristics. *Scientific reports*, *10*(1), p.5582.

Omand, MM, D'Asaro, EA, Lee, CM, Perry, MJ, Briggs, N, Cetinić, I, Mahadevan, A. 2015. Eddy-driven subduction exports particulate organic carbon from the spring bloom. *Science*, 348(6231): 222–225. DOI: https://doi.org/10.1126/science.1260062.

Ortega-Retuerta, E, Mazuecos, IP, Reche, I, Gasol, JM, Álvarez-Salgado, XA, Álvarez, M, Montero, MF, Arístegui, J. 2019. Transparent exopolymer particle (TEP) distribution and in situ prokaryotic generation across the deep Mediterranean Sea and nearby North East

Atlantic Ocean. *Progress in Oceanography* 173: 180–191. DOI: https://doi.org/10.1016/j.pocean.2019.03.002.

Ortega-Retuerta, E, Reche, I, Pulido-Villena, E, Agustí, S, Duarte, CM. 2009. Uncoupled distributions of transparent exopolymer particles (TEP) and dissolved carbohydrates in the Southern Ocean. *Marine Chemistry* 115(1–2): 59–65. DOI: https://doi.org/10.1016/j.marchem.2009.06.004.

Owen, BM, Hallett, CS, Cosgrove, JJ, Tweedley, JR, Moheimani, NR. 2022. Reporting of methods for automated devices: A systematic review and recommendation for studies using FlowCam for phytoplankton. *Limnology and Oceanography: Methods* 20(7): 400–427. DOI: https://doi.org/10.1002/lom3.10496.

Parekh, P, Dutkiewicz, S, Follows, MJ, Ito, T. 2006. Atmospheric carbon dioxide in a less dusty world. *Geophysical Research Letters* 33(3). DOI: https://doi.org/10.1029/2005GL025098.

Parekh, P., Dutkiewicz, S., Follows, M.J. and Ito, T., 2006. Atmospheric carbon dioxide in a less dusty world. *Geophysical research letters*, *33*(3).

Passow, U, Alldredge, AL. 1994. Distribution, size and bacterial colonization of transparent exopolymer particles (TEP) in the ocean. *Marine Ecology Progress Series* 113: 185–198. DOI: http://dx.doi.org/10.3354/meps113185.

Passow, U, Alldredge, AL. 1995. A dye-binding assay for the spectrophotometric measurement of transparent exopolymer particles (TEP). *Limnology and Oceanography* 40(7): 1326–1335. DOI: https://doi.org/10.4319/lo.1995.40.7.1326.

Passow, U, Alldredge, AL. 1999. Do transparent exopolymer particles (TEP) inhibit grazing by the euphausiid Euphausia pacifica?. *Journal of Plankton Research* 21(11): 2203–2217. DOI: https://doi.org/10.1093/plankt/21.11.2203.

Passow, U, De La Rocha, CL. 2006. Accumulation of mineral ballast on organic aggregates. *Global Biogeochemical Cycles* 20(1): GB1013. DOI: https://doi.org/10.1029/2005GB002579-.

Passow, U. 2002. Transparent exopolymer particles (TEP) in aquatic environments. *Progress in Oceanography* 55(3–4): 287–333. DOI: https://doi.org/10.1016/S0079-6611(02)00138-6.

Passow, U. 2004. Switching perspectives: Do mineral fluxes determine particulate organic carbon fluxes or vice versa?. *Geochemistry, Geophysics, Geosystems* 5(4): Q04002. DOI: https://doi.org/10.1029/2003GC000670.

Passow, U. and Alldredge, A.L., 1994. Distribution, size and bacterial colonization of transparent exopolymer particles (TEP) in the ocean. *Marine Ecology Progress Series*, pp.185-198.

Passow, U. and Alldredge, A.L., 1995. A dye-binding assay for the spectrophotometric measurement of transparent exopolymer particles (TEP). *Limnology and Oceanography*, *40*(7), pp.1326-1335.

Passow, U. and Peinert, R., 1993. The role of plankton in particle flux: Two case studies from the northeast Atlantic. *Deep Sea Research Part II: Topical Studies in Oceanography*, *40*(1-2), pp.573-585.

Passow, U., 2002. Transparent exopolymer particles (TEP) in aquatic environments. *Progress in oceanography*, *55*(3-4), pp.287-333.

Picheral, M, Guidi, L, Stemmann, L, Karl, DM, Iddaoud, G, Gorsky, G. 2010. The Underwater Vision Profiler 5: An advanced instrument for high spatial resolution studies of particle size spectra and zooplankton. *Limnology and Oceanography: Methods* 8(9): 462–473. DOI: https://doi.org/10.4319/lom.2010.8.462.

Picheral, M., Guidi, L., Stemmann, L., Karl, D.M., Iddaoud, G. and Gorsky, G., 2010. The Underwater Vision Profiler 5: An advanced instrument for high spatial resolution studies of particle size spectra and zooplankton. *Limnology and Oceanography: Methods*, *8*(9), pp.462-473.

Ploug, H., Grossart, H.P., Azam, F. and Jørgensen, B.B., 1999. Photosynthesis, respiration, and carbon turnover in sinking marine snow from surface waters of Southern California Bight: implications for the carbon cycle in the ocean. *Marine Ecology Progress Series*, *179*, pp.1-11.

Richardson, TL. 2019. Mechanisms and pathways of small-phytoplankton export from the surface ocean. *Annual Review of Marine Science* 11(1): 57–74. DOI: https://doi.org/10.1146/annurev-marine-121916-063627.

Riebesell, U., 1991. Particle aggregation during a diatom bloom II. Biological aspects. *Marine Ecology Progress Series*, *69*, pp.281-291.

Riley, J.S., Sanders, R., Marsay, C., Le Moigne, F.A., Achterberg, E.P. and Poulton, A.J., 2012. The relative contribution of fast and slow sinking particles to ocean carbon export. *Global Biogeochemical Cycles*, *26*(1).

Riley, JS, Sanders, R, Marsay, C, Le Moigne, FA, Achterberg, EP, Poulton, AJ. 2012. The relative contribution of fast and slow sinking particles to ocean carbon export. *Global Biogeochemical Cycles* 26(1). DOI: https://doi.org/10.1029/2011GB004085.

Robinson, KL, Sponaugle, S, Luo, JY, Gleiber, MR, Cowen, RK. 2021. Big or small, patchy all: Resolution of marine plankton patch structure at micro-to submesoscales for 36 taxa. *Science Advances* 7(47): p.eabk2904. DOI: https://doi.org/10.1126/sciadv.abk2904.

Roca-Martí, M, Benitez-Nelson, CR, Umhau, BP, Wyatt, AM, Clevenger, SJ, Pike, S, Horner, TJ, Estapa, ML, Resplandy, L, Buesseler, KO. 2021. Concentrations, ratios, and sinking fluxes of major bioelements at Ocean Station Papa. *Elementa: Science of the Anthropocene* 9(1): 00166. DOI: https://doi.org/10.1525/elementa.2020.00166.

Romanelli, E., Giering, S.L., Sweet, J., Siegel, D.A., Passow. U. The importance of transparent exopolymer particles over ballast in determining both sinking and suspension of small particles during late summer in the Northeast Pacific Ocean. In press, Elementa: Science of the Anthropocene.

Ruiz, J.E. and Izquierdo, A., 1997. A simple model for the break-up of marine aggregates by turbulent shear. *Oceanolica Acta*, *20*(4), pp.597-605.

Sherr, E.B. and Sherr, B.F., 2007. Heterotrophic dinoflagellates: a significant component of microzooplankton biomass and major grazers of diatoms in the sea. *Marine Ecology Progress Series*, *352*, pp.187-197.

Siegel, D.A., DeVries, T., Cetinić, I. and Bisson, K.M., 2023. Quantifying the Ocean's Biological Pump and Its Carbon Cycle Impacts on Global Scales. *Annual review of marine science*, *15*, pp.329-356.

Siegel, DA, Buesseler, KO, Doney, SC, Sailley, SF, Behrenfeld, MJ, Boyd, PW. 2014. Global assessment of ocean carbon export by combining satellite observations and food-web models. *Global Biogeochemical Cycles* 28(3): 181–196. DOI: https://doi.org/10.1002/2013GB004743.

Siegel, DA, Cetinić, I, Graff, JR, Lee, CM, Nelson, N, Perry, MJ, Ramos, IS, Steinberg, DK, Buesseler, K, Hamme, R, Fassbender, AJ. 2021. An operational overview of the EXport Processes in the Ocean from RemoTe Sensing (EXPORTS) Northeast Pacific field deployment. *Elementa: Science of the Anthropocene* 9(1): 00107. DOI: https://doi.org/10.1525/elementa.2020.00107.

Siegel, DA, DeVries, T, Cetinić, I, Bisson, KM. 2023. Quantifying the ocean's biological pump and its carbon cycle impacts on global scales. *Annual Review of Marine Science* 15: 329–356. DOI: https://doi.org/10.1146/annurev-marine-040722-115226.

Siegel, DA, Fields, E, Buesseler, KO. 2008. A bottom-up view of the biological pump: Modeling source funnels above ocean sediment traps. *Deep Sea Research Part I: Oceanographic Research Papers* 55(1): 108–127. DOI: https://doi.org/10.1016/j.dsr.2007.10.006.

Siegel, DA. 1998. Resource competition in a discrete environment: Why are plankton distributions paradoxical?. *Limnology and Oceanography* 43(6): 1133–1146. DOI: https://doi.org/10.4319/lo.1998.43.6.1133.

Sieracki, CK, Sieracki, ME, Yentsch, CS. 1998. An imaging-in-flow system for automated analysis of marine microplankton. *Marine Ecology Progress Series* 168: 285–296. DOI: http://dx.doi.org/10.3354/meps168285.

Sieracki, M.E., Verity, P.G. and Stoecker, D.K., 1993. Plankton community response to sequential silicate and nitrate depletion during the 1989 North Atlantic spring bloom. *Deep Sea Research Part II: Topical Studies in Oceanography*, *40*(1-2), pp.213-225.

Smetacek, V.S., 1985. Role of sinking in diatom life-history cycles: ecological, evolutionary and geological significance. *Marine biology*, *84*, pp.239-251.

Smith, D.C., Simon, M., Alldredge, A.L. and Azam, F., 1992. Intense hydrolytic enzyme activity on marine aggregates and implications for rapid particle dissolution. *Nature*, *359*(6391), pp.139-142.

Steinberg, D.K., Cope, J.S., Wilson, S.E. and Kobari, T., 2008. A comparison of mesopelagic mesozooplankton community structure in the subtropical and subarctic North Pacific Ocean. *Deep Sea Research Part II: Topical Studies in Oceanography*, *55*(14-15), pp.1615-1635.

Steinberg, D.K., Stamieszkin, K., Maas, A.E., Durkin, C.A., Passow, U., Estapa, M.L., Omand, M.M., McDonnell, A.M., Karp-Boss, L., Galbraith, M. and Siegel, D.A., 2023. The outsized role of salps in carbon export in the subarctic Northeast Pacific Ocean. *Global Biogeochemical Cycles*, *37*(1), p.e2022GB007523.

Steinberg, DK, Landry, MR. 2017. Zooplankton and the ocean carbon cycle. *Annual Review of Marine Science* 9: 413–444. DOI: https://doi.org/10.1146/annurev-marine-010814-015924.

Steinberg, DK, Stamieszkin, K, Maas, AE, Durkin, CA, Passow, U, Estapa, ML, Omand, MM, McDonnell, AM, Karp-Boss, L, Galbraith, M, Siegel, DA. 2023. The outsized role of salps in carbon export in the subarctic Northeast Pacific Ocean. *Global Biogeochemical Cycles* 37(1): p.e2022GB007523. DOI: https://doi.org/10.1029/2022GB007523.

Stemmann, L, Jackson, GA, Ianson, D. 2004. A vertical model of particle size distributions and fluxes in the midwater column that includes biological and physical processes—Part I: model formulation. *Deep Sea Research Part I: Oceanographic Research Papers* 51(7): 865–884. DOI: http://dx.doi.org/10.1016/j.dsr.2004.03.001.

Stemmann, L., Jackson, G.A. and Ianson, D., 2004. A vertical model of particle size distributions and fluxes in the midwater column that includes biological and physical

processes—Part I: model formulation. *Deep Sea Research Part I: Oceanographic Research Papers*, *51*(7), pp.865-884.

Strickland, JDH, Parsons, TR. 1968. A practical handbook of seawater analysis fisheries. Research Board of Canada Ottawa. *Bulletin* 167: 185–206.

Tabata S, Boston NE, Boyce FM. 1965. The relation between wind speed and summer isothermal surface layer of water at ocean station P in the eastern subarctic Pacific Ocean. *Journal of Geophysical Research* 70(16): 3867–3878. DOI: https://doi.org/10.1029/JZ070i016p03867.

Takeuchi, M., Doubell, M.J., Jackson, G.A., Yukawa, M., Sagara, Y. and Yamazaki, H., 2019. Turbulence mediates marine aggregate formation and destruction in the upper ocean. *Scientific Reports*, *9*(1), p.16280.

Timothy, D, Wong, C, Barwell-Clarke, J, Page, J, White, L, Macdonald, RW. 2013. Climatology of sediment flux and composition in the subarctic Northeast Pacific Ocean with biogeochemical implications. *Progress in Oceanography* 116: 95–129. DOI: http://dx.doi.org/10.1016/j.pocean.2013.06.017.

Tiselius, P. and Kuylenstierna, M., 1996. Growth and decline of a diatom spring bloom phytoplankton species composition, formation of marine snow and the role of heterotrophic dinoflagellates. *Journal of Plankton Research*, *18*(2), pp.133-155.

Tréguer, D.M Nelson, M.A Brzezinski, D.J De Master, J Van Bennekom, A Kamatani Protocol for determination of biogenic and of lithogenic silica in particulate matter SO-JGOFS core parameter, Int. Rep. (1992), p. 4.

Villareal, TA. 1988. Positive buoyancy in the oceanic diatom *Rhizosolenia debyana* H. Peragallo. *Deep Sea Research Part A. Oceanographic Research Papers* 35(6): 1037–1045. DOI: https://doi.org/10.1016/0198-0149(88)90075-1.

Volk, T, Hoffert, MI. 1985. Ocean carbon pumps: Analysis of relative strengths and efficiencies in ocean-driven atmospheric CO2 changes. *The carbon cycle and atmospheric CO_2: natural variations Archean to present* 32: 99–110. DOI: https://doi.org/10.1029/GM032p0099.

Volk, T. and Hoffert, M.I., 1985. Ocean carbon pumps: Analysis of relative strengths and efficiencies in ocean-driven atmospheric CO2 changes. *The carbon cycle and atmospheric CO2: Natural variations Archean to present*, *32*, pp.99-110.

Wong, C, Waser, N, Whitney, F, Johnson, W, Page, J. 2002. Time-series study of the biogeochemistry of the North East subarctic Pacific: reconciliation of the C_{org}/N remineralization and uptake ratios with the Redfield ratios. *Deep Sea Research Part II* 49(24–25): 5717–5738. DOI: https://doi.org/10.1016/S0967-0645(02)00211-4.

Woods, S, Villareal, TA. 2008. Intracellular ion concentrations and cell sap density in positively buoyant oceanic phytoplankton. *Nova Hedwigia Beiheft* 133: 131–145.

Yamada, Y, Yokokawa, T, Uchimiya, M, Nishino, S, Fukuda, H, Ogawa, H, Nagata, T. 2017. Transparent exopolymer particles (TEP) in the deep ocean: full-depth distribution patterns and contribution to the organic carbon pool. *Marine Ecology Progress Series* 583: 81–93. DOI: http://dx.doi.org/10.3354/meps12339.